# Performance improvement in LiFi using advanced modulation techniques and learning-based coexistence with WiFi


By

**Rizwana Ahmad**

under the guidance of

**Dr. Anand Srivastava**

Professor, IIIT-Delhi

**Indraprastha Institute of Information Technology, Delhi**


**May, 2021**

# Performance improvement in LiFi using advanced modulation techniques and learning-based coexistence with WiFi


By

**Rizwana Ahmad**

PhD-16113

under the guidance of

**Dr. Anand Srivastava**

Professor, IIIT-Delhi


**submitted**

**in partial fulfillment of the requirements for the degree of Doctor of Philosophy**

**to**

**Indraprastha Institute of Information Technology, Delhi**

**May, 2021**

To my loving family ...

# Certificate

This is to certify that the thesis titled "***Performance improvement in LiFi using advanced modulation techniques and learning-based coexistence with WiFi***" being submitted by ***Rizwana Ahmad*** to the Indraprastha Institute of Information Technology-Delhi, for the award of the degree of **Doctor of Philosophy**, is an original research work carried out by her under my supervision. In my opinion, the thesis has reached the standard fulfilling the requirements of the regulations relating to the degree.

The results contained in this thesis have not been submitted in part or full to any other university or institute for the award of any degree or diploma.

October 2021
Prof. Anand Srivastava

Indraprastha Institute of Information Technology-Delhi
New Delhi-110020

# Acknowledgements

Being a student of science, I have always wondered what would have happened if "Electronics and Communication" as a faculty of science didn't exist. Well, one thing for sure is that we wouldn't have been able to create computers, and mobiles to name only two out of many, which have practically changed our views of the world as well as our "lives" itself. Throughout these years I have learned that there are those who build the blocks of technology and those who use them; my passion is in creating such block of technology used in cutting edge research. This thesis represents not only my work at the keyboard, but also a milestone with more than one decade of work in the field that I have always loved.

To begin with, I would like to say thanks to *Almighty Allah* for all the blessings he has bistowed upon me.

I would like to express my gratitude to **Prof. Anand Srivastava** without whom the completion of this work would not have been possible. I would also like to thank him for his valuable guidance, scholarly inputs and the consistent encouragement, I have received throughout the research work. The joy and enthusiasm he has for research was contagious and motivational for me, even during tough times in the Ph.D. pursuit.

My special words of thanks to **Dr. Majid Safari** (University of Edinburgh) and **Dr. Vivek Bohara** (IIIT-D) for their valuable inputs that helped me to find the correct answers to some of the most daunting challenges that I faced in my work. I would also like to thank Dr. Abhishek Dixit (IIT-D) and Dr. Mohammad S. Hashmi (IIIT-D) for serving as my committee members and taking out their valuable time for their insightful feedback and useful suggestions on my work. I would also like to thank **Intel India** for believing in my technical acumen and funding my research.

My words of thanks to my friend Dilnashin, and research collaborator Mohammad (University of Edinburgh) for their help, and support. I also take the opportunity to thank the administration staff at IIIT-Delhi, especially Ms. Priti Patel, for being kind enough to address all my queries throughout these years. I am very grateful to them for all their help and support.

Moreover, I would like to give a special thanks to my husband (Syed Faraz Umar), my uncle (Mr. R. H. Fazli) and other family members for their unconditional love, motivation, and constant support. I dedicate this thesis to them as a token of gratitude.

# Abstract

*Keywords-* **LiFi, WiFi, O-OFDM, PAPR, DP-OFDM, GMSK, DFT, O-GFDM, HLWN, load balancing, RL, RWP, ORWP.**

A significant increase in wireless communication has been observed over the past decade. The existing radio frequency (RF) based communication network is not able to cope up with this influx in connections and data requirements. In order to meet future needs, researchers have started investigating Light Fidelity (LiFi) for the indoor environment. LiFi offers various advantages over RF, such as a vast spectrum, spatial reuse, and inherent security. Furthermore, LiFi does not interfere with the devices operating in the RF spectrum. However, LiFi technology has its limitations; the major challenges of the LiFi system include the non-linearity due to LiFi front end, limited front-end bandwidth, and susceptibility to blockages. In this dissertation, we have tried to address these aforementioned challenges.

Firstly, we propose an adaptive learning architecture (ALA)-based predistoter to mitigate the effect of front-end non-linearity. The proposed ALA predistoter achieved near-linear performance in terms of amplitude-amplitude (AM/AM) distortions and constellation plots for different LiFi front-ends non-linearity.

Secondly, in order to support high data rates with limited front-end bandwidth, highly spectral efficient modulation schemes such as optical orthogonal frequency division multiplexing (O-OFDM) are required. Nonetheless, the major drawback of O-OFDM is that it suffers from a high peak-to-average power ratio (PAPR), which causes clipping distortion, reduces the illumination-to-communication conversion efficiency, and affects the lifetime of the LED. Therefore, in this thesis, we propose advanced spectrally efficient low PAPR modulation schemes such as double precoded optical orthogonal frequency division multiplexing (DP-OOFDM) and optical-generalized frequency division multiplexing (O-GFDM). The simulation results validate that the proposed DP-OOFDM with interleaved subcarrier mapping provides PAPR as low as 2.1 dB compared to 12.7 dB for the corresponding O-OFDM counterpart. Lastly, in order to deal with the problem of blockages in LiFi, the coexistence of LiFi and WiFi

has been proposed in the literature. However, an appropriate load balancing strategy plays a vital role in the overall performance of such heterogeneous LiFi WiFi networks (HLWN). Nonetheless, the problem of load balancing of HLWN is a non-convex mixed-integer nonlinear programming (MINLP) optimization problem, i.e., it is mathematically intractable. Therefore, in this thesis, we propose a reinforcement learning (RL) based load balancing technique for HLWN. Additionally, we also explore the effect of different mobility models and link aggregation in HLWN. Simulation results illustrate that the proposed RL-based method can ensure near-optimal performance at relatively low complexity.

The proposed frameworks in this dissertation can be utilized in LiFi standards. It will be helpful for LiFi communication engineers to design an efficient physical layer and intelligent load balancing scheme for HLWN without performing extensive simulations.

# Table of contents

# List of figures

# List of tables

# Nomenclature

## Acronyms

| | |
|---|---|
| ACO-OFDM | Asymmetrically Clipped Optical-Orthogonal Frequency-Division Multiplexing |
| ALA | Adaptive-Learning-Architecture |
| AM/AM | Amplitude-Amplitude Modulation |
| AP | Access Point |
| AWGN | Additive White Gaussian Noise |
| BER | Bit-Error-Rate |
| CAP | Carrier-less Amplitude and Phase |
| CC | Central Controller |
| CCDF | Complementary Cumulative Distribution Function |
| CCI | Co-Channel Interference |
| CP | Cyclic Prefix |
| CSK | Color Shift Keying |
| CSMA/CA | Carrier-Sense Multiple Access with Collision Avoidance |
| DCO-OFDM | Direct-Current biased Optical OFDM |
| DFT | Discrete Fourier Transform |
| DHT | Discrete Hartley Transform |
| DK | Domain Knowledge |
| DP-OOFDM | Double Precoded Optical-Orthogonal Frequency-Division Multiplexing |
| EVM | Error Vector Magnitude |
| Exh-LA-DK | Exhaustive search based load balancing in Link aggregation enabled Heterogeneous LiFi WiFi Network with Domain Knowledge |
| Exh-LA | Exhaustive search based load balancing in Link Aggregation enabled heterogeneous LiFi WiFi Network |

| | |
|---|---|
| Exh-SAP-DK | Exhaustive search based load balancing in Single Access Point connection heterogeneous LiFi WiFi Network with Domain Knowledge |
| Exh-SAP | Exhaustive Search based load balancing in Single Access Point connection heterogeneous LiFi WiFi Network |
| FIR | Finite Impulse Response |
| FoV | Field of View |
| G-DP-OOFDM | Grouped DP-OOFDM |
| G-I-DP-OOFDM | Grouped Double Precoded Optical-Orthogonal Frequency-Division Multiplexing with Interleaved subcarrier mapping |
| G-L-DP-OOFDM | Grouped Double Precoded Optical-Orthogonal Frequency-Division Multiplexing with Localized subcarrier mapping |
| GFDM | Generalized Frequency Division Multiplexing |
| GMSK | Gaussian-minimum-shift-keying |
| HHO | Horizontal Handover |
| HLWN | Heterogeneous LiFi WiFi Network |
| HRWP | Hotspot Random Waypoint |
| HRWP | Hotspot Random Waypoint |
| HS | Hermitian Symmetry |
| I-DFT OOFDM | Discrete Fourier Transform precoded Optical-Orthogonal Frequency-Division Multiplexing with Interleaved subcarrier mapping |
| I-DP-OOFDM | Double Precoded Optical-Orthogonal Frequency-Division Multiplexing with interleaved subcarrier mapping |
| IDFT | Inverse Discrete Fourier Transform |
| IFFT | Inverse Fast Fourier Transform |
| IM/DD | Intensity Modulation with Direct Detection |
| L-DFT OOFDM | Discrete Fourier Transform precoded Optical-Orthogonal Frequency-Division Multiplexing with Localized subcarrier mapping |
| L-DP-OOFDM | Double Precoded Optical-Orthogonal Frequency-Division Multiplexing with Localized subcarrier mapping |
| LA | Link Aggregation |
| LB | Load Balancing |
| LED | Light Emitting Diodes |
| LiFi | Light Fidelity |
| LoS | Line-of-Sight |

| | |
|---|---|
| m-CAP | Mutliband Carrier-less Amplitude and Phase |
| MA | Medium Access |
| MDPs | Markov Decision Processes |
| MINLP | Mixed-Integer Nonlinear Programming |
| MLP | Multi-Layer Perceptron |
| MTC | Machine Type Communication |
| NLoS | Non-Line-of-Sight |
| O-OFDM | Optical Orthogonal Frequency-Division Multiplexing |
| OFDMA | Orthogonal Frequency-Division Multiple Access |
| OFDM | Orthogonal Frequency Division Multiplexing |
| OGFDM-DC | Optical Generalized Frequency Division Multiplexing with DC bias |
| OGFDM-NDC | Optical Generalized Frequency Division Multiplexing without DC bias |
| O-GFDM | Optical Generalized Frequency Division Multiplexing |
| OOK | On-Off Keying |
| ORWP | Orientation-based Random Waypoint |
| OWC | optical wireless communication |
| PAM | Pulse-Amplitude Modulation |
| PAPR | Peak-to-Average Power Ratio |
| PD | Photo-Detector |
| PPM | Pulse Position Modulation |
| QAM | Quadrature Amplitude Modulation |
| QoS | Quality of Services |
| RF | Radio Frequency |
| RL-LA-DK | Reinforcement Learning based load balancing in Link aggregation enabled Heterogeneous LiFi WiFi network with domain knowledge |
| RL-LA | Reinforcement Learning based load balancing in Link aggregation enabled Heterogeneous LiFi WiFi Network |
| RL | Reinforcement Learning |
| RSS-LA-DK | Received Signal Strategy based load balancing in Link aggregation enabled Heterogeneous LiFi WiFi Network with Domain Knowledge |
| RSS-LA | Received Signal Strategy based load balancing in Link aggregation enabled Heterogeneous LiFi WiFi Network |

| | |
|---|---|
| RSS-SAP-DK | Received Signal Strategy based load balancing in Single Access Point connection heterogeneous LiFi WiFi Network with Domain Knowledge |
| RSS-SAP | Received Signal Strategy based load balancing in Single Access Point connection heterogeneous LiFi WiFi Network |
| RSS | Received Signal Strategy |
| RWP | Random Waypoint |
| SAP | Single AP Receiver |
| SER | Symbol-Error-Rate |
| SINR | Signal-to-Interference-Noise Ratio |
| SNR | Signal-to-Noise Ratio |
| SSS | Signal Strength Strategy |
| TDMA | Time-Division Multiple Access |
| TIA | Trans-impedance amplifier |
| TRPO | Trust Region Policy Optimization |
| VHO | Vertical Handover |
| VLC | Visible Light Communication |

# Symbols

| | |
|---|---|
| $\alpha$ | AP |
| $\alpha_1^{t-1}$ | WiFi AP connection at t-1 |
| $\alpha_1^t$ | WiFi AP connection at t |
| $\alpha_2^{t-1}$ | LiFi AP connection at t-1 |
| $\alpha_2^t$ | LiFi AP connection at t |
| $\Delta T$ | Delay between the LOS and onset of the diffused signals |
| $\eta_1$ | spectral efficiency ratio of ACO-OFDM over DCO-OFDM |
| $\eta_2$ | spectral efficiency ratio of OGFDM-DC over DCO-OFDM |
| $\eta_3$ | spectral efficiency ratio of OGFDM-NDC over DCO-OFDM |
| $\eta(\pi)$ | RL agents discounted cumulative reward under policy $\pi$ |
| $\eta_{0,\mathrm{HHO}}$ | Average HHO handover efficiency |
| $\eta_{0,\mathrm{VHO}}$ | Average VHO handover efficiency |
| $\eta_{\mathrm{LA}}(t)$ | Estimated handover efficiency for LA user |
| $\eta_{\mathrm{SAP}}(t)$ | Estimated handover efficiency for SAP user |
| $\eta_f$ | Jain's fairness index |
| $\gamma$ | Discount factor |
| $\Gamma_{ACO-OFDM}$ | PAPR of ACO-OFDM |
| $\Gamma_{DP-OOFDM}$ | PAPR of DP-OOFDM |
| $\hat{c}_p$ | Predistorter coefficient |
| $\mathbb{AP}$ | Set of APs |
| $\mathbb{A}$ | RL agent's set of actions |
| $\mathbb{LAP}$ | Set of LiFi APs |
| $\mathbb{R}$ | RL agent's set of rewards |
| $\mathbb{S}$ | Set of MDP states |
| $\mathbb{U}$ | Set of users |
| $\mathbb{W}$ | Set of WiFi APs |
| $\mu$ | User |
| $\Phi$ | Rate outage probability |
| $\phi$ | Angle of irradiation |

| | |
|---|---|
| $\Phi_{1/2}$ | LED half intensity angle |
| $\pi$ | RL agents policy |
| $\pi^*$ | RL agents optimum policy |
| $\psi$ | Angle of incidence at the PD |
| $\Psi_c$ | Field of View the PD |
| $\rho$ | Reflectivity of the walls |
| $\sigma^2_{shot}$ | Power of shot noise |
| $\sigma^2_{thermal}$ | Power of thermal noise |
| $\theta$ | Policy network with parameters |
| $\xi$ | PAPR value corresponding value to a particular clipping probability |
| $\xi_i$ | Hotspot intensity |
| $\zeta$ | PAPR threshold value |
| $\zeta_{NL}$ | LED nonlinearity coefficient |
| $A_{\text{room}}$ | Area of the room |
| $A_a$ | Hotspot area |
| $a_t$ | RL agent action |
| $A_\pi$ | Advantage function |
| $A_\pi$ | Value function |
| $A_{PD}$ | Area of the PD |
| $B$ | Noise bandwidth |
| $B_{\text{WiFi}}$ | WiFi AP bandwidth |
| $d$ | Distance between the transmitter (LED) and receiver (PD) |
| $d_{\text{BP}}$ | Breakpoint distance |
| $dr_{\mu,\alpha}$ | Achievable data rate of the user $\mu$ connected to AP $\alpha$ |
| $EVM$ | Error Vector Magnitude |
| $f$ | WiFi carrier frequency |
| $f_c$ | Cut-off frequency of the diffuse optical channel |
| $g(t)$ | Pulse shaping filter |
| $g(t)_{GMSK}$ | GMSK pulse shaping filter |
| $G_(\mu,\alpha)(f)$ | WiFi channel gain between user $\mu$ and AP $\alpha$ |

| | |
|---|---|
| $g_{\mathrm{c}}$ | Gain of the optical concentrator |
| $g_{\mathrm{f}}$ | Gain of the optical filter |
| $g_{\mu,\alpha}$ | Binary connection variable betwenn AP $\alpha$ and user $\mu$ |
| $H(f)_{\mathrm{LiFi}}$ | Frequency response of the optical channel |
| $H(f)_{\mathrm{LoS}}$ | Frequency response of the line-of-sight optical channel |
| $H(f)_{\mathrm{LoS}}$ | Frequency response of the non-line-of-sight optical channel |
| $h(t)$ | Impulse response of the optical channel |
| $h_{\mathrm{LoS}}(t)$ | Impulse response of the line-of-sight optical channel |
| $h_{\mathrm{NLoS}}(t)$ | Impulse response of the non-line-of-sight optical channel |
| $h_{\mathrm{r}}$ | WiFi small-scale fading gain |
| $H_{\mathrm{LiFi}(\mu,\alpha)}$ | LiFi channel gain between AP $\alpha$ and user $\mu$ |
| $I(x_k)$ | In-phase component of $k^{th}$ subcarrier of $x(n)$ |
| $I(y_k)$ | In-phase component of $k^{th}$ subcarrier of $y(n)$ |
| $I$ | Number of iteration iterative method takes to converge |
| $I_2$ | Noise bandwidth factor |
| $I_{\mathrm{BG}}$ | Background current |
| $I_{DC}$ | LED normalized bias current |
| $I_{in}(t)$ | LED input current |
| $J$ | Number of time slots |
| $k_B$ | Boltzmann's constant |
| $k_{\mu,\alpha}$ | Faction AP $\alpha$ resources allocated to user $\mu$ |
| $L(d)$ | WiFi large-scale fading loss |
| $L_{\mathrm{FS}}$ | WiFi free space loss |
| $M$ | Modulation order |
| $m$ | Lambertian order |
| $M_\alpha$ | Total number of users connected to AP $\alpha$ |
| $n(t)$ | Additive white Gaussian noise |
| $N$ | Number of subcarrier |
| $n$ | refractive index of the concentrator |
| $N_{\mathrm{AP\text{-}LiFi}}$ | Total number of LiFi APs |

| | |
|---|---|
| $N_{\text{AP-WiFi}}$ | Total number of WiFi APs |
| $N_{\text{LiFi}}$ | Noise spectral density for LiFi |
| $N_{\text{u}}$ | Total number of users |
| $N_{\text{WiFi}}$ | Noise spectral density for WiFi |
| $P_{\text{opt}}$ | Received optical power |
| $P_{ACO-OFDM}$ | Power required for the transmission of ACO-OFDM signal |
| $P_{avg}$ | Average power |
| $P_{DFT-precodedOOFDM}$ | Power required for the transmission of DFT-precoded OOFDM |
| $P_{DP-OOFDM}$ | Power required for the transmission of DP-OOFDM signal |
| $P_{saving_{DFT-precodedOOFDM}}$ | Power saving of DFT-precoded OOFDM over ACO-OFDM |
| $P_{saving_{DP-OOFDM}}$ | Power saving of DP-OOFDM over ACO-OFDM |
| $Q(x_k)$ | Quadrature phase component of $k^{th}$ subcarrier of $x(n)$ |
| $Q(y_k)$ | Quadrature phase component of $k^{th}$ subcarrier of $y(n)$ |
| $q$ | electron charge |
| $Q_\pi$ | State-action value function |
| $R(\phi)$ | Lambertion radiation intensity |
| $R_1$ | RL reward designed to maximize the long-term average datarate |
| $R_2$ | RL reward designed to maximize the long-term user satisfaction |
| $R_3$ | RL reward designed to ensure 50% user satisfaction and maximize the long-term user satisfaction |
| $R_{\text{PD}}$ | Responsivity of the PD |
| $R_L$ | Receiver equivalent load resistance |
| $r_t$ | RL agents immediate reward |
| $R_\mu$ | Data requirement of user $\mu$ |
| $R_{ACO}$ | Bit rate of ACO-OFDM |
| $R_{DCO}$ | Bit rate of DCO-OFDM |
| $R_{OGFDM-DC}$ | Bit rate of OGFDM-DC |
| $R_{OGFDM-NDC}$ | Bit rate of OGFDM-NDC |
| $s_t$ | MDP State |
| $s_0$ | MDP intial state |

| | |
|---|---|
| $S_{\mu,\alpha}$ | User satisfaction |
| $s_{t+1}$ | MDP next State |
| $SINR_{\mu,\alpha}$ | SINR for the user $\mu$ connected to LiFi AP $\alpha$ |
| $SINR_{\mu,\beta}$ | LiFi channel gain between user $\mu$ and interfering LiFi APs $\beta$ |
| $SNR_{\mu,\alpha}(f)$ | SNR of the user $\mu$ connected to WiFi AP $\alpha$ |
| $SNR_{\mu,\alpha}$ | SNR for the user $\mu$ connected to LiFi AP $\alpha$ |
| $T$ | OFDM Symbol duration |
| $T_{\text{avg}}$ | Average datarate |
| $T_k$ | Absolute temperature in Kelvin |
| $T_{CP}$ | CP duration |
| $U_\alpha$ | Set of users connected to AP $\alpha$ |
| $v(n)$ | Predistorter output signal |
| $x(n)$ | DCO-OFDM signal |
| $X_{\text{SF}}$ | WiFi shadowing loss |
| $X_k$ | DFT precoded signal |
| $X_k$ | PAPR of a transmitted signal $z_n$ |
| $y(n)$ | LED output signal |
| $Y_q$ | Signal after subcarrier mapping |
| $EVM_T$ | EVM threshold |

Chapter 1

# Introduction

In this chapter, the motivation of the work is discussed in Section 1.1. Followed by Section 1.2 which states the overall objectives of the thesis. The major contributions of this dissertation and relevant publications are summarized in Section 1.3. The outline of the thesis is discussed in Section 1.4. Finally, Section 1.5 concludes the introduction.

## 1.1 Motivation

Cisco report predicts that by 2023, two-thirds of the global population will have the Internet and the average data-rate requirement will increase by more than three times from 2018 [10]. This rapidly growing connections and data traffic have placed huge pressure on the radio frequency (RF) communication network, it has been forecasted that the entire RF spectrum will not be sufficient to provide the demanded traffic by 2035 [11]. In order to support future data traffic requirements, it is imperative to explore other parts of the electromagnetic spectrum (shown in Fig.1.1) for devising new communication technologies. Thus, many researchers are investigating visible light communication (VLC) as one of the promising solutions for the short-range indoor communication. As the name suggests, this technology works on the visible light spectrum i.e. 400-830 THz, thus can potentially utilize 400 THz unlicensed spectrum. VLC offers inherent security and higher spatial reuse because of the nature of visible light that does not pass through the walls. Furthermore, VLC does not interfere with devices operating at 2.4 GHz, thus it can be used in RF sensitive environments such as aeroplanes and hospitals. Additionally, VLC is a green technology, since it is power efficient and utilizes the existing illumination infrastructure for communication [1, 12]. The VLC technology exploits light emitting diodes (LEDs) as transmitters to provide high speed wireless communications. Unfortunately, the conventional blue-phosphor LEDs can only support the 3-dB bandwidth of approximately 3-5 MHz, due to the slow phosphor response. Researchers are actively

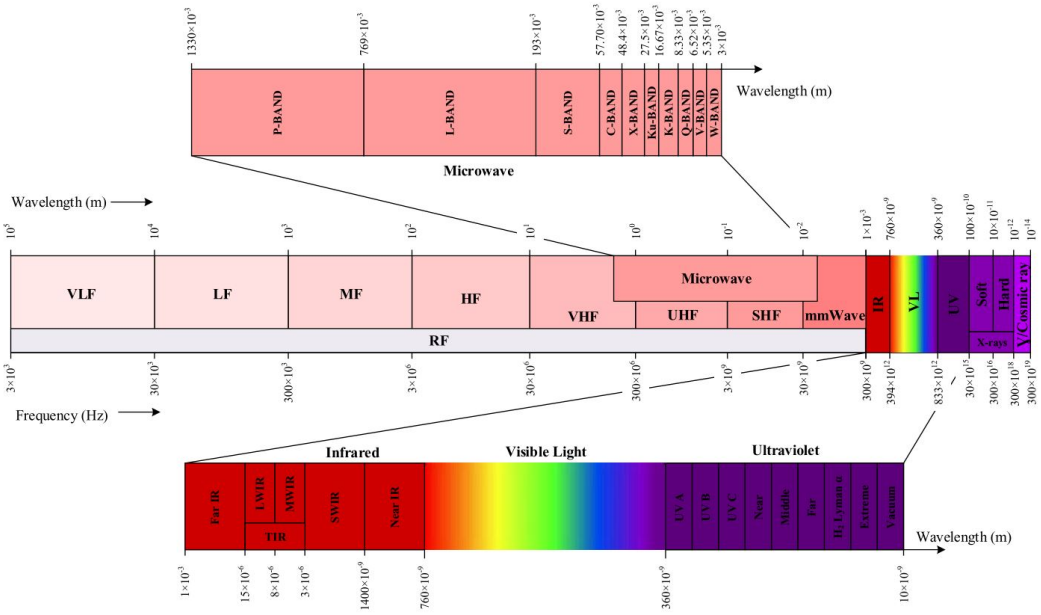


Figure 1.1: Electromagnetic Spectrum [1]

investigating micro-LEDs, laser diode with diffusers to further improve the bandwidth of VLC transmitter [13]. Nonetheless, the universal availability of LEDs, license-free deployment, and Gbps order data rate makes VLC an attractive choice for indoor communications. The first generation of VLC devices are already available from several vendors such as PureLiFi, OledComm, Philips, VLNComm and Velmenni. According to a recent market report, VLC market size is anticipated to reach 80 Billion USD by 2030 [14]. Thus, both IEEE and ITU have initiated efforts for VLC standardization in the form of IEEE 802.15.13 Task Group [15], IEEE 802.11.bb [16] and ITU-T G.vlc [17].

The choice of modulation scheme plays a crucial role for ensuring high data rates in a communication network. Due to the the non-coherent nature of LED transmitters, the conventional RF modulation schemes can not be directly used in VLC. Thus, VLC utilizes intensity modulation with direct detection (IM/DD) technique for communication, which requires real and positive transmit signal. In IEEE 802.15.7, many single-carrier modulation techniques such as on-off keying (OOK) , M-ary pulse-amplitude modulation (M-PAM) , and M-ary pulse position modulation (M-PPM) and color shift keying (CSK) were proposed for VLC. However, the demand for spectrally efficient high data-rate communication motivated the introduction of VLC multi-carrier modulation schemes [18]. Orthogonal frequency division multiplexing (OFDM) has been proposed for low bandwidth (LB) and high bandwidth (HB) PHY modes of IEEE 802.15.13. OFDM has several advantages over single carrier schemes: it achieves high data-rate by using multiple orthogonal subcarriers to concurrently transmit parallel data streams, eliminates the need for complex equalizers, embodies an inherent resilience to combat ISI; and

straightforward for medium access (MA) . However, the conventional OFDM symbol is bipolar and complex. In order make OFDM compatible with IM/DD, the complex bipolar signal needs to be converted it into real and unipolar signal, the resultant is known as Optical-OFDM (O-OFDM) . One of the major draw back of O-OFDM system is its high peak-to-average power ratio (PAPR) . Since the time domain O-OFDM is generated by addition of multiple subcarriers with distinct frequencies, it is possible to have constructive addition of various subcarriers. This can result into a relatively higher instantaneous power than the average power, which results in high PAPR. This high PAPR due to O-OFDM modulation can cause severe clipping distortion that can result into degradation of system performance. In addition, a high PAPR reduces the illumination to communication conversion efficiency [19] and lifetime of the LED. Therefore, in this thesis, we have explored double precoding based method termed as Double Precoded O-OFDM (DP-OOFDM) for reducing the PAPR of O-OFDM, and evaluated its performance in terms of complexity, spectral efficiency, PAPR, power-saving and symbol-error-rate (SER) against conventional discrete fourier transform (DFT)-precoded OOFDM [20] and O-OFDM. Although this method provides ultra low PAPR, good SER and power saving, it provides limited support for future communication requirements, such as machine type communication (MTC), tactile internet, machine-to-machine (M2M) communication, bitpipe communication and wireless regional area network (WRAN). Applications like MTC and M2M communication work over low power, therefore making strict synchronization unaffordable. Thus, an alternative flexible multicarrier approach which enables the mix of synchronous/asynchronous and orthogonal/non-orthogonal traffic types is required for the next generation. Generalized frequency division multiplexing (GFDM) is one such potential candidate as it is based on block structure of $NJ$ samples, where each of the $N$ subcarriers carry $J$ subsymbols. GFDM turns into OFDM when $J = 1$, and single carrier with single carrier frequency domain equalization when $N = 1$. In GFDM, a single cyclic prefix (CP) is added for entire block that contains multiple subsymbols, resulting into improved spectral efficiency of the system. This improved spectral efficiency can be traded for an additional redundancy which leads to relaxation in synchronization requirements of multiple users in an MTC scenario. GFDM can also fulfill low latency requirement for tactile internet and vehicle-to-vehicle applications by utilizing its flexible block structure [21]. The flexible nature of GFDM makes it a suitable candidate for future communication networks. Therefore, we have proposed optical generalized frequency division multiplexing (O-GFDM) for VLC physical layer in this thesis.

The physical layer of VLC only supports point-to-point communication whereas light fidelity (LiFi) can be built over the VLC physical layer to support fully networked, bidirectional, high-speed optical wireless communication. LiFi utilizes the visible light spectrum for downlink and the infrared spectrum or WiFi for the uplink. The support of mobility, handover, and illumination is mandatory in LiFi. LiFi is a wireless networking extension of VLC that supports

multiuser, bidirectional, multicast, or broadcast communication. LiFi deployment requires multiuser techniques, resource allocation algorithms, and security strategies [1, 22]. There are various advantages of LiFi over WiFi:

- **High spatial data rate:** LiFi can potentially utilize massive bandwidth of visible spectrum to achieve high data rates. Although the off-the-shelf LEDs practically have limited bandwidth, literature has reported that LiFi can achieve a speed over 15 Gbps [23] as compared to 10 Gbps which is the top speed of WiFi IEEE 802.11ax [24]. Moreover, the coverage of a LiFi AP is spatially confined to a small region known as attocell. These small attocells facilitate spatial bandwidth reuse, thus improves spatial-spectral efficiency.

- **High security:** Unlike WiFi signals which can penetrate through opaque objects, LiFi signals cannot pass through opaque structures and thus, they are confined to the room for the intended communication. Furthermore, as the coverage area of attocell is relatively smaller than WiFi thus, LiFi can provide higher security compared to WiFi.

- **High utility and power efficiency:** LiFi can enable the existing illumination infrastructure to provide communication, resulting into higher utility. Furthermore, LiFi can significantly improve energy efficiency [25].

Despite these advantages, LiFi has some limitations. Since light-wave cannot penetrate through opaque objects, LiFi suffers from a major drawback of blockage. Furthermore, as all the LiFi access points (APs) in a room operate on the same frequency, there exists co-channel interference (CCI) between LiFi APs. Consequently, the LiFi throughput fluctuates spatially which results into various coverage holes in an indoor LiFi environment. LiFi can support high data rates when the receiver is in direct line-of-sight (LoS) , but as soon as the LoS connection is lost, the data rate drops significantly; on the contrary, WiFi can support moderate data rates with more ubiquitous coverage. Thus, to ensure the user's quality of services (QoS) , it is suggested to use LiFi technology as an additional layer within the existing WiFi networks to form heterogeneous LiFi WiFi network (HLWN) . The coexistence of LiFi and WiFi technologies is possible because of their nonoverlapping spectrums. In [26], it has been shown that a HLWN provides higher system throughput as compared to standalone LiFi or WiFi networks. An appropriately designed HLWN can support higher data rate, better user satisfaction, outage performance, and lower handover rates [27]. For HLWN, load balancing (LB) includes AP assignment, resource allocation and handover management. LB in HLWNs is challenging as LiFi's and WiFi's coverage areas overlap with each other and WiFi covers larger area but has lower capacity; this increases the complexity of AP selection process. If the conventional received signal strategy (RSS) is applied for AP assignment in HLWN, WiFi

AP will be susceptible to over-load, and the system would not be able to ensure the required QoS. The problem of load balancing of HLWN is a non-convex mixed-integer nonlinear programming (MINLP) optimization problem, it is mathematically intractable, consequently, the conventional optimization methods fail to provide an optimal global solution. Therefore, in this thesis, we have explored reinforcement learning (RL) based LB for HLWNs. Furthermore, most of the existing literature considered that a HLWN user could either connect to a LiFi AP or WiFi AP at a given point, however, in [28, 29] authors have implemented channel aggregation for HLWN, and demonstrated proof-of-concept by using state-of-the-art LiFi and WiFi frontends. Motivated by them, in this thesis, we have proposed a RL based LB algorithm for link aggregation enabled HLWNs which provides near optimal performance at fairly low complexity.

## 1.2 Objectives

The main aim of this dissertation is to improve both the PHY and MAC layer of VLC. Specifically, this Ph.D was funded by Intel India and the objectives were defined according to the MoU, which are as follows:

- To improve the VLC physical layer by investigating methods to reduce the PAPR of O-OFDM and advanced modulation schemes for future communication requirements.
- To improve the performance of HLWN by designing a low complexity near-optimal load balancing algorithm.
- To design an efficient LB algorithm for link aggregation enabled HLWNs with more realistic system modeling.

## 1.3 Major Contributions

The major contributions of this dissertation and relevant publications are summarized below.

- In order to improve VLC physical layer, two major works have been investigated in this thesis. First, DP-OOFDM is proposed to reduce the PAPR of O-OFDM. DP-OFDM for the first time analyse the performance of real and imaginary part separation based grouped DFT precoded OFDM in conjunction with Gaussian-minimum-shift-keying (GMSK) based pulse shaping for VLC system. A comprehensive performance analysis of proposed DP-OOFDM in-terms of PAPR, power saving, SER, spectral efficiency and computational complexity against conventional DFT-precoded OOFDM and O-OFDM is

provided. Furthermore, the analytical PAPR expressions for DP-OOFDM were derived and results are validated through simulations. Second, an alternative flexible multi-carrier approach known as O-GFDM has been investigated for VLC to cater future wireless communication requirements. The O-GFDM significantly reduces the PAPR compared to O-OFDM counterpart. The analytical SER expressions for O-GFDM SER was derived and results are validated through simulations. The O-GFDM provides higher spectral efficiency and significant power saving compared to DCO-OFDM counterpart.

  - **Rizwana Ahmad**, and Anand Srivastava."*PAPR Reduction of OFDM Signal Through DFT Precoding and GMSK Pulse Shaping in Indoor VLC*." IEEE ACCESS, vol. 8, pp. 122092-122103. 2020.
  - **Rizwana Ahmad**, and Anand Srivastava. "*Optical GFDM: an improved alternative candidate for indoor visible light communication*." Photonic Network Communications, vol. 39, no. 2, pp. 152-163. 2019.
  - **Rizwana Ahmad**, Anand Srivastava, and Hossam AI Selmy. "*Advanced modulation techniques for low PAPR in vlc system*." in IEEE 20th International Conference on Transparent Optical Networks (ICTON), Bucharest, Romania, July 2018.
  - **Rizwana Ahmad**, Anand Srivastava, and Hossam A. I. Selmy "*Novel modulation scheme for VLC*", Proceedings of SPIE OPTO, Broadband Access Communication Technologies XII, 105590K, San Francisco, California, United States, Jan. 2018.

- A RL based load balancing algorithm is designed for HLWN. The reward function of RL was carefully crafted to increase the average system throughput while ensuring the required QoS. The convergence and effectiveness of this algorithm were studied under different mobility models. The performance of the proposed algorithm is compared against benchmark in terms of complexity, average throughput and user satisfaction. It is shown that the RL based LB can achieve a near-optimal performance with a lower complexity as compared to RSS and exhaustive search methods.

  - **Rizwana Ahmad**, Mohammad Dehghani Soltani, Majid Safari, Anand Srivastava, and Abir Das. "*Reinforcement learning based load balancing for hybrid LiFi WiFi networks.*" IEEE Access, vol. 8, pp. 132273-132284, 2020.
  - **Rizwana Ahmad**, Mohammad Dehghani Soltani, Majid Safari, and Anand Srivastava. "*Load Balancing of Hybrid LiFi WiFi Networks Using Reinforcement learning.*" in 2020 IEEE 31st Annual International Symposium on Personal, Indoor and Mobile Radio Communications (PIMRC). London. pp. 1-6.

  - **Rizwana Ahmad**, and Anand Srivastava. "*Optimized User Association for Indoor Hybrid Li-Fi Wi-Fi Network.*" in 2019 IEEE 21st International Conference on Transparent Optical Networks (ICTON), Angers, France. pp. 1-5.

- For a link aggregation enabled HLWNs, a centralized RL based LB algorithm is proposed. This work considers a more realistic system model that takes into account the effect of receiver orientation and handover overhead. Furthermore, domain knowledge is included to reduce the action space which in turn reduces the complexity. The performance of the algorithm for different reward functions is evaluated and compared against the benchmark in terms of complexity, average throughput and user satisfaction.

  - **Rizwana Ahmad**, Mohammad Dehghani Soltani, Majid Safari, and Anand Srivastava. "Reinforcement Learning-based Near-Optimal Load Balancing for Heterogeneous LiFi WiFi network". Accepted in IEEE System Journal, 2021.

## 1.4 Thesis Layout

The rest of the thesis is organised as follows:

Chapter 2 presents the VLC system overview. Initially, the necessary background knowledge about VLC along with its applications and system model is briefly explained followed by, a more detailed explanation of optical VLC channel. Afterwards, various VLC modulation schemes including O-OFDM are discussed. Further, the possible impairments in a VLC system are reviewed. Finally, an ALA based predistorter is proposed to mitigate the effect of LED non-linearity and its performance is compared against VLC system with ideal linear LED. Overall, the impact of nonlinear LED on O-OFDM system has been mitigated to improve its performance.

In chapter 3, a further improvement in performance of O-OFDM system is investigated by employing PAPR reduction method termed as DP-OFDM. DP-OFDM is real and imaginary part separation based grouped DFT precoded OFDM in conjunction with GMSK based pulse shaping for VLC system. This chapter provides a comprehensive performance evaluation of DP-OOFDM against O-OFDM, in-terms of PAPR, power saving, SER, spectral efficiency, and computational complexity. Further, analytical expression for DP-OFDM PAPR is derived in this chapter.

Chapter 4 investigate the performance of an alternative flexible multi-carrier modulation technique i.e., generalized frequency division multiplexing (GFDM) for VLC. In this chapter, the performance of two variants of GFDM for VLC namely, O-GFDM with DC (OGFDM-DC) and without DC bias (OGFDM-NDC) have been evaluated against corresponding O-OFDM counterparts. A comprehensive performance analysis in-terms of spectral efficiency,

complexity, power saving, PAPR, SER, and subcarrier frequency shift tolerance is provided in this chapter. Furthermore, this chapter also provides an analytical derivation of O-GFDM SER expression.

Chapter 5 provides overview of LiFi and its coexistence with WiFi. Initially, the background of LiFi and HLWN network is briefly explained. Afterwards, the HLWN system model used in subsequent chapters is discussed. Finally, an optimization based load balancing algorithm for HLWN is proposed and evaluated against RSS method.

In chapter 6, a low complexity near-optimal centralized RL based dynamic load balancing algorithm for HLWN is proposed to maximize user QoS. The performance of this algorithm has been compared against the state-of-the-art signal strength strategy (SSS), iterative optimization method and exhaustive search based on computational complexity, average network throughput, user satisfaction, fairness and capacity outage probability. Additionally, two different mobility models, namely, random waypoint (RWP) and hotspot random waypoint (HRWP) have been explored in this work, to illustrate the robustness of the proposed algorithm.

In chapter 7, link aggregation enabled HLWN is explored and an efficient RL based load balancing is proposed for LA enabled HLWN. Furthermore, a more realistic framework with orientation-based random waypoint (ORWP) mobility model, carrier-sense multiple access with collision avoidance (CSMA/CA)-based multi-user access, and handover overhead is discussed in this chapter. Moreover, this chapter extensively covers design of reward function according to the objectives and demonstrates that a particular reward design is able to provide both high average network throughout and user satisfaction. In addition, it introduces the concept of domain knowledge to reduce the complexity of RL load balancing algorithm at the cost of marginal performance degradation.

Chapter 8 concludes the dissertation and suggests the possible future research directions.

## 1.5 Summary

The rapid growth in mobile data traffic have motivated researchers to consider investigate alternative communication technologies to support the future communication network requirements. VLC is one of the potential technology, which operates in the visible light spectrum and utilizes the illumination LEDs for communication. In order to fully efficiently utilizes the spectrum, O-OFDM modulation has been proposed for VLC. While the O-OFDM provide high data rates, it suffers from the problem of high PAPR, which causes clipping distortion, and reduces the illumination-to-communication conversion efficiency. Therefore, in this thesis, more efficient low PAPR modulation scheme for the VLC physical layer have been investigated. Furthermore, LiFi can be built over the physical layer of VLC to provide fully networked, bidirectional, high-speed optical wireless communication. However, since light cannot penetrate through

opaque objects, LiFi is prone to blockages; hence it can support high data rates in specific areas only. On the other hand, the WiFi communication technology (WiFi) can support moderate data rates with more ubiquitous coverage. As the spectrum of WiFi and LiFi are non-overlapping, both of the technologies can coexist to form heterogeneous LiFi WiFi network (HLWN). The load balancing strategy plays a critical role in the overall performance of a HLWN. Therefore, in the second part of this thesis, various intelligent load balancing strategies for heterogeneous LiFi WiFi network (HLWN) have been investigated.

Chapter 2

# VLC Background and Overview

In this chapter, background and applications of VLC are discussed in Section 2.1. Followed by Section 2.2 which provides a brief overview of a typical VLC system. More details related to VLC physical layer such as channel model and modulation schemes are discussed in Section 2.3 and 2.4. Various impairments present in a VLC system including thermal noise, shot noise and LED non-linear distortions are discussed in Section 2.5. In Section 2.5.2, effect of LED nonlinearity on a VLC system is evaluated and an adaptive-learning-architecture (ALA) based predistortion algorithm is proposed to mitigate the effect of LED nonlinearity.

## 2.1 Background

The first use of optical wireless communication (OWC)) dates back to 1880 when Alexander GrahamBell invented a photo-phone to transmit audio signals by modulating sunlight [30]. With recent advancements in solid-state lighting, LEDs reliability, lifespan, cost, and energy efficiency have significantly improved; consequently, LEDs are forecasted to take over nearly 84% of illumination infrastructure by the year 2030 [31]. Furthermore, LEDs can switch to different light intensity levels at a high- rate; this allows LEDs to be used for illumination and high-speed communication simultaneously. Motivated by this, Komine and Nakagawa, developed a digital communication system using white-LEDs and referred to it as VLC [32]. Afterwards, VLC Consortium (VLCC) was founded in 2007 to standardize the VLC technology. The vast bandwidth in the unlicensed band, existing infrastructure, low power consumption, and no electromagnetic interference make VLC an attractive option for various applications. Some of them are as follows:

- Wireless connectivity: VLC can be used to provide very-high-speed wireless connectivity with inherent security. Currently, VLC can provide a data rate of over 15 Gbps [23] using off off-the-shelf LEDs.

- Aviation: In aircraft, RF communication is undesirable as it can cause interference in navigational equipment. Thus, VLC can utilize the existing illumination LEDs of aircraft for multimedia delivery to passengers. In 2019, Air France Airbus A321 demonstrated the first in-flight use of VLC.

- V2X communication: The presence of LED-based headlamps in most vehicles and LED-based traffic lights and street lamps enables the use of VLC for high-speed communication between vehicle-to-vehicle and vehicle-to-infrastructure. The current achievements and research challenges associated with the use of VLC for V2X communication are summarized in [33].

- Underwater communications: The acoustic navigation and positioning technology is limited by bandwidth whereas the RF communication requires huge antenna size, large transmitter power and suffers from high attenuation. On the contrary, VLC can provide higher data rates than the traditional acoustic systems with significantly lower power consumption and complexities for short-range communication [34].

- Hospitals: Conventional RF-based communication is undesirable in electromagnetic wave-sensitive areas, such as around MRI scanners and operation theaters, because they may cause interference. Instead, VLC can be used in hospitals.

- Smart displaying signboards: In modern days, signboards are used everywhere, including shopping malls, roads, airports, and bus stops. These signboards are formed by an array of LEDs, that can be used for broadcasting information by utilizing VLC.

- Location-based services: Most public spaces already have LED based illumination; thus VLC based localization systems can be easily implemented with little additional equipment [35]. In factories, VLC based localization can be used to locate employees and assets efficiently. In shopping malls, it can aid efficient navigation and personalized shopping experiences.

## 2.2 A Typical VLC system

The basic block diagram of a typical VLC system is shown in Fig. 2.1. In an indoor VLC system, LED is commonly used as the transmitter front-end. Due to incoherent nature of the LED, the data is modulated only into light intensity, rather than amplitude and phase. Therefore, the simplest method of IM/DD technique is used in VLC. As illustrated in Fig. 2.1, the input data after being coded based on source, channel or precoding methods is modulated and then the modulated data is made compatible with LED front-end by converting the modulated signal

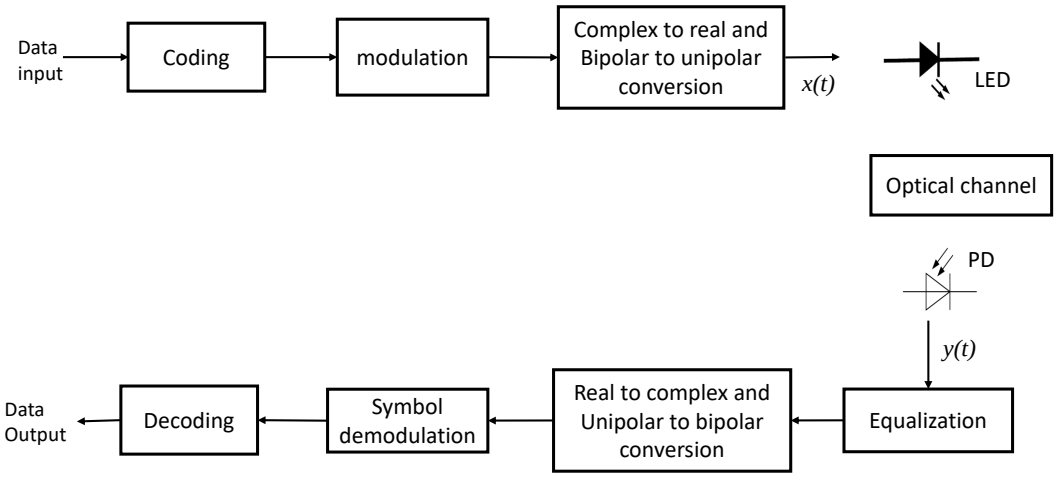


Figure 2.1: A Typical VLC system

into real and unipolar signal. Afterwards, the signal $x(t)$ is used for intensity modulation of the LED, and the LEDs output signal travels through the channel to reach the optical receiver. At the receiver, optical filters are employed to confine the spectrum of light, weaken the impact of ambient light sources and for blue filtering. Afterwards, the filtered light is concentrated on the photo-detector (PD) via an optical concentrator. The PD converts the incoming optical signal into equivalent electrical signal which is amplified via a trans-impedance amplifier (TIA) to provide signal $y(t)$ for data demodulation. It is important to notes that the choice of modulation scheme plays a crucial role in performance of the VLC system. More details about the modulation schemes, optical channel and impairments present in a VLC system are discussed in subsequent section.

## 2.3 Optical Channel

The VLC optical channel can be modelled as:

$$y(t) = R_{\mathrm{PD}}\, x(t) * h(t) + n(t) \tag{2.1}$$

where, "*" stands for a convolution operator, $R_{\mathrm{PD}}$ indicates the responsivity of the PD, $h(t)$ denotes the impulse response of the optical channel, and $n(t)$ is the additive white Gaussian noise (AWGN) which represents the cumulative noise present in VLC system, explained in Section 2.5.1. The impulse response $h(t)$ can be expressed as:

$$h(t) = h_{\mathrm{LoS}}(t) + h_{\mathrm{NLoS}}(t) \tag{2.2}$$

where $h_{\text{LoS}}(t)$ is the impulse response of the line-of-sight optical channel, i.e., the direct link between the LED and PD and $h_{\text{NLoS}}(t)$ is the impulse response of the non-line-of-sight (NLoS) optical channel, i.e., diffused components taking into account the reflections from the walls. Fig. 2.2 shows the LoS link and NLoS link between the LED and PD. The optical channel in frequency domain is given as:

$$H(f)_{\text{LiFi}} = H(f)_{\text{LoS}} + H(f)_{\text{NLoS}} \tag{2.3}$$

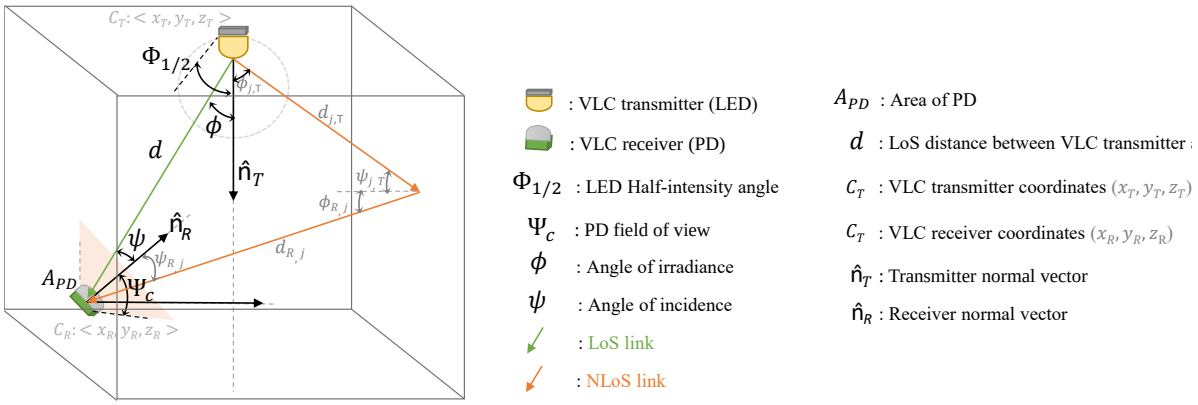


Figure 2.2: Typical VLC channel with LoS (green) and NLoS (orange) link

### 2.3.1 LoS Link

The light emitted by LED can be modelled as Lambertion radiation $R(\phi)$ following the spatial distribution function $\cos^m(\phi)$, which can be modelled as [32, 36]:

$$R(\phi) = \frac{(m+1)\cos^m(\phi)P_t}{2\pi} \tag{2.4}$$

where $\phi$ represents the angle of irradiation, $m$ denotes the Lambertian order which specifies the directionality of the source, and $P_t$ is the transmitted optical power. The value of $m$ can be calculated from the source half-angle, $\Phi_{1/2}$, which is defined as:

$$\Phi_{1/2} = \arccos(0.5)^{\frac{1}{m}}. \tag{2.5}$$

The PD at the receiver is responsible for converting the optical power into electrical current, and it has various associated parameters which include physical area of PD $A_{PD}$ , the receiver's field of view (FoV) $\Psi_c$ .

The direct LoS link between LED and PD can be modeled as [37]:

$$h_{LoS}(t) = \begin{cases} \frac{R(\phi)A_{PD}\cos(\psi)}{d^2}\delta(t-\frac{d}{c}) & : \ \psi < \Psi_c \\ 0 & : \ \psi > \Psi_c \end{cases} \tag{2.6}$$

where, $d$ is the distance between the transmitter and receiver, $\delta(.)$ is the Dirac delta function, $c$ is the speed of light. The angle of irradiance $\phi$, is the angle of view (relative to normal direction) of the receiver position when looking from the transmitter, can be expressed as:

$$\cos(\phi) = \widehat{n}_T \frac{(C_R - C_T)}{||d||}, \tag{2.7}$$

The angle of light incidence at the receiver $\psi$, is the angle of view (relative to normal direction) of the transmitter position when looking from the receiver, It can be given as:

$$\cos(\psi) = \widehat{n}_R \frac{(C_T - C_R)}{||d||}. \tag{2.8}$$

where $\widehat{n}_T$ and $\widehat{n}_R$ are the orientations of the transmitter and receiver respectively. The positions of source and receiver are $C_T$ and $C_R$ respectively. The DC channel gain for LoS is defined as [9]:

$$H(0)_{\text{LoS}} = \frac{(m+1)A_{\text{PD}}}{2\pi d^2}\cos^m(\phi) g_{\text{f}} g_{\text{c}}(\psi)\cos(\psi), \tag{2.9}$$

where, $g_{\text{f}}$ denotes the gain of the optical filter; and $g_{\text{c}}$ defines the gain of optical concentrator, and is given as:

$$g_{\text{c}}(\psi) = \begin{cases} \frac{n^2}{\sin^2(\psi)}, & 0 \le \psi \le \Psi_c \\ 0, & \psi > \Psi_c \end{cases} \tag{2.10}$$

where $n$ is the refractive index of the concentrator.

### 2.3.2 NLOS Link

For the NLOS link, the light rays reaching to the PD after being reflected from different walls of the room are considered. The channel gain for NLOS component is defined as [38]:

$$H(f)_{\text{NLOS}} = \frac{\rho A_{\text{PD}} e^{j2\pi f \Delta T}}{A_{\text{room}}(1-\rho)(1+j\frac{f}{f_c})} \tag{2.11}$$

where $\rho$ is the reflectivity of the walls, $A_{\text{room}}$ is the area of the room, $\Delta T$ is the delay between the LOS and onset of the diffused signals, and $f_c$ is the cut-off frequency of the diffuse optical channel [39].

## 2.4 VLC Modulation Schemes

In VLC, since the same LED is responsible for both illumination and communication, the modulation schemes need to satisfy the illumination requirements along with reliable communication. Thus, they should provide a particular luminous flux, support dimming, and ensure no flickering, i.e, change in light intensity should be faster than perceptible human vision (200 Hz). Accordingly, IEEE 802.15.7 and 802.15.13 have proposed the following modulation schemes for the VLC physical layer.

### 2.4.1 On-off Keying (OOK)

OOK is the simplest modulation scheme in which when '1' has to be transmitted the LED is turned 'ON', whereas when '0' has to be transmitted LED is turned 'OFF'. It must be noted that 'OFF' state does not imply turning off the LED rather it indicates that the light intensity being significantly reduced. OOK is easy to implement but can support only limited data rate with off-the-shelf components [18]. At higher transmission speeds, OOK pulse bandwidth exceeds the LED 3-dB bandwidth, thus, the OOK modulation schemes begin to suffer from the undesired effects of inter-symbol interference (ISI) [40]. Therefore, limiting the datarate.

### 2.4.2 Variable Pulse Position Modulation (VPPM)

VPPM uses PPM to provide communication and PWM to support dimming control. In case of VPPM, the position of the pulse is modulated according to data and pulse width is modulated according to the dimming requirement. The advantage of this modulation is that the amount of dimming does not effect the communication, as long as there is some illumination [2]. Fig 2.3 illustrates an example of VPPM.

### 2.4.3 Color Shift Keying (CSK)

CSK uses the red-green-blue (RGB) LEDs as transmitter. Specifically, in CSK, the binary data is first mapped on to x and y chromaticities by using the colour space chromaticity diagram, after that these chromaticities are converted to the intensities $R_t$, $G_t$ and $B_t$ that can ensure the white light. Finally, these intensities are transmitted by the RGB LED. Fig. 2.4(a) and 2.4(b) illustrates the block diagram of a typical CSK system and colour space chromaticity diagram.

### 2.4.4 Multiband carrier-less amplitude and phase modulation (m-CAP)

carrier-less amplitude and phase (CAP) modulation transmit two streams of data in parallel, similar to QAM. However, in contrast to QAM, CAP does not rely on a carrier, but uses orthog-

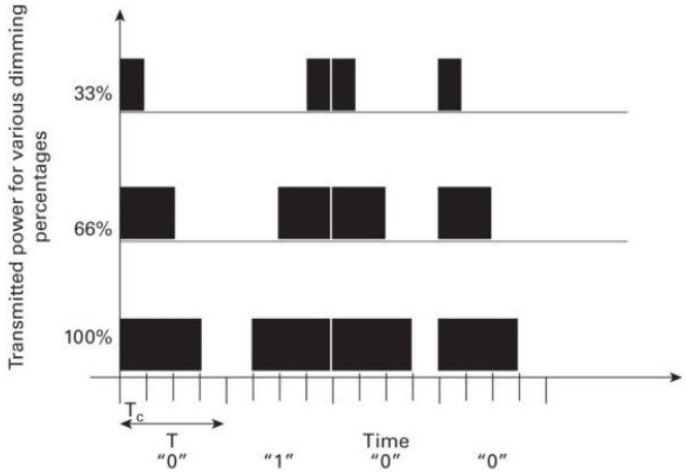


Figure 2.3: Variable pulse position modulation (VPPM) with different dimming percentages, where the encoded information is “0 1 0 0" [2].

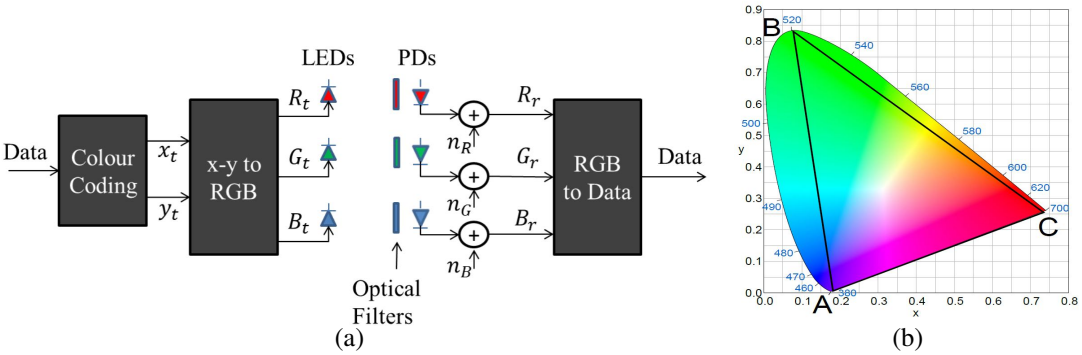


Figure 2.4: A typical CSK based VLC system: (a) Block diagram [3] (b) Colour space chromaticity diagram (CIE 1931) [3]

onal waveform filters to separate the data streams. Thus, makes CAP receivers simpler than QAM without compromising on the spectral efficiency and performance. Fig. 2.5 illustrates the block diagram of m-CAP based VLC system.

Nonetheless, CAP is highly sensitive to non-flat channels, and requires complex equalizers for frequency selective channels. Thus, for non-flat VLC, a multiband form of CAP (m-CAP) has been proposed [4, 41]. The m-CAP splits the total signal bandwidth into m equally spaced sub-carriers, in order to relax the flat-band response requirement by allocating a narrow bandwidth to individual subcarriers. However, the major disadvantage of m-CAP is that it significantly increases the computational complexity of the system, as it requires 2m finite impulse response (FIR) filters at the transmitter and additional 2m FIR filters at the receiver. Thus, an m-CAP signal in total requires 4m [41].

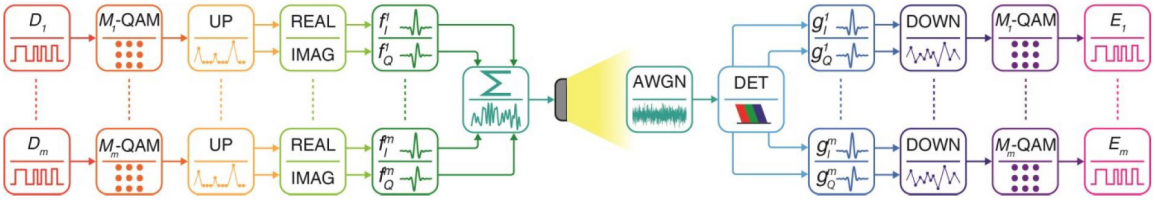


Figure 2.5: Block diagram of m-CAP based VLC system [4].

### 2.4.5 Orthogonal Frequency Division Multiplexing (OFDM)

One limitation of previously discussed single-carrier modulation schemes is that they suffer from high inter-symbol interference due to non-linear frequency response of LEDs. OFDM has been widely adopted in VLC because of its high spectral efficiency and robustness against inter-symbol interference.

For VLC, the transmitted signal needs to be real and positive. Therefore, the complex bipolar OFDM signal is required to be converted to real unipolar signal. For this purpose, Hermitian symmetry is applied to convert complex OFDM signal into real signal. Further, in order to obtain a unipolar OFDM signal, there are various techniques which are used namely, DC biased optical OFDM (DCO-OFDM): DC bias is added to the bipolar OFDM signal, asymmetrically clipped optical OFDM (ACO-OFDM): the bipolar signal is clipped at zero level and only the positive part of the signal is transmitted and Flip-OFDM: the positive and negative parts of the bipolar OFDM signal are extracted into two separate subframes, and subframe containing negative part is flipped in polarity, thus resulting into positive valued signal [42]. DCO-OFDM is more spectral efficient as compared to ACO-OFDM and Flip-OFDM, but less power efficient [43]. The block diagram of O-OFDM is shown in Fig. 2.6. The incoming bits are converted from serial to parallel and modulation is performed. Following that frame mapping and Hermitian symmetry is applied, in order to obtain real valued bipolar signal after inverse fast Fourier transform (IFFT) operation. Different variant of O-OFDM uses different techniques to convert this bipolar signal into unipolar signal. In ACO-OFDM, only odd subcarriers carry information and zero level clipping is performed before transmission, resulting into unipolar signal. In case of flip-OFDM, the polarity separator extracts the positive and negative parts of real valued bipolar signal into two frames. These frames are multiplexed such that first subframe contains positive part and second subframe contains flipped negative part, therefore, the resultant frame has real unipolar values. In [42], authors have reported that the performance and spectral efficiency of Flip-OFDM and ACO-OFDM are same and they both are non-DC techniques. Hence, they can be considered equivalent, except for the receiver complexity. In case of DCO-OFDM, a real valued unipolar signal is obtained by adding appropriate DC bias to the bipolar signal. Thus, for DCO-OFDM the information is carried over $(N/2-1)$ subcarriers, whereas, for ACO-OFDM information is carried over $N/4$

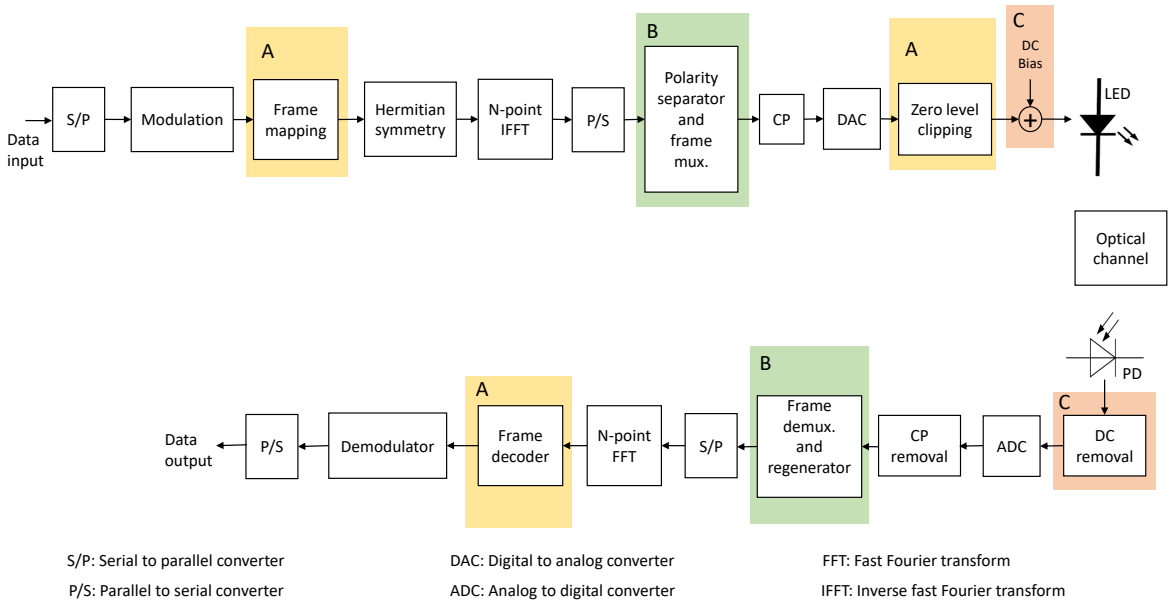


Figure 2.6: Block diagram of O-OFDM, where ACO-OFDM: Basic + A, Flip-OFDM: Basic + B, DCO-OFDM: Basic + C, and 'Basic' are unshaded blocks.

subcarriers, provided $N$ is the total number of subcarriers. DC bias added in DCO-OFDM results into higher PAPR, therefore, making it less power efficient [43]. Additionally, high PAPR causes clipping distortion, which results in performance degradation [44].

## 2.5 Impairments in VLC

### 2.5.1 Noise component

There are three prime noise sources present in a VLC system. First, ambient noise due to solar radiations or fluorescent lamps presence in proximity of VLC receiver. It is hard to model but its effect can be reduced using appropriate optical and electrical filters at the receiver. Second, shot noise in the PD due to intrinsic randomness in the photon's particle characteristics. It increases with an increase in light intensity. For a large number of photons, this can be modelled as an additive white Gaussian noise (AWGN). Third, thermal noise because of random thermal motion of electrons in the receiver circuit. The resistance of the transimpedance amplifier (TIA) is a major source of thermal noise. This noise can also be modelled as an AWGN. Thus, the power of the overall noise in a VLC system can be modelled as:

$$\sigma^2 = \sigma^2_{shot} + \sigma^2_{thermal} \tag{2.12}$$

where, $\sigma^2_{shot}$ and $\sigma^2_{thermal}$ indicates the power of shot and thermal noise respectively. They are described as:

$$\sigma^2_{shot} = 2qR_{\mathrm{PD}}P_{\mathrm{opt}}B + 2qI_{\mathrm{BG}}I_2B \tag{2.13}$$

where, $q$ is the electron charge, $P_{\mathrm{opt}}$ represents the average received optical power, B is the noise bandwidth which is determined by the minimum of signal modulation bandwidth or the receiver bandwidth that has been used [45]; $I_{\mathrm{BG}}$ indicates the background current; and $I_2$ denotes the noise bandwidth factor.

$$\sigma^2_{thermal} = \frac{4k_BT_kB}{R_L} \tag{2.14}$$

where, $k_B$ is the Boltzmann's constant, $T_k$ is the absolute temperature in Kelvin and $R_L$ represents receiver equivalent load resistance.

### 2.5.2 Nonlinear Distortions

Apart from these previously discussed noise components, a VLC system also suffers from clipping and nonlinear distortion caused due to limited dynamic range of LED. Both the voltage-current relationship and the current-light intensity relationship in the LED are nonlinear [46]. Thus, the optical power emitted by LED $P_{out}$ follows an nonlinear relationship with input current signal $I_{in}(t)$, as show in Fig. 2.7.

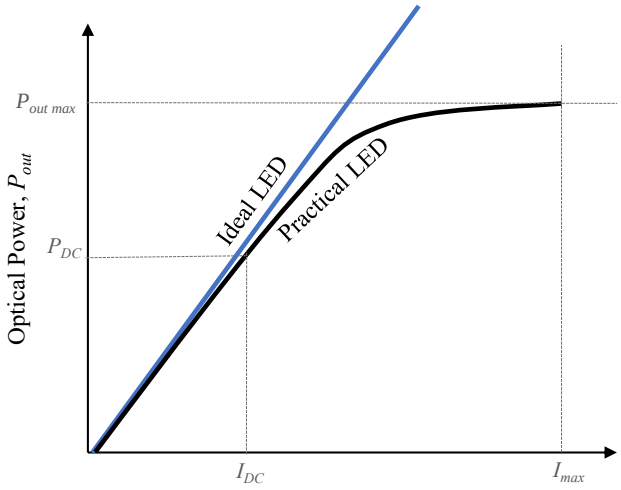


Figure 2.7: LED transfer characteristic: Practical (black) and Ideal (blue)

In this work, a quadratic polynomial is used to characterize the nonlinear behavior of LED [47]. It can be expressed as:

$$P_{out} = b_0 + b_1\left(I_{in}(t) - I_{DC}\right) + b_2\left(I_{in}(t) - I_{DC}\right)^2 \tag{2.15}$$

where, $I_{DC}$ is the normalized bias current to the LED, and the nonlinearity coefficients $b_0$, $b_1$ and $b_2$ can be defined as:

$$b_0 = \zeta_{NL}, \quad b_1 = 1 \quad b_2 = -4\zeta_{NL} + 2 \tag{2.16}$$

where $\zeta_{NL}$ controls the severity of nonlinearity. According to the LED type, the experimental value of $\zeta_{NL}$ varies in a range of 0.5 to 0.75 [48]. $I_{DC}$ represents the normalized bias current which is set to 0.5 [47]. The LED nonlinearity significantly degrades the performance of O-OFDM [49]. In literature, various predistortion and postdistortion techniques have been proposed to mitigate the effects of LED nonlinear distortion [50–56]. To the best of our knowledge, although the schemes in literature have shown considerable performance improvement, however, none of them have compared the performance against a linear DCO-OFDM system [57]. We propose a novel ALA-based predistortion algorithm to mitigate the effect of LED nonlinearity in VLC system. ALA is a two step learning algorithm. First step includes error measurement and decision making and second step is coefficient estimation. Firstly, the error between the input DCO-OFDM signal $x(n)$ and the LED output signal $y(n)$ is measured in terms of error vector magnitude (EVM) which can be expressed as [58]:

$$\text{EVM} = \frac{\sqrt{\frac{1}{N}\sum_{k=0}^{N-1}\left((I(y_k) - I(x_k))^2 + (Q(y_k) - Q(x_k))^2\right)}}{\sqrt{\frac{1}{N}\sum_{k=0}^{N-1}\left((I(x_k))^2 + (Q(x_k))^2\right)}}, \tag{2.17}$$

where $I(y_k)$ and $Q(y_k)$ are the in-phase and quadrature phase components at the $k^{th}$ subcarrier of the observed signal $y(n)$, and $I(x_k)$ and $Q(x_k)$ are the in-phase and quadrature phase components at the $k^{th}$ subcarrier of the input DCO-OFDM signal $x(n)$. The measured EVM is then compared with threshold EVM ($EVM_T$) for decision-making. The value of $EVM_T$ typically depends on the quality of service (QoS) requirement of a DCO-OFDM based VLC system. It can be calculated from the desired bit error rate (BER) or signal-to-noise ratio (SNR) [58]. If the measured EVM $< EVM_T$, no further coefficient estimation is required and the output signal becomes linear in nature. If the calculated EVM $> EVM_T$ (indicates nonlinear LED output), then the coefficients of the predistorter are re-estimated. This process is repeated until we get the linearzied output signal. This algorithm checks any variation in the linearization of the transmitted signal in regular intervals. If there is any change in the physical characteristics of LED or LED gets replaced by another LED, then ALA-based predistortion algorithm adapts to these changes in the transmitted signal and re-estimates the coefficients of predistorter.

The second step of the algorithm is coefficient estimation. This block minimizes the error between the predistorter output signal $v(n)$ and the predistorter input signal $y(n)$. A nonlinear

polynomial model is considered for the predistorter which can be expressed as [59]:

$$\hat{v}(n) = \sum_{p=0}^{P-1} \hat{c}_p x^{p+1}(n), \tag{2.18}$$

where $\hat{c}_p$ are the coefficients and $P$ is the nonlinearity order. Initially, the coefficient $(\hat{c}_0)$ is set to unity and the remaining coefficients $(\hat{c}_1, \hat{c}_2, \cdots, \hat{c}_P)$ are set to zero. Later, the values of these coefficients would be updated depending upon the nonlinear characteristics of LED. Their values are estimated using the ALA-based predistortion. For a total number of samples equal to $N$, we can rewrite (2.18) as (2.19) and (2.20) where $\mathbf{v}$ is a $N \times 1$ output vector, $\mathbf{Y}$ is a $N \times P$ input matrix and $\mathbf{c}$ is a $P \times 1$ coefficient vector. Since, it is an over-determined system, therefore it has no solution.

$$\begin{bmatrix} v(0) \\ v(1) \\ \vdots \\ v(N-1) \end{bmatrix} = \begin{bmatrix} y(0) & y^2(0) & \cdots & y^P(0) \\ y(1) & y^2(1) & \cdots & y^P(1) \\ \vdots & \vdots & \ddots & \vdots \\ y(N-1) & y^2(N-1) & \cdots & y^P(N-1) \end{bmatrix} \begin{bmatrix} c_0 \\ c_1 \\ \vdots \\ c_{P-1} \end{bmatrix} \tag{2.19}$$

$$\mathbf{v} = \mathbf{Y}\mathbf{c} \tag{2.20}$$

However, the coefficient vector $\mathbf{c}$ can be calculated by using least square (LS) solution on (2.20), which can be expressed as:

$$\hat{\mathbf{c}} = \arg\min_{\mathbf{c}} \|\mathbf{v} - \mathbf{Y}\mathbf{c}\|^2 \tag{2.21}$$

**Algorithm 1** ALA-based algorithm

**Input**: A DCO-OFDM signal $x(n)$
**Initialization**: $\hat{c}_0 \leftarrow 1$; $\hat{c}_1, \hat{c}_2, \cdots, \hat{c}_P \leftarrow 0$
1: Calculate ALA-based predistorter output $\hat{v}(n)$ using (2.18)
2: Calculate LED output $y(n)$ using (2.15) and OEC
3: Calculate $EVM$ using (2.17)
4: **while** $EVM > EVM_T$ **do**
5: Compute the values of coefficient $c_p$ using (2.22)
6: $\hat{c}_p \leftarrow c_p$ ;
7: **end while**
8: System is linearised

The solution of (2.21) can be given as:

$$\hat{\mathbf{c}} = (\mathbf{Y}^H\mathbf{Y})^{-1}\mathbf{Y}^H\mathbf{v}. \tag{2.22}$$

These estimated coefficients are used as the predistorter coefficients to predistort the input signal and then get the linearized output signal from the LED. The above steps for the proposed ALA-based algorithm has been summarized in Algorithm 1.

#### 2.5.2.1 Simulation Results and Discussion

The VLC channel and simulation parameters are given in Table 2.1 [5] and 2.2 [6, 7]. The performance of the proposed ALA-predistorter is compared against both linear VLC system and nonlinear VLC system.

Table 2.1: Optical channel parameters [5]

| **Channel Parameter** | **Value** |
|---|---|
| Lambertian mode number, $m$ | 45 |
| Area of PD, $A_{\text{PD}}$ | 9.8 $mm^2$ |
| PD's field of View, $\Psi_c$ | 60° |
| Transmitter location $(x_t,y_t,z_t)$ | (2.5 m, 2.5 m, 3m) |
| Receiver location, $(x_r,y_r,z_r)$ | (2.5 m, 2.5 m, 1m ) |
| Optical concentrator gain, $g_{\text{c}}$ | 0 dB |
| Optical filter gain, $g_{\text{f}}$ | 0 dB |
| Responsivity of PD, $R_{\text{PD}}$ | 0.53 A/W |

Table 2.2: System parameters [6, 7]

| **System Parameter** | **Value** |
|---|---|
| Room dimension | $5 \times 5 \times 3$ $\text{m}^3$ |
| Modulation | 16 QAM DCO-OFDM |
| DCO-OFDM IFFT order | 512 |
| Reflection coefficient, $\rho$ | 0.8 |
| Nonlinearity coefficient, $\zeta_{NL}$ | 0.541, 0.582, 0.65. |
| Predistorter nonlinearity order, $P$ | 7 |

The amplitude-amplitude (AM/AM) distortions due to nonlinear LED on the DCO-OFDM signal with different $\zeta_{NL}$ are shown in Fig. 2.8. It can easily be observed from Fig. 2.8 that with the increase in $\zeta_{NL}$, the gap between the linear model and LED model also increases. Thereby, degrading the quality of transmit signal degrades and consequently affecting the overall performance of the VLC system. With the help of the predistorter, the AM/AM curves approach the linear system which improves the system performance. From Fig. 2.8, it can

be clearly observed that the proposed ALA-based predistorter is capable of mitigating the nonlinearity caused by different LEDs.

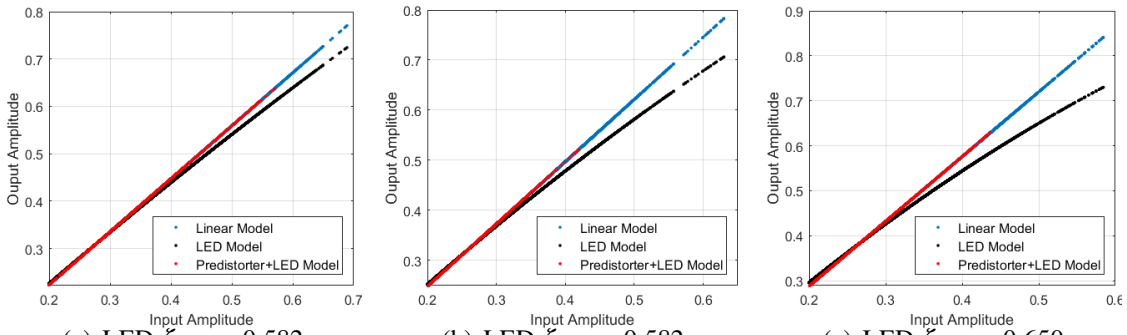


(a) LED $\zeta_{NL1} = 0.582$ (b) LED $\zeta_{NL2} = 0.582$ (c) LED $\zeta_{NL3} = 0.650$

Figure 2.8: AM/AM plot for nonlinear LED having different $\zeta_{NL}$ with and without ALA based predistorter

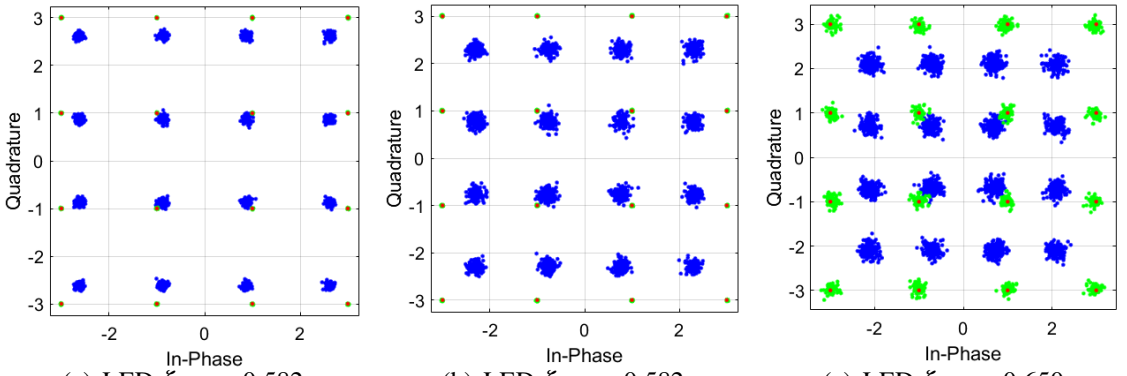


(a) LED $\zeta_{NL1} = 0.582$ (b) LED $\zeta_{NL2} = 0.582$ (c) LED $\zeta_{NL3} = 0.650$

Figure 2.9: Constellation plot for 16-QAM DCO-OFDM signal when pass through nonlinear LED having different $\zeta_{NL}$ with and without predistorter where red, blue, green and dots represents Input symbols, output symbols without predistorter, output symbols with ALA based predistorter, respectively.

The constellation diagram of input symbols and output symbols of nonlinear LEDs with and without predistorter for 16-QAM DCO-OFDM signal is shown in Fig. 2.9. It can be observed that the output symbols without predistorter (blue dots) are deviated from their expected position (red dots) due to the LEDs nonlinearity and this deviation increases with an increase in nonlinear parameter $\zeta_{NL}$. This indicates that there exits an inherent error in the nonlinear which is a function of LED nonlinearity. However, in presence of predistorter, the output symbols (green dots) are reverted close to their desired positions (red dots) because the predistorter compensates for the inherent LED nonlinear distortion.

## 2.6 Summary

In this chapter, an overview of a typical VLC system was presented followed by details related to VLC channel model, modulation schemes, and impairments in VLC including LED non-linearity. In the second half of the chapter, we proposed an adaptive-learning-architecture based predistortion technique to mitigate the effect of LED non-linearity. While the existing literature compared the performance of their algorithm “with predistorter" and “without predistorter" in nonlinear VLC system only, we have compared the performance of our proposed ALA-based predistortion technique with a linear VLC system as well. Furthermore, It is validated from the results that our proposed ALA-based predistortion provides performance matching to the linear VLC system. The near-linear performance is verified by AM/AM, constellation plots for LEDs with different values of $\zeta_{NL}$. In this chapter, we have shown that the effect of LED non-linearity on a DCO-OFDM system can be mitigated by using ALA-based predistortion. In the next chapter, we propose a method to deal with the issue of O-OFDM high PAPR.

Chapter 3

# PAPR Reduction for O-OFDM

In order to further improve the VLC physical layer, double precoding O-OFDM is proposed in this chapter to reduce the PAPR of O-OFDM. In Section 3.1, brief introduction and major contributions related to above mentioned technique are presented followed by details related to the system model in Section 3.2. The mathematical expressions of PAPR, complexity and average spectral efficiency are derived in Section 3.3. The analytical and simulation results are presented in Section 3.4. Finally, Section 3.5 concludes the chapter.

## 3.1 Introduction

The O-OFDM is most widely adopted in VLC to support high data rates. However, it suffers from the major draw back of high PAPR. Since the time domain O-OFDM is generated by addition of multiple subcarriers with distinct frequencies, it is possible to have constructive addition of various subcarriers. This can result into a relatively higher instantaneous power than the average power, which results in high PAPR. This high PAPR can cause sever clipping distortion that can result into degradation of system performance. In addition, a high PAPR reduces the illumination to communication conversion efficiency and lifetime of the LED. Thus, various techniques have been investigated in the literature in order to reduce the high PAPR of O-OFDM. They can be broadly classified into the following categories:

1. Signal Distortion Techniques: These techniques reduce the PAPR by distorting the O-OFDM signal before its transmission. Some common signal distortion techniques include (i) clipping and filtering [60, 61] (ii) companding [62] (iii) peak windowing [63] and (iv) peak reduction carrier. The clipping and filtering method works on the principle that high signal peaks occur rarely; therefore, these peaks can be clipped, which introduces signal distortion. Companding techniques involve the application of nonlinear transformation on the OFDM signal in order to reduce the PAPR values. However, this nonlinearity

operation destroys the orthogonality of OFDM and results in degraded performance. These are simple to implement techniques, but they introduce clipping distortion, which results in SER degradation.

2. Multiple signalling and probabilistic techniques: These techniques generate multiple candidate signals that contain the same information, and the signal with the lowest PAPR is selected for transmission. Some common probabilistic techniques includes: (i) partial transmit sequences [64], (ii) selected-mapping [64], (iii) tone-reservation [65], and (iv) pilot-assisted [66] etc.. Most of these methods typically require side information along with the data, which reduces the useful data rate and increases the computational complexity.

3. Precoding: One of the simplest methods for PAPR reduction is precoding [67]. In [68], authors proposed a block coding technique for PAPR reduction in O-OFDM; however, this technique requires additional bandwidth and introduces complexity overhead. In [69], authors proposed a discrete Hartley transform (DHT)-spread technique PAPR reduction in a DHT-based ACO-OFDM system. In [70], authors have considered precoding based on Vandermonde like matrix to reduce the high PAPR of DCO-OFDM and ACO-OFDM. In [71], authors have considered precoding based on discrete Fourier transform (DFT), DHT, and Zadoff-Chu transforms, and concluded that DFT precoder performs better than other precoders. It is found that DFT precoded OFDM provides lower PAPR and better BER performance [72]. The benefit and feasibility of the DFT precoded OFDM modulation format for a Gbit/s VLC system are demonstrated in [73]. Meanwhile, in order to deal with the issue of substantial interference in DFT precoded OFDM, an optimized lighting layout was proposed in [74]. Further, it has also been shown in [75] that subcarrier waveform shaping in OFDM is a form of precoding scheme, where each OFDM block is linearly transformed by a shaping matrix before modulation and transmission. In literature, various pulse shaping filters like raised-cosine (RC), root-raised-cosine filter (RRC), Gaussian, and finite impulse response (FIR) Nyquist filters have been considered for low PAPR OFDM system [76–80]. In [81], authors have used partial response precoding based on Gaussian-minimum-shift-keying (GMSK) pulse for further PAPR reduction in DFT precoded OFDMA system.

   The concept of Hermitian symmetry (HS) is used in O-OFDM to obtain a real signal. However, in [82], authors have demonstrated that due to the application of HS, only half of the time-domain DFT-precoded-OFDM symbols exhibit the single carrier form in VLC systems, therefore resulting in less compelling PAPR reduction as compared to radio counterparts. The inherent reason for this degradation is the loss of half of the degrees of freedom for subcarrier mapping due to the essential conjugate constraint for

HS; this restricts the subcarrier mapping space to only half of the OFDM bandwidth after DFT operation, rather than the entire bandwidth as in RF systems. In [83], authors have implemented a HS free optical-single-carrier frequency-division multiple access (HSFO-SCFDMA) and illustrated that it performs better than other alternatives that utilises HS. Furthermore, in [84], authors have shown that implementation based on real and imaginary separation for DFT precoded layered ACO-OFDM provides better PAPR performance as compared to conventional the HS method.

### 3.1.1 Main Contributions

In this chapter, we propose a novel modulation technique based on GMSK pulse shaping and DFT-precoding to further reduce PAPR of the OFDM signal for the VLC system, without compromising the power efficiency of the system. Additionally, the concept of grouped precoding is also explored to reduce the computational complexity of the proposed scheme compared to conventional DFT precoding [20]. As two precoding operations are performed in this system, i.e., DFT precoding and GMSK pulse shaping; therefore, we have named the proposed scheme as double precoded O-OFDM: (DP-OOFDM). In order to make DP-OOFDM compatible with IM/DD the concept of real and imaginary separation and flip-OFDM have been implemented in this work instead of HS, as HS based DFT precoded O-OFDM does not provide the best PAPR reduction [82–84]. For pulse shaping, GMSK has been chosen because it provides constant envelope and high spectral efficiency [85]. Since the performance of flip-OFDM and ACO-OFDM is similar [86]. Therefore, the performance of the proposed DP-OOFDM has been evaluated against ACO-OFDM, based on PAPR, power saving, SER, spectral efficiency, and computational complexity. To the best of our knowledge, the grouped DFT precoded OFDM based on real and imaginary part separation in conjunction with GMSK based pulse shaping has not been analyzed for VLC system. The main contributions of this chapter are as follows:

1. The DP-OOFDM has been introduced which consist of grouped DFT precoded OFDM in conjunction with GMSK pulse shaping, this approach has resulted in lower PAPR and high spectral efficiency over earlier explored alternatives.

2. This work provides a comprehensive performance analysis of proposed DP-OOFDM in-terms of PAPR, power saving, SER, spectral efficiency and computational complexity against conventional DFT-precoded OOFDM and ACO-OFDM. For SER evaluation, a VLC channel with both LOS and NLOS components are considered.

3. The concept of grouped precoding is also explored for DP-OOFDM, in order to reduce the computational complexity of the proposed scheme compared to conventional DFT

precoding. Further, different kinds of sub-carrier mapping has been analyzed to study the effect on PAPR and SER.

4. Analytical expression for PAPR of the proposed system is derived and compared with simulation results.

## 3.2 System Model

The block diagram for the proposed DP-OOFDM scheme which implements IM/DD is shown in Fig.3.1. At the transmitter, symbol mapping block converts the input bits into one of several possible modulation formats like binary phase shift keying (BPSK), 4-level quadrature amplitude modulation (4-QAM) etc. The modulated symbols $x_n$, are grouped into blocks each containing $N$ symbols. The $N$-point DFT is applied on this block of $N$ symbols. In general, DFT is performed to transform the data from time domain to frequency domain. However, here $N$-point DFT is used as a precoder i.e., the block of $N$ symbols are pre-coded using the DFT matrix to obtain $X_k$, as follows [87]:

$$X_k = \frac{1}{\sqrt{N}} \sum_{i=1}^{N-1} x_n \exp^{\frac{-j2\pi ki}{N}}, 0 \leq k \leq N \tag{3.1}$$

Further, subcarrier mapping block maps each of the $N$-point DFT outputs to one of the $M(>N)$

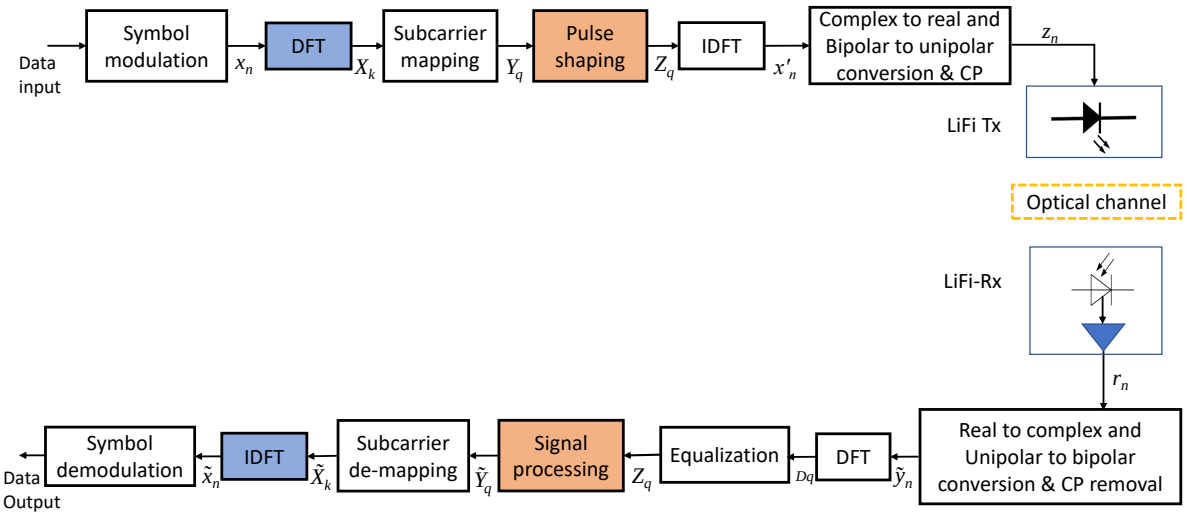


Figure 3.1: Block diagram of DP-OOFDM.

inputs of the inverse DFT (IDFT). There are two methods of subcarrier mapping; localized subcarrier mapping and distributed subcarrier mapping (described later). Factor of $L(=M/N)$

defines the bandwidth expansion factor. For a system transmitting $M$ symbols per block, $L$ simultaneous transmissions are possible. The output of the subcarrier mapping is multiplied with frequency response of signal shaping waveform to obtain $Y_q$. Subsequently, $M$-point IDFT transforms the subcarrier amplitudes to a complex time domain signal $x'_k$. For IM/DD data transmission over optical wireless channel, the signal needs to be real and positive. The complex to real and bipolar to unipolar block makes the complex output of IDFT compatible for IM/DD transmission. Afterwards, CP is added to $z_n$ and resultant signal is transmitted by the LED. At the receiver, photodetector converts received optical power into electrical signal. After channel equalization and CP removal, real to complex and unipolar to bipolar block converts the real unipolar signal $\tilde{z}_n$ into complex bipolar signal $\tilde{y}_n$. Further, $M$-point DFT is applied followed by subcarrier de-mapping and frequency domain processing to reverse the signal shaping applied at the transmitter. The resulting signal is then subjected to $N$-point IDFT and symbol demodulation to obtain the data output corresponding to the transmitted input data. The following subsections discuss different subblocks of the system model.

### 3.2.1 Subcarrier Mapping

Subcarrier mapping is achieved by implementing either the localized or distributed subcarrier mode. In localized mode, consecutive subcarriers are occupied by the DFT outputs of the input data whereas in the distributed mode, DFT outputs of the input data are allocated over the entire bandwidth with zeros occupying the unused subcarriers [88]. Interleaved subcarrier mapping is a special case of distributed subcarrier mapping when $M = L \times N$, therefore, equidistance subcarriers are occupied by DFT outputs of the input data [89]. The output of localized subcarrier mapping can be expressed as [87]:

$$Y_q = \begin{cases} X_q & : \ q = 0, 1, ..., N-1 \\ 0 & : \ \text{otherwise} \end{cases} \tag{3.2}$$

Similarly, the output for interleaved subcarrier mapping can be expressed as [87]:

$$Y_q = \begin{cases} X_{(q/L)} & : \ q = pL, \ \ p = 0, 1, ..., N-1 \\ 0 & : \ \text{otherwise} \end{cases} \tag{3.3}$$

An example of localized and interleaved subcarrier mappings in the frequency domain for $M = 12$, $N = 4$, and $Q = 3$ is illustrated in Fig. 3.2. Based on subcarrier mapping, the time domain output of IDFT differs i.e., samples equally spaced in frequency domain will result into periodic sequence in time domain and any shift in frequency domain will result into a phase rotation in time domain. Therefore, time domain output of IDFT for localized mode have exact

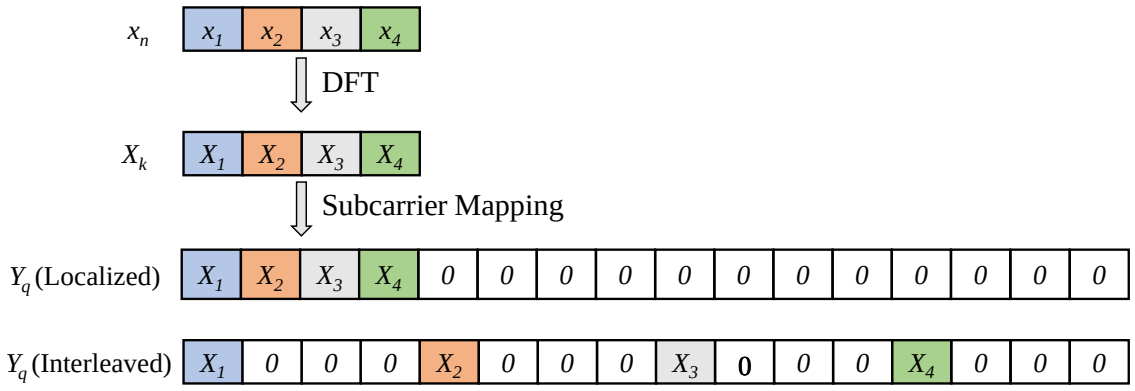


Figure 3.2: Subcarrier mapping in frequency domain

copies of input time symbols at the $M$-multiple sample positions and the in-between values are complex weighted sum of all the time input symbols in the input block. Time domain output of IDFT for interleaved mode is simply a repetition of the original input symbols with a scaling factor(1/Q). The time domain outputs of localized and interleaved mode are shown in Fig. 3.3. In this work, we have analyzed the proposed system for both interleaved and localized subcarrier mapping.

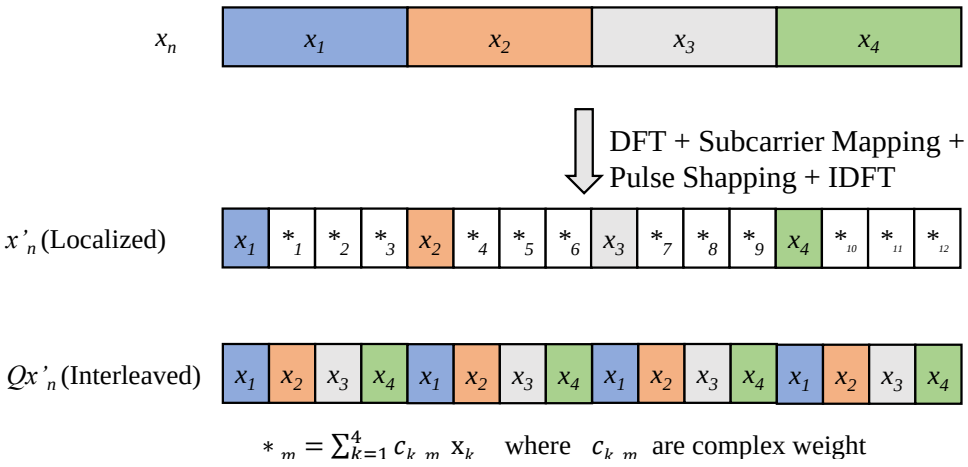


Figure 3.3: Time domain signal for different subcarrier mapping

### 3.2.2 Pulse Shaping

For a single carrier system, pulse shaping is required to band limit the transmitted signal. However, there is a trade-off between PAPR reduction and bandwidth efficiency in a single carrier system, i.e., pulse shaping limits the signal bandwidth at the cost of increased PAPR of

the transmitted signals. In order to reduce the PAPR of the single carrier system, we need a pulse with a reduced tail size because the magnitudes of the filter's sidelobes directly affect the PAPR. Few studies have been carried out to design a pulse shaping filter that limits the signal bandwidth without degrading the PAPR performance [77, 78, 90]. In this work, we have used GMSK filter for pulse shaping. GMSK pulse provides a constant envelope over the used bandwidth, and therefore improves the system performance. GMSK pulses are spectrally efficient and have reduced side lobe gain. Because of the aforementioned reasons, GMSK pulse has been chosen for pulse shaping in our proposed system. Further, for the sake of comparison with the conventional DFT precoded OFDM, we have considered rectangular pulse shaping filer as well which has been referred as DFT precoded OFDM in this work. We have performed pulse shaping in frequency domain i.e.,

$$\mathbf{Z} = \mathbf{YS} \tag{3.4}$$

where $\mathbf{S}$ is the frequency response of the pulse shaping filter $g(t)$. The time domain pulse shaping filter $g(t)$ is defined as follows [81]:

$$g(t)_{GMSK} = \frac{1}{T}[Q(\gamma(\frac{t}{T} - \frac{1}{2})) - Q(\gamma(\frac{t}{T} + \frac{1}{2}))] \tag{3.5}$$

where $\gamma \approx \frac{2\pi BT}{\sqrt{ln(2)}}$, BT is the bandwidth time product, that controls the pulse shape, and $Q(x) \approx \frac{1}{2\pi}\int_x^\infty \exp(\frac{-u^2}{2})du$

$$g(t)_{Rect} = rect(\frac{t}{T}) = \begin{cases} 1 & \frac{-T}{2} < t < \frac{T}{2} \\ 0 & otherwise \end{cases} \tag{3.6}$$

### 3.2.3 Complex to Real and Bipolar to Unipolar Conversion

In order to transmit data using LED, the signal needs to be real and positive. To meet this requirement, the real and imaginary part of the complex valued signal $\mathbf{x}'$ is separated and transmitted in different sub-frames. First sub-frame contains the real part of $\mathbf{x}$ i.e., $Re(\mathbf{x}')$ whereas, the second sub-frame contains the imaginary part i.e., $Imag(\mathbf{x}')$. After time multiplexing, the resultant vector $\mathbf{y}$ is represented as follows [87]:

$$y_n = \begin{cases} Re(x'_n) & : \ 0 \leq n \leq M \\ Imag(x'_n) & : \ M \leq n \leq 2M \end{cases} \tag{3.7}$$

The resultant bipolar signal $y_n$ can be written as [87]:

$$y_n = y_n^+ - y_n^- \tag{3.8}$$

where, $y_n^+$ and $y_n^-$ are the positive and negative parts of $y_n$ respectively. Therefore uniploar $z_n$ can be obtained as follows [87]:

$$y_n^+ = \begin{cases} y_n & : \ y_n \geq 0 \\ 0 & : \ \text{otherwise} \end{cases} \qquad y_n^- = \begin{cases} |y_n| & : \ y_n \leq 0 \\ 0 & : \ \text{otherwise} \end{cases} \tag{3.9}$$

$$z_n = \begin{cases} y_n^+ & : \ 0 \leq n \leq 2M \\ y_{n-2M}^- & : \ 2M \leq n \leq 4M \end{cases} \tag{3.10}$$

All the samples of the resultant signal $z_n$ are unipolar which are transmitted through LED, as shown in Fig. 3.4.

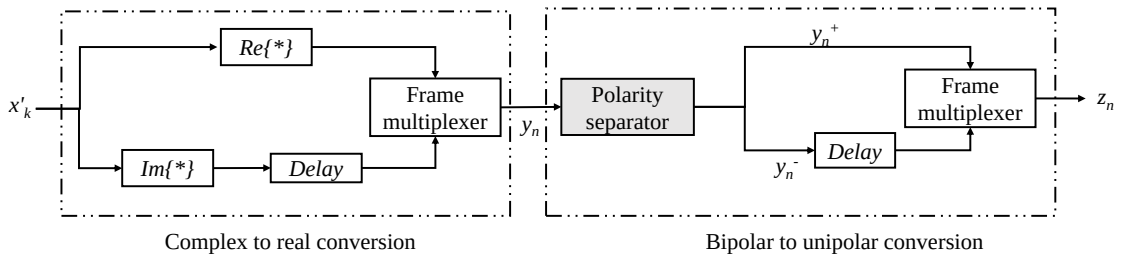


Figure 3.4: Complex to real and bipolar to unipolar conversion

### 3.2.4 Grouped DFT Precoding

The DFT precoding block adds extra computational complexity to the proposed system as compared to conventional optical OFDM system. One way to reduce this computational complexity is by using the concept of grouped precoding, where instead of performing $N$-point DFT, two $N/2$-point DFTs are applied. The $N$-block of data is divided into two $N/2$-blocks, each of which is processed by one of the two $N/2$-point DFTs. In this work, we have analyzed the proposed system using both, simple ($N$-point) DFT precoding and grouped (two $N/2$-point) DFT precoding which are referred as DP-OOFDM and G-DP-OOFDM respectively.

### 3.2.5 Receiver

At the receiver, PD receives optical signal and converts it into equivalent current signal which is converted into corresponding voltage signal by the transimpedance amplifier. Afterwards, CP is removed and channel equalization is performed by a zero-forcing equalizer in order to

compensate for distortion caused in transmitted signal due to the channel, resulting into signal $r_n$, which can be expressed as follows [87]:

$$r_n = z_n + w_n \qquad 0 \leq n \leq 4M \tag{3.11}$$

The bipolar signal $\tilde{z}_n$ is regenerated from $r_n$ as [87]:

$$\tilde{z}_n = r_n - r_{n+2M} \qquad 0 \leq n \leq 2M \tag{3.12}$$

Further, the real signal $z_n$ can be converted into complex signal as follows [87]:

$$\tilde{y}_n = \tilde{z}_n + j * \tilde{z}_{n+M} \qquad 0 \leq n \leq M \tag{3.13}$$

Further, $M$-point DFT is applied to $\tilde{y}_n$, to obtain frequency domain transform $\tilde{Z}_k$.

$$\tilde{Z}_k = \frac{1}{\sqrt{M}} \sum_{i=1}^{M-1} \tilde{y}_n \exp^{\frac{-j2\pi ki}{M}}, 0 \leq k \leq M \tag{3.14}$$

Afterwards, signal processing block and subcarrier demapping performs reverse operation of pulse shaping and subcarrier mapping respectively. The signal processing block performs following operation [87]:

$$\tilde{\mathbf{Y}} = \tilde{\mathbf{Z}} / \mathbf{S} \tag{3.15}$$

The subcarrier demapping for localized mode can be expressed as [87]:

$$\tilde{X}_n = \tilde{Y}_n \qquad n = 0, 1, ..., N-1 \tag{3.16}$$

For interleaved mode subcarrier demapping can be obtained by [87]:

$$\tilde{X}_n = \tilde{Y}_{nL} \qquad n = 0, 1, ..., N-1 \tag{3.17}$$

Further, $N$-point IDFT is applied to convert the signal back into time domain, which is expressed as [87]:

$$\tilde{x}_n = \frac{1}{\sqrt{N}} \sum_{i=1}^{N-1} \tilde{y}_n \exp^{\frac{j2\pi ki}{N}}, 0 \leq k \leq N \tag{3.18}$$

Finally, symbol demodulation is applied in-order to obtain data output corresponding to data input.

## 3.3 Performance Analysis and Comparison

This section provides mathematical analysis and comparison of the DP-OOFDM with ACO-OFDM on the basis of PAPR, computational complexity and spectral efficiency.

### 3.3.1 PAPR Analysis

The PAPR is defined as the ratio between the maximum peak power and the average power of the transmitted signal. PAPR of a transmitted signal $z_n$ can be defined as [87]:

$$PAPR_z = \frac{\max\limits_{0\leq n\leq 4M-1} z_n^2}{E[z_n^2]} \tag{3.19}$$

where $E[\cdot]$ denotes the expectation operation. A high PAPR signal requires LEDs with large dynamic range in order to avoid clipping distortion. Additionally, high PAPR reduces illumination to communication conversion efficiency and lifetime of the LED. The probability of PAPR of block greater than the threshold value ($\zeta$) is defined by complementary cumulative distribution function (CCDF) . CCDF of PAPR is commonly used to measure the performance of PAPR reduction techniques. The PAPR of ACO-OFDM can be expressed as [91]:

$$\begin{aligned}\Gamma_{ACO-OFDM} &= \text{Prob}(PAPR > \zeta) \\ &= \begin{cases} 1-[2\phi(\sqrt{c(0,u)\zeta}-1)]^{\frac{M}{2}}, & 0\leq\zeta\leq\theta_{0,U} \\ 0, & \zeta\geq\theta_{0,U} \end{cases}\end{aligned} \tag{3.20}$$

where $\theta_{0,U} = u^2/c(0,u)$ and $u$ is the normalized upper clipping bound which is set to 1, for the sake of simplicity. The other required values are defined below.

$$c(0,u) = -\Phi(0) - (u^2-1)\Phi(u) + u^2 - ug(u), \tag{3.21}$$

$$g(x) = \frac{1}{\sqrt{(2\pi)}}\exp\frac{-x^2}{2}, \qquad \Phi(x) = \int_{-\infty}^{x}\frac{1}{\sqrt{2\pi}}\exp\frac{-t^2}{2}dt \tag{3.22}$$

In order to make DFT precoded OFDM compatible with VLC, we have implemented real and imaginary separation and concept of flip OFDM in order to obtain unipolar signals. It is important to note that the distribution of PAPR will depend upon the instantaneous power and average power. As real and imaginary separation followed by positive and negative separation is implemented, therefore, the relationship between average signal power of $x_n'$ and $z_n$ can be obtained as [87]:

$$E[|x_n'|^2] = 4E[|z_n|^2] \tag{3.23}$$

The CCDF of PAPR for DP-OOFDM can be obtained by [87]:

$$\begin{aligned}\Gamma_{DP-OOFDM} &= \text{Prob}(PAPR_z > \zeta) \\ &= 1 - (\text{Prob}(PAPR_z < \zeta)) \\ &= 1 - \text{Prob}\left(\frac{\max\limits_{0\le n\le 4M-1}|z_n|^2}{E[|z_n|^2]} < \zeta\right) \end{aligned} \tag{3.24}$$

It is important to note that $z_n$ and $z_{n+2M}$ are correlated i.e. only one of them would be non-zero, however, the same is not true for $z_n$ and $z_{n+M}$, as they represent the real and imaginary part of $x'_n$ . Therefore, equation (3.24) can be rewritten as [87]:

$$\begin{aligned}\Gamma_{DP-OOFDM} &= 1 - 2 \times \text{Prob}\left(\max_{0\le n\le 2M-1}|z_n|^2 < \zeta E[|z_n|^2]\right) \\ &= 1 - 2 \times \prod_{n=0}^{2M-1} \text{Prob}\left({x'_n}^2 < \frac{\zeta E[(x'_n)^2]}{4}\right) \\ &= 1 - 2 \times \text{Prob}\left({x'_n}^2 < \frac{\zeta E[(x'_n)^2]}{4}\right)^{2M} \end{aligned} \tag{3.25}$$

It may be noted that for localized and interleaved sub-carrier mapping the distribution of instantaneous power of $x'_n$ remains the same [92]. The CDF of instantaneous power of $x'_n$ at a given time instant $n$ can be expressed as [93]:

$$\text{Prob}({x'_n}^2 < \xi) = \sqrt{\xi}\int_0^{\infty} J_1(\sqrt{\xi}R)\, G(R,n)\, dR \tag{3.26}$$

where $J_n(\cdot)$ donates $n^{th}$ order first kind Bessel function and

$$G(R;n) \triangleq \frac{1}{2\pi}\int_0^{2\pi} \upsilon_{x,y}(R\cos(\phi), R\sin(\phi); n) d\phi \tag{3.27}$$

here, $\upsilon_{x,y}$ is the joint characteristic function of $Re(x'_n)$ and $Imag(x'_n)$. For $Q^2$-QAM, $G(R;n)$ is defined as follows [94]:

$$G(R;n) = \left(\frac{2}{Q}\right)^2 \sum_{m=0}^{\frac{Q}{2}-1}\sum_{l=0}^{\frac{Q}{2}-1} J_0\left(\alpha_n R\sqrt{A_m^2 + A_l^2}\right) \tag{3.28}$$

where $\alpha_n$ depends on the pulse shaping filter i.e., $\alpha_n = g(t+nT)$ and $A_m \triangleq (2m+1)\sqrt{\frac{3}{2(Q^2-1)}}$ : $m = \frac{-Q}{2}, ..., -1, 0, ..., \frac{Q}{2}$ and $A_l \triangleq (2l+1)\sqrt{\frac{3}{2(Q^2-1)}}$ : $l = \frac{-Q}{2}, ..., -1, 0, ..., \frac{Q}{2}$. The PAPR can be calculated by substituting values from equation (3.26) and (3.28) into (3.25).

### 3.3.2 Complexity

The computational complexity of $M$-point DFT algorithm is defined as $M^2$ complex multiplications and $(M^2 - M)$ complex additions [95]. In case of ACO-OFDM, there is only $M$-point IDFT, whereas in case of DP-OOFDM there is $N$-point DFT, $M$-point IDFT and frequency domain pulse shaping, therefore, increasing the complexity of DP-OOFDM. The G-DP-OOFDM is an attempt to reduce the complexity of DP-OOFDM by using two $N/2$-point DFTs for precoding instead of one $N$-point DFT precoding as used in DP-OOFDM. The computational complexities of transmitters for these schemes are given in Table 3.1. It can be seen that grouped DFT precoding scheme reduces the computational complexity of system as compared to conventional DFT precoding scheme.

Table 3.1: Computational complexity of transmitters

| Modulation scheme | No. of effective real multiplications |
|---|---|
| ACO-OFDM | $4M^2$ |
| DP-OOFDM | $4M^2 + 4N^2 + 4M^2 + M$ |
| G-DP-OOFDM | $4M^2 + \frac{4N^2}{2} + 4M^2 + M$ |

### 3.3.3 Spectral Efficiency

The spectral efficiency of OFDM and DFT precoded OFDM is a function of IDFT size ($M$) and modulation order ($Q$). If pulse shaping filter is not considered, then OFDM and DFT precoded OFDM will have same spectral efficiency given as [96]

$$\eta = Q\frac{M/4}{M+CP} \tag{3.29}$$

where, the factor of $1/4$ takes into account the loss of spectral efficiency for conversion of complex bipolar signal into real unipolar signal. However, in the DP-OOFDM system, we have considered a GMSK pulse shaping filter along with DFT precoded OFDM whereas conventional OFDM uses a rectangular pulse, i.e., sinc in frequency domain. By using the FVTool of MATLAB, the magnitude response of rectangular and GMSK filters are obtained

using the FVTool of MATLAB, as shown in Figs. 3.5. It is observed that the rectangular filter has higher sidelobes as compared to GMSK filter, therefore, making the proposed DP-OOFDM more spectrally efficient as compared to ACO-OFDM.

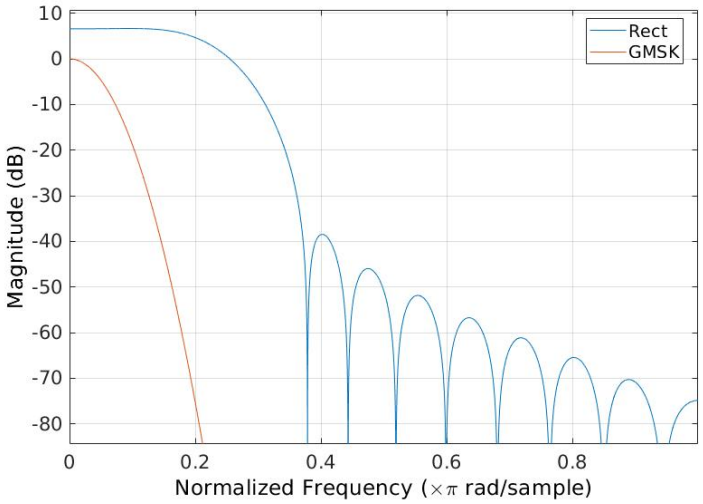


Figure 3.5: Magnitude response of Rectangular and GMSK pulse.

## 3.4 Simulation Results and Discussion

In this section, different variants of DP-OOFDM are compared with DFT precoded O-OFDM and ACO-OFDM, based on their PAPR, power saving and SER using MATLAB simulations. The variants of DP-OOFDM are DP-OOFDM with localized subcarrier maping (L-DP-OOFDM) , DP-OOFDM with interleaved subcarrier mapping (I-DP-OOFDM) , grouped DP-OOFDM with localized subcarrier mapping (G-L-DP-OOFDM) and grouped DP-OOFDM with interleaved subcarrier mapping (G-I-DP-OOFDM) . In this chapter, the focus is on the performance evaluation of the proposed scheme, therefore, for simplicity we have assumed irradiance and incident angels as 0. The channel and simulation parameters are given in Table 3.2 [5] and Table 3.3 respectively. The results are evaluated and presented in Table 3.4.

### 3.4.1 PAPR

By using extensive MATLAB simulation and equation (3.19), the CCDF of PAPR for proposed scheme was obtained. Further, using equations (3.26) and (3.28) into (3.25), the analytical PAPR for the proposed scheme was obtained and plotted in Fig.3.6.

Table 3.2: Optical channel parameters

| **Channel Parameter** | **Value** |
|---|---|
| Lambertian mode number, $m$ | 45 |
| Area of PD, $A_{\text{PD}}$ | 9.8 $mm^2$ |
| PD's field of View, $\Psi_c$ | 60° |
| Transmitter location $(x_t,y_t,z_t)$ | (2.5 m, 2.5 m, 3m) |
| Receiver location, $(x_r,y_r,z_r)$ | (2.5 m, 2.5 m, 1m ) |
| Optical concentrator gain, $g_{\text{c}}$ | 0 dB |
| Optical filter gain, $g_{\text{f}}$ | 0 dB |
| Responsivity of PD, $R_{\text{PD}}$ | 0.53 A/W |

Table 3.3: Simulation parameters

| Parameters | ACO-OFDM | DFT-precoded OFDM | DP-OOFDM | G-DP-OOFDM |
|---|---|---|---|---|
| Modulation | 4 QAM | 4 QAM | 4 QAM | 4 QAM |
| Order of IDFT | 64 | 64 | 64 | 64 |
| Pulse shaping filter | Rect. | Rect. | GMSK | GMSK |
| Bandwidth time product ($BT$) for pulse shaping filter | NA | NA | 0.5 | 0.5 |
| Precoding | NA | 32-point DFT | 32-point DFT | 2 blocks of 16-point grouped DFT |

Figs. 3.6(a) and 3.6(b) show the CCDF of PAPR for DP-OOFDM with localized and interleaved sub-carrier mapping respectively. For localized mapping, it is observed that the proposed L-DP-OFDM, performs better than the L-DFT precoded OOFDM and ACO-OFDM. For a clipping probability Prob($PAPR > \zeta$) $= 10^{-1}$, $PAPR$ gain of 2.5 and 5 dB is achieved in L-DP-OOFDM over L-DFT precoded OOFDM, and ACO-OFDM respectively. Similarly, for interleaved sub-carrier mapping, proposed I-DP-OFDM have superior PAPR performance as compared to I-DFT precoded OOFDM and ACO-OFDM, as shown in Fig. 3.6(b). $PAPR$ gain of 1.9 and 10.6 dB is achieved by I-DP-OOFDM over I-DFT-precoded OOFDM and ACO-OFDM, if the clipping probability Prob($PAPR > \zeta$) is set to $10^{-1}$. Additionally, the theoretical PAPR derived in section 3.3.1 have been plotted in Fig.3.6, and they show a close overlap with the simulation results.

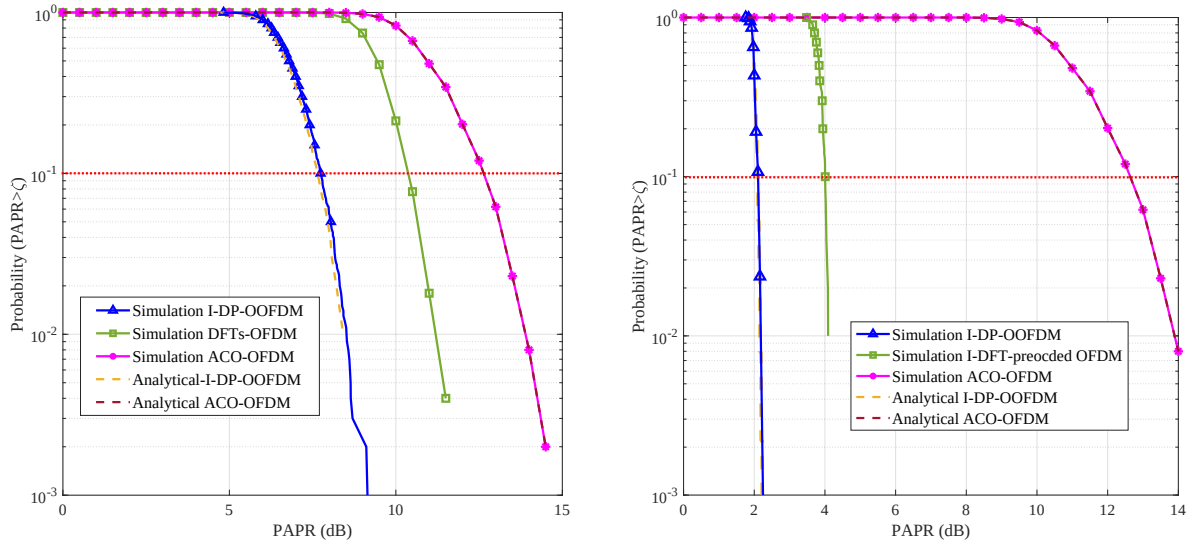


(a) Localized subcarrier mapping (b) Interleaved subcarrier mapping

Figure 3.6: CCDF distribution of PAPR (dB) for ACO-OFDM, DFT precoded OOFDM and DP-OFDM with different subcarrier mapping.

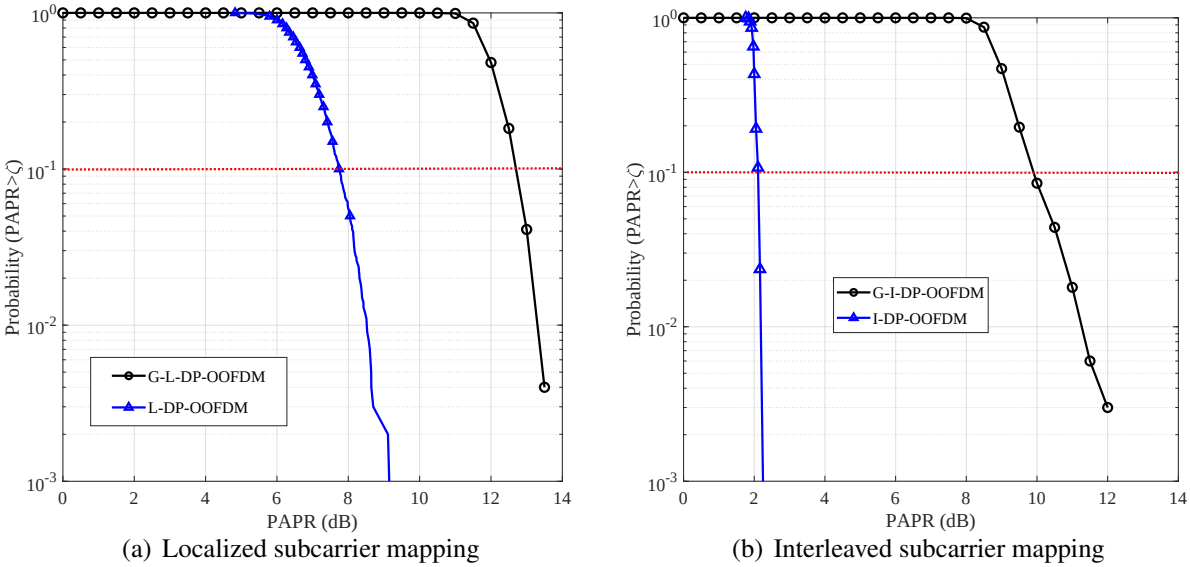


(a) Localized subcarrier mapping (b) Interleaved subcarrier mapping

Figure 3.7: Effect of grouped DFT precoding on CCDF distribution of PAPR (dB)

Fig. 3.7 illustrates the effect of grouped DFT precoding for the proposed DP-OOFDM in terms PAPR CCDF. It can be clearly seen that the PAPR for grouped configurations are higher as compared to the ungrouped configurations. In case of localized subcarrier mapping, for clipping probability Prob($PAPR > \zeta$) $= 10^{-1}$, the value of $PAPR$ is 5 and 12.5 dB in L-DP-OOFDM and G-L-DP-OOFDM respectively. Similarly, for interleaved subcarrier mapping, at clipping probability Prob($PAPR > \zeta$) $= 10^{-1}$, the value of $PAPR$ is 2.1 and 9.8 dB in I-DP-OOFDM and G-I-DP-OOFDM respectively.

Overall, I-DP-OOFDM provides lowest PAPR as compared to all the other schemes. The reason behind low PAPR of I-DP-OOFDM can be understood by Fig.3.3 which illustrates that the time domain output for interleaved mode is simply a repetition of the original input symbols with a scaling factor (1/Q). Because of this structure, interleaved mode output will have less fluctuation and lower peaks than localized mode output. Therefore, the interleaved mode is desirable than the localized mode in terms of PAPR.

### 3.4.2 Power Saving

The power saving ($P_{saving}$) achieved by the DP-OOFDM over the ACO-OFDM, is given by [87]:

$$P_{saving_{DP-OOFDM}} = 10\log_{10}\left(\frac{P_{ACO-OFDM}}{P_{DP-OOFDM}}\right) \tag{3.30}$$

where, $P_{ACO-OFDM}$ and $P_{DP-OOFDM}$ corresponds to the power required for the transmission of ACO-OFDM signal and different variants of DP-OOFDM respectively. The values of $P_{ACO-OFDM}$ and $P_{DP-OOFDM}$ can be calculated by using the following generic formula [97].

$$P = P_{avg} * \xi \tag{3.31}$$

where, $\xi$ is the inverse function of the CCDF for a given clipping probability i.e., Prob.($PAPR > \zeta_{\text{PAPR}}$) and $P_{avg}$ is the average power per time slot. In order to determine the power saving achieved by the DP-OOFDM over the ACO-OFDM using equation 3.30, the $P_{avg}$ for ACO-OFDM, L-DP-OOFDM, G-L-DP-OOFDM, I-DP-OOFDM and G-I-DP-OOFDM schemes has been obtained through extensive MATLAB simulations. Furthermore, the value of $\zeta_{\text{PAPR}}$ is calculated for clipping probability Prob.($PAPR > \zeta_{\text{PAPR}}$) set to $10^{-1}$ from the CCDF curve (Fig. 4.6 and 3.7). The power saving is found to be 8.19, 18.05, 13.83 and 19.19 dB over ACO-OFDM for L-DP-OFDM, G-L-DP-OFDM, I-DP-OFDM and G-I-DP-OFDM respectively. This saving of power over ACO-OFDM is because of the low $P_{avg}$ and reduced PAPR of the proposed schemes. It is important to note that grouped DFT precoding further reduces the $P_{avg}$, therefore, provides higher power saving.

Similarly, the power saving ($P_{saving}$) achieved by the DFT-precoded OOFDM over the ACO-OFDM, is given by [87]:

$$P_{saving_{DFT-precodedOOFDM}} = 10\log_{10}\left(\frac{P_{ACO-OFDM}}{P_{DFT-precoded\ OOFDM}}\right) \tag{3.32}$$

where, $P_{ACO-OFDM}$ and $P_{DFT-precodedOOFDM}$ corresponds to the power required for the transmission of ACO-OFDM signal and different variants of DFT-precoded OOFDM respectively. The values of $P_{ACO-OFDM}$ and $P_{DFT-precoded\ OOFDM}$ can be calculated by using (3.31). By following the same procedure, the power saving for L-DFT-precoded OOFDM and I-DFT-precoded OOFDM over ACO-OFDM is found to be 3.98 and 8.04 dB respectively.

### 3.4.3 SER

By using extensive MATLAB simulation, the SER for the proposed techniques was obtained. The SER performance for localized subcarrier mapping (L-DP-OOFDM and L-DFT-precoded OFDM) is shown in Fig. 3.8(a).

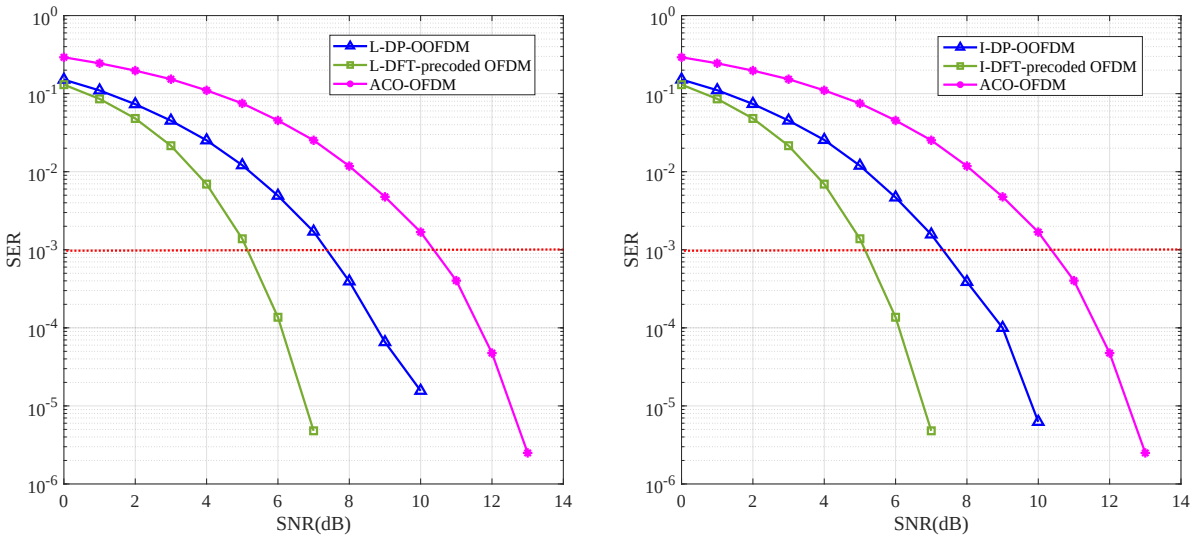


(a) Localized subcarrier mapping (b) Interleaved subcarrier mapping

Figure 3.8: SER Performance for ACO-OFDM, DFT precoded OOFDM and DP-OFDM with different subcarrier mapping.

It is observed that L-DP-OOFDM have better SER performance compared to ACO-OFDM, and L-DFT precoded OFDM performs better than L-DP-OOFDM, in terms of SER. For FEC limit i.e., $SER$ of $10^{-3}$, L-DP-OOFDM provides SNR gain of 2.9 dB over ACO-OFDM,

whereas L-DFT-precoded OFDM provides SNR gain of 2.3 dB over L-DP-OOFDM. Similar trend is observed for Interleaved subcarrier mapping (I-DP-OOFDM and I-DFT-precoded OOFDM) as shown in Fig. 3.8(b). It is observed that for FEC limit, I-DP-OOFDM and I-DFT-precoded OOFDM provides SNR gain of 2.9 and 5.2 dB over ACO-OFDM respectively. The effect of grouped DFT precoding on SER performance is shown in Fig. 3.9. In case of localized subcarrier mapping, for FEC limit, G-L-DP-OOFDM provides a SNR gain of 6.1 dB over ACO-OFDM. Similar performance gain is observed for interleaved subcarrier mapping. From the observations, it can be concluded that grouping not only reduces the computational complexity but also improves the SER performance. Further, the SER performance is independent of the subcarrier mapping.

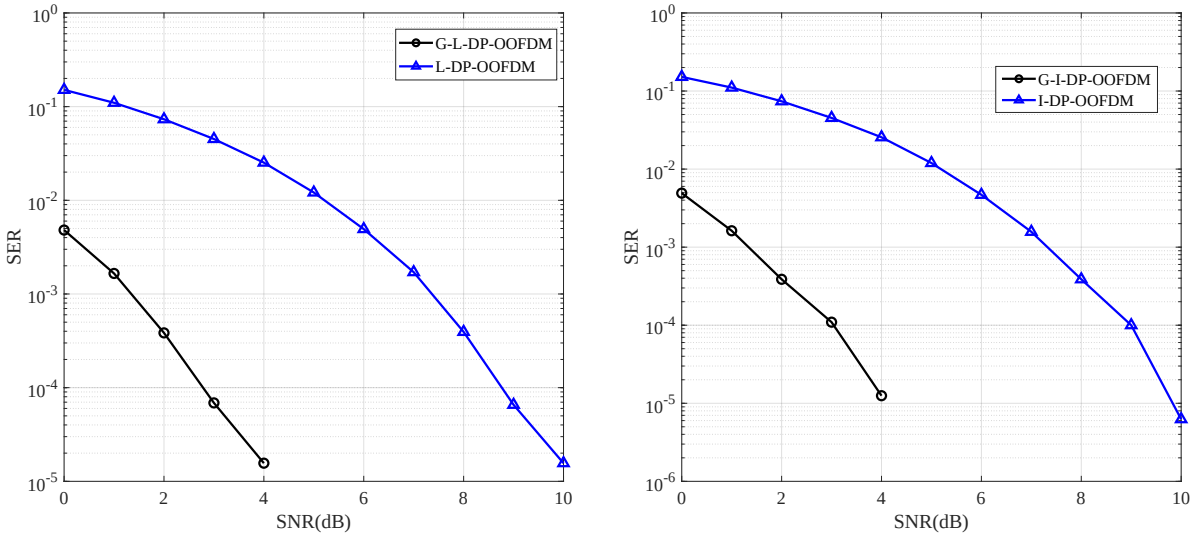


(a) Localized subcarrier mapping (b) Interleaved subcarrier mapping

Figure 3.9: Effect of grouped DFT precoding on SER Performance.

## 3.5 Summary

In this chapter, we have proposed and evaluated the DP-OOFDM scheme based on complexity, spectral efficiency, PAPR, power-saving and SER against conventional DFT-precoded OOFDM and ACO-OFDM. A comprehensive summary of the results is presented in Table 3.4. It is observed from the results that there is a trade-off between PAPR and SER if the interleaved subcarrier mapping is used. It must also be noted that, although grouped DFT precoding reduced the computational complexity at the cost of PAPR performance, but it still provided better power saving. Further, DP-OOFDM schemes are low PAPR and spectrally efficient as

Table 3.4: Summary of results

| Parameters | ACO-OFDM | L-DFT-precoded OOFDM | L-DP-OOFDM | G-L-DP-OOFDM | I-DFT-precoded OOFDM | I-DP-OOFDM | G-I-DP-OOFDM |
|---|---|---|---|---|---|---|---|
| Value of PAPR ($\zeta$) for CCDF prob. $= 10^{-1}$ | 12.7 | 10.2 | 7.7 | 12.75 | 4.0 | 2.1 | 9.8 |
| Power saving (dB) with respect to ACO-OFDM | – | 3.98 | 8.19 | 18.05 | 8.04 | 13.84 | 19.19 |
| SNR (dB) for FEC limit ($10^{-3}$) | 10.3 | 5.1 | 7.4 | 1.4 | 5.1 | 7.4 | 1.4 |

compared to DFT-precoded OFDM and ACO-OFDM. It can be concluded that I-DP-OOFDM outperformed all the schemes under consideration from PAPR perspective and G-I-DP-OOFM was desirable from SER and power-saving points of view. Therefore, one can choose either G-L-DP-OOFDM or G-I-DP-OOFDM for high reliability and power saving, however, I-DP-OOFDM is the most appropriate scheme for low PAPR. These results are useful in selecting appropriate schemes for different VLC applications.

Chapter 4

# Advanced Modulation Scheme for VLC: O-GFDM

This chapter presents an advanced more flexible modulation schemes for next generation VLC: optical-generalized frequency division multiplexing (O-GFDM). The brief introduction and contributions related to above mentioned system are given in Section 4.1, followed by Section 4.2 which presents the system model. Section 4.3 provides the derivation of spectral efficiency, SER, and complexity for this advanced modulation scheme. The simulation results are presented in Section 4.4. Finally, Section 4.5 summarizes the chapter.

## 4.1 Introduction

Generalized frequency division multiplexing (GFDM) is one of the potential candidate for next-generation wireless communications, as it is based on block structure of $NJ$ samples, where each of the $N$ subcarriers carry $J$ subsymbols. Each subcarrier is filtered by a circularly shifted filter. The subcarrier filtering can result in non-orthogonal subcarriers, which in turn may give rise to both inter-symbol interference (ISI) and inter-carrier interference (ICI). However, efficient receiving techniques can eliminate this interference and can achieve SER performance matching to that of OFDM [98]. GFDM turns into OFDM when $J = 1$, and single carrier with single carrier frequency domain equalization (SC-FDE) when $N = 1$. Since, GFDM in general will have some value of $J$ and $N$, therefore, the PAPR of GFDM will range between OFDM and SC-FDE [99]. The PAPR of GFDM can be further controlled by adjusting the parameters of sub-carrier filters [100, 101]. In GFDM, a single CP is added for entire block that contains multiple subsymbols, resulting into improved spectral efficiency of the system. This improved spectral efficiency can be traded for an additional redundancy which leads to relaxation in synchronization requirements of multiple users in an MTC scenario. GFDM can also fulfill low

latency requirement for tactile internet and vehicle-to-vehicle (V2V) applications by ultizing its flexible block structure [21]. The flexible nature of GFDM makes it a suitable candidate for future communication applications. To the best of our knowledge, GFDM for VLC has not been analyzed in detail, however, a limited analysis was done by one of the authors of this work [102]. In this work, we propose optical generalized frequency division multiplexing (O-GFDM), i.e., GFDM for VLC, in order to make it suitable for future applications. Two variants of O-GFDM namely, with and without DC bias have been evaluated on the basis of PAPR, SER and subcarrier frequency shift tolerance.

### 4.1.1 Main Contributions

The main contributions of this chapter are as follows:

1. This work propose two variants of GFDM for VLC namely, O-GFDM with DC (OGFDM-DC) and without DC bias (OGFDM-NDC). These schemes have been evaluated against their O-OFDM counterpart.

2. This work provides a comprehensive performance analysis of proposed O-GFDM schemes in-terms of spectral efficiency, complexity, power saving, PAPR, SER, and subcarrier frequency shift tolerance against conventional DCO-OFDM and ACO-OFDM schemes.

3. Further, analytical SER expressions of O-GFDM was derived and results are validated through simulations.

## 4.2 System Model

The transceiver structure for DC biased O-GFDM (OGFDM-DC) and Non-DC biased O-GFDM (OGFDM-NDC) are discussed in sections 4.2.1 and 4.2.2 respectively.

### 4.2.1 DC-biased O-GFDM

The details of DC biased O-GFDM (OGFDM-DC) transmitter and receiver are as follows:

#### 4.2.1.1 Transmitter

The block diagram of OGFDM-DC transmitter is shown in Fig. 4.1. The input data bits are converted into $NJ$ data streams where, $N$ is the total number of subcarriers and $J$ is the total number of time slots. These $NJ$ data streams are sent to $NJ$ independent M-QAM mappers

and each modulated data symbol is represented as $s_{n,j}$, where, $n \in \{0,1,2,...,N-1\}$ and $j \in \{0,1,2,...,J-1\}$. Afterwards, each data symbol $s_{n,j}$ is upsampled by $(JK-1)$ zero-padding, where, $K$ represents the number of samples in a time-slot. This sequence is fed to a transmit filter with impulse response $p(k)$ of length $L = JK$ and circular convolution is performed. The transmit filter can have non-rectangular shape which can be either raised cosine (RC) or root raised cosine (RRC) [103, 104]. After performing circular convolution, each sub-stream is up-converted by a complex subcarrier $c_n(k)$. The resultant complex valued O-GFDM symbol can be written as

$$x(k) = \sum_{j=0}^{J-1} \sum_{n=0}^{N-1} s_{n,j}(k) \odot p(< k - jK >_{JK-1}) c_n(k) \tag{4.1}$$

where, $< \cdot >_Z$ denotes the $Z$-modulo operator and $\odot$ denotes the circular convolution and the matrix form of (4.1) can be represented as:

$$\mathbf{X} = diag(\mathbf{CSP}) \tag{4.2}$$

where, diag $(\cdot)$ returns the main diagonal of a matrix, $\mathbf{C}$ is the matrix containing $N$ complex subcarriers and $\mathbf{P}$ is the matrix which contains the circularly shifted version of $p(k)$.

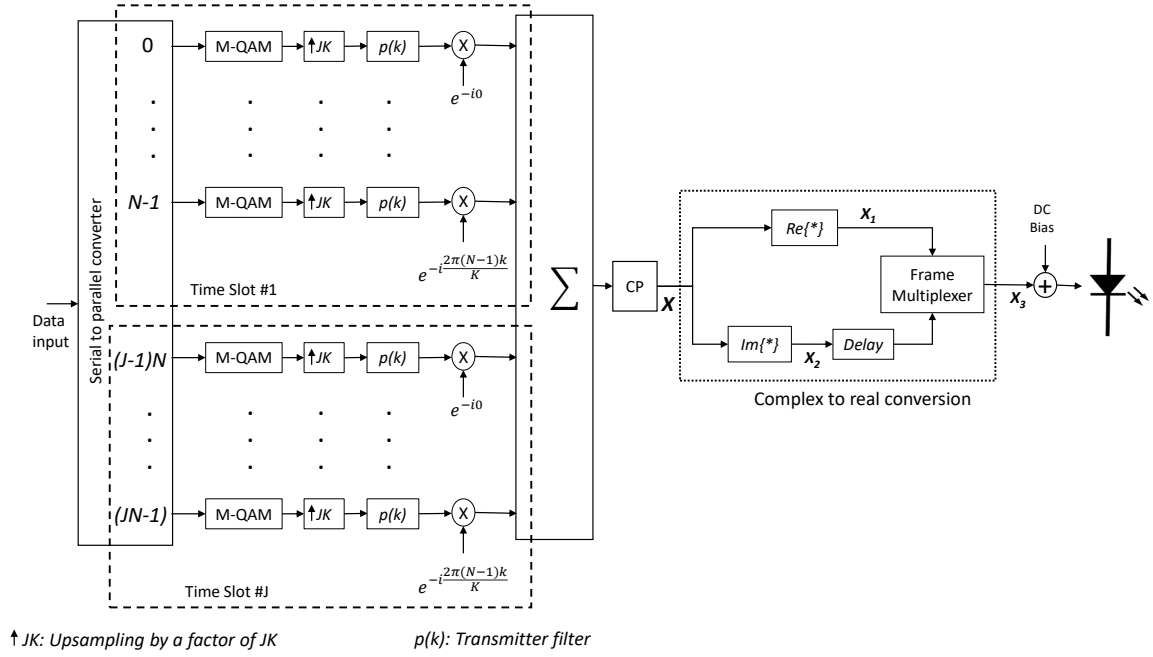


Figure 4.1: Block diagram of OGFDM-DC transmitter.

Further, it is important to note that resultant GFDM signal is complex and this signal needs to be converted into real and positive for IM/DD data transmission over optical wireless

channel. To meet this requirement, the real and imaginary part of the complex-valued signal $\mathbf{X}$ is separated and transmitted in different sub-frames. First sub-frame $\mathbf{X_1}$ contains the real part of $\mathbf{X}$ i.e., Re($\mathbf{X}$) whereas, the second sub-frame $\mathbf{X_2}$ contains the imaginary part i.e., Im($\mathbf{X}$). After multiplexing $\mathbf{X_1}$ and $\mathbf{X_2}$, the resultant vector $\mathbf{X_3}$ is obtained as follows: The resultant signal $\mathbf{X_3}$ is transmitted through LED after adding appropriate DC bias.

#### 4.2.1.2 Receiver

The block diagram of the OGFDM-DC receiver is shown in Fig. 4.2. The received optical signal is first converted into an electrical signal with the help of PD. After removal of DC bias, the resultant signal $\mathbf{Y_3}$ is further demultiplexed into $\mathbf{Y_1}$ and $\mathbf{Y_2}$, to get back the complex-valued signal $\mathbf{Y}$. After removal of CP, down conversion and convolution with receiver matched filter ($g(k)$), minimum means square error (MMSE) detector is used to estimate the transmitted data bits. MMSE detector is given as [105]:

$$\mathbf{Y_{MMSE}} = \left[\mathbf{A}^H\mathbf{A} + \left(\frac{1}{SNR}\right)\mathbf{I}_{NJ}{}^{-1}\mathbf{A}^H\right]\mathbf{Y_0} \tag{4.3}$$

where, $SNR$ is the signal to noise ratio of the channel and $I_{NJ}$ is the identity matrix of size $NJ$.

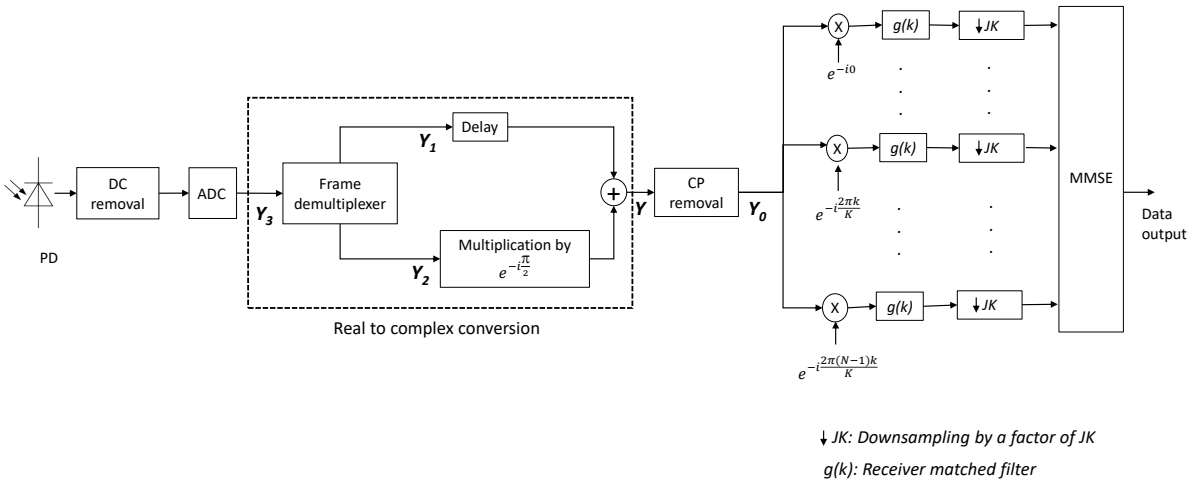


Figure 4.2: Block diagram of OGFDM-DC receiver.

### 4.2.2 Non-DC-biased O-GFDM

In this work, we analyze another transmission strategy using the concept of flip-OFDM [42], which does not require DC-biasing. The transmitter and receiver of non-DC biased O-GFDM (OGFDM-NDC) scheme are described below:

#### 4.2.2.1 Transmitter

The block diagram of the OGFDM-NDC transmitter is shown in Fig. 4.3. At the transmitter signal processing till the formation of the bipolar signal $\mathbf{X_3}$ is the same as that of OGFDM-DC. From (3.7), the bipolar signal $\mathbf{X_3}$ can be written as:

$$\mathbf{X_3} = \mathbf{X_3^+} - \mathbf{X_3^-} \tag{4.4}$$

where, $\mathbf{X_3^+}$ and $\mathbf{X_3^-}$ are the positive and negative parts of $\mathbf{X_3}$ respectively and are defined as:

$$\mathbf{X_3^+} = \begin{cases} x_3(k) & : \ x_3(k) \geq 0 \\ 0 & : \ \text{otherwise} \end{cases} \tag{4.5}$$

$$\mathbf{X_3^-} = \begin{cases} |x_3(k)| & : \ x_3(k) < 0 \\ 0 & : \ \text{otherwise} \end{cases} \tag{4.6}$$

where, $x_3(k)$ is the element of vector $\mathbf{X_3}$ and $k \in \{1, 2, ..., 2N\}$. Positive part $\mathbf{X_3^+}$ is transmitted in first O-GFDM sub-frame followed by the sub-frame containing $\mathbf{X_3^-}$ signal, by using frame multiplexing. All the samples of the resultant signal $\mathbf{X_4}$ are unipolar, thus can be transmitted through the optical wireless channel using LED.

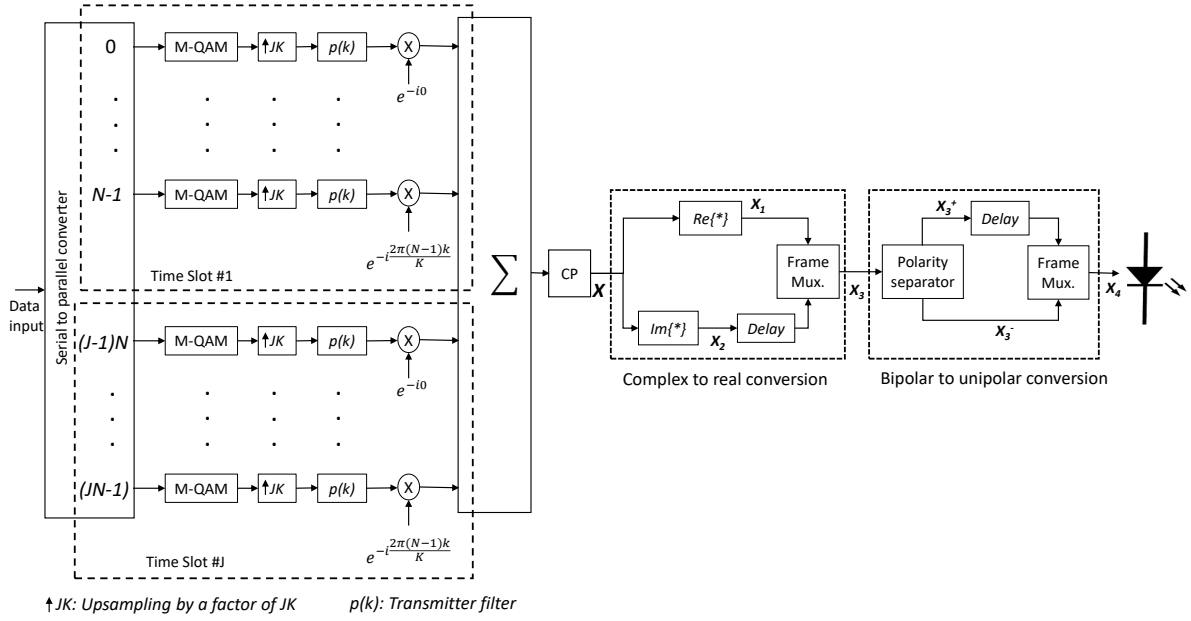


Figure 4.3: Block diagram of OGFDM-NDC transmitter.

#### 4.2.2.2 Receiver

The block diagram of the OGFDM-NDC receiver is shown in Fig. 4.4. Received optical signal is first converted into equivalent electrical signal by the PD.

The bipolar signal $\mathbf{Y_3}$ is regenerated as:

$$\mathbf{Y_3} = \mathbf{Y_3^+} - \mathbf{Y_3^-} \tag{4.7}$$

where, $\mathbf{Y_3^+}$ is the first subframe and $\mathbf{Y_3^-}$ is the second sub-frame received after frame demultiplexing $\mathbf{Y_4}$. Resultant $\mathbf{Y_3}$ is further demultiplexed into $\mathbf{Y_1}$ and $\mathbf{Y_2}$, to get back the complex valued signal $\mathbf{Y}$. Further, CP removal followed by MMSE detector is used to estimate the transmitted data bits.

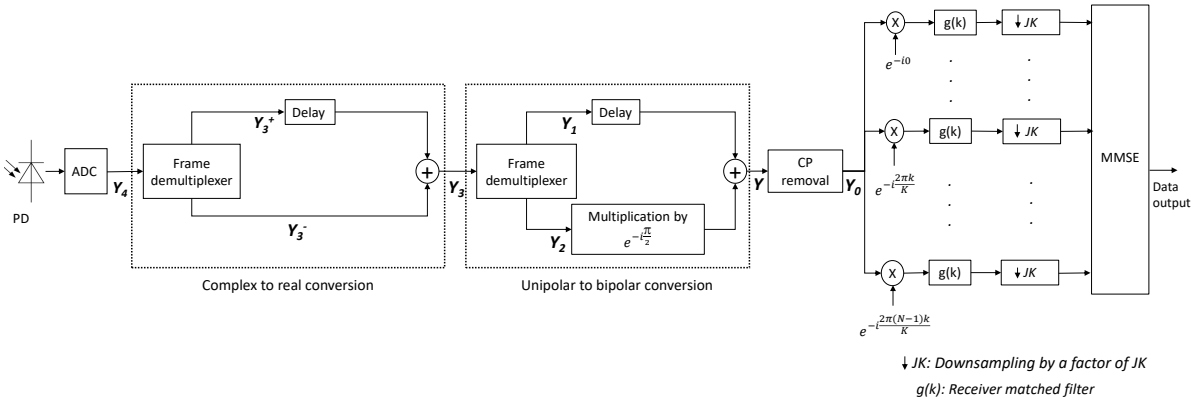


Figure 4.4: Block diagram of OGFDM-NDC receiver.

## 4.3 Performance Analysis and Comparison

This section provides mathematical analysis and comparison of the above-mentioned schemes on the basis of spectral efficiency, SER and computational complexity.

### 4.3.1 Spectral Efficiency

Due to Hermitian symmetry in DCO-OFDM, information is only transmitted over half number of subcarriers. Therefore, the bit rate of DCO-OFDM is given by [103, 106]:

$$R_{DCO} \approx \frac{N/2}{(T+T_{CP})} \log_2 M \tag{4.8}$$

where, $T$ and $T_{CP}$ are one-time slot and CP duration respectively, and $M$ is the modulation level. However, for ACO-OFDM, data is only transmitted over odd subcarriers, therefore, the ACO-OFDM bit rate is given by [103, 106]:

$$R_{ACO} = \frac{N/4}{(T + T_{CP})} \log_2 M \tag{4.9}$$

OGFDM-DC and OGFDM-NDC requires addition of CP after every $J$ time slots, unlike ACO-OFDM and DCO-OFDM which requires CP addition after every O-OFDM symbols. Thus, for OGFDM-DC bit rate is given by [103, 106]:

$$R_{OGFDM-DC} \approx \frac{JN/2}{(JT + T_{CP})} \log_2 M \tag{4.10}$$

Similarly, bit rate of OGFDM-NDC is given by [103, 106]:

$$R_{OGFDM-NDC} = \frac{JN/4}{(JT + T_{CP})} \log_2 M \tag{4.11}$$

The spectral efficiency ratio of ACO-OFDM over DCO-OFDM ($\eta_1$) can be calculated from (4.8) and (4.9) and is given as:

$$\eta_1 \approx \frac{R_{ACO}}{R_{DCO}} = \frac{1}{2} \tag{4.12}$$

Similarly, spectral efficiency ratio of OGFDM-DC and OGFDM-NDC over DCO-OFDM ($\eta_2$ and $\eta_3$ respectively) are given as follows:

$$\eta_2 \approx \frac{R_{OGFDM-DC}}{R_{DCO}} = \left( \frac{1 + \frac{T_{CP}}{T}}{1 + \frac{T_{CP}}{JT}} \right) \tag{4.13}$$

$$\eta_3 \approx \frac{R_{OGFDM-NDC}}{R_{DCO}} = \frac{(1 + \frac{T_{CP}}{T})}{2(1 + \frac{T_{CP}}{JT})} \tag{4.14}$$

For the equal number of subcarriers, same modulation level and $T_{CP}/T$ = 0.1, spectral efficiency ratio of OGFDM-DC and OGFDM-NDC over DCO-OFDM is found to be 1.07 and 0.53 respectively. Thus, it can be concluded that OGFDM-DC has the highest spectral efficiency among four schemes. The reason for higher spectral efficiency of O-GFDM (DC and NDC) is due to the fact that CP is required only between O-GFDM frames, unlike O-OFDM that requires a CP after every time slot.

### 4.3.2 SER

The SER for GFDM under AWGN is given by [98]:

$$P_e = 2\frac{\kappa-1}{\kappa} erfc(\sqrt{\gamma}) - \frac{\kappa-1}{\kappa} erfc^2(\sqrt{\gamma}) \tag{4.15}$$

where, $\gamma$ is given by:

$$\gamma = \frac{3R_T}{2(2^\mu - 1)} \frac{E_s'}{\xi N_0} \tag{4.16}$$

and

$$R_T = \frac{JN}{JN + N_{CP} + N_{CS}} \tag{4.17}$$

$\mu$ is the number of bits per QAM symbol, $\kappa = \sqrt{2^\mu}$, $N_{CP}$ and $N_{CS}$ are the length of cyclic prefix and cyclic suffix (CS) respectively, $E_s'$ is the average energy per symbol, $N_0$ is the noise power density and $\xi$ is the noise enhancement factor that is responsible for adjusting the SNR of the GFDM receiver. However, it is important to note that inorder to make GFDM compatible with VLC, two variants namely, OGFDM-DC and OGFDM-NDC are implemented in this work, each of which will result into different $\frac{E_s'}{N_0}$, as discussed in the following sections:

#### 4.3.2.1 OGFDM-DC

In order to make GFDM unipolar, DC bias has been added, which results in effective $\frac{E_s'}{N_0}$, given by [107]:

$$\frac{E_s'}{N_0} = \frac{E_s}{N_0} \frac{1}{(1 + (\frac{I_{DC}}{\sqrt{E_s}})^2)} \tag{4.18}$$

where $\frac{I_{DC}}{\sqrt{E_s}}$ is 0.5. Therefore, for OGFDM-DC, (4.16) is modified to:

$$\gamma = \frac{3R_T}{2(2^\mu - 1)} \frac{E_s}{\xi N_0} \frac{1}{(1 + (\frac{I_{DC}}{\sqrt{E_s}})^2)} \tag{4.19}$$

Further, OGFDM-DC implements MMSE receiver, so there will be no noise enhancement i.e., $\xi = 1$. In our work, 4-QAM has been used, so $\mu$ and $\kappa$ are equal to two. Using 4.15 and 4.19, theoretical SER for OGFDM-DC is obtained and plotted in Fig.3.8(a)

#### 4.3.2.2 OGFDM-NDC

In OGFDM-NDC, concept of Flip-OFDM is used to make the signal unipolar in nature. Since the effective SNR for ACO-OFDM and Flip-OFDM is same [86], therefore, the effective

received $\frac{E_s'}{N_0}$ is given by [107]

$$\frac{E_s'}{N_0} = \frac{E_s}{N_0} \tag{4.20}$$

Therefore, for OGFDM-NDC, (4.16) remains same. OGFDM-NDC also implements MMSE receiver, so $\xi = 1$. Using values of $\mu$ and $\kappa$ and (4.15), theoretical SER for OGFDM-NDC is obtained and plotted in Fig.3.8(b)

### 4.3.3 Complexity

The computational complexity of GFDM is higher than OFDM. However, by using low complexity GFDM (LC-GFDM) modem structure as proposed in [108], a substantial amount of complexity reduction can be achieved without incurring any performance loss.

In [108], the transmitter block uses DFT and IDFT matrices, which make the modulation matrix sparse and hence reduces the computational burden. In the receiver, a reduction in computational complexity is achieved by designing a low complexity MMSE detector using block diagonalization of the matrix involved. It is shown that through this block diagonalization, a substantial amount of complexity reduction in the matrix inversion and multiplication operations can be achieved. Further, equalizer used in the receiver will require fewer taps as the delay spread is small compared with symbol duration.

To have a fair comparison between OFDM, GFDM and LC-GFDM system implementations, an OFDM system transmitting $M$ concatenated symbols, each having $N$ subcarriers is considered in the analysis. Quantitative indication of the complexity of the system are shown in Table 4.1.

In Fig. 4.5, number of complex multiplications (CMs) required have been plotted against $J$ for fixed $N = 64$ for OFDM, GFDM and LC-GFDM. It is observed that the complexity order of LC-GFDM is quite close to OFDM. It is further emphasized that the proposed algorithm reported for LC-GFDM does not incur any performance penalty and maintain optimal performance. Such a substantial reduction in the number of computations makes GFDM based modem structures attractive for hardware implementation.

Table 4.1: Computational complexity

| **Schemes** | **Number of complex multiplications** |
|---|---|
| OFDM | $\frac{MN}{2} * log_2(N) + \frac{MN}{2} * log_2(N)$ |
| GFDM | $(MN)^2 + \frac{1}{3} * (MN)^3 + 2 * (MN)^2$ |
| LC-GFDM | $\frac{MN}{2} \{M + log_2(N)\} + \frac{MN}{2} \{4M + log_2(N) + 3\}$ |

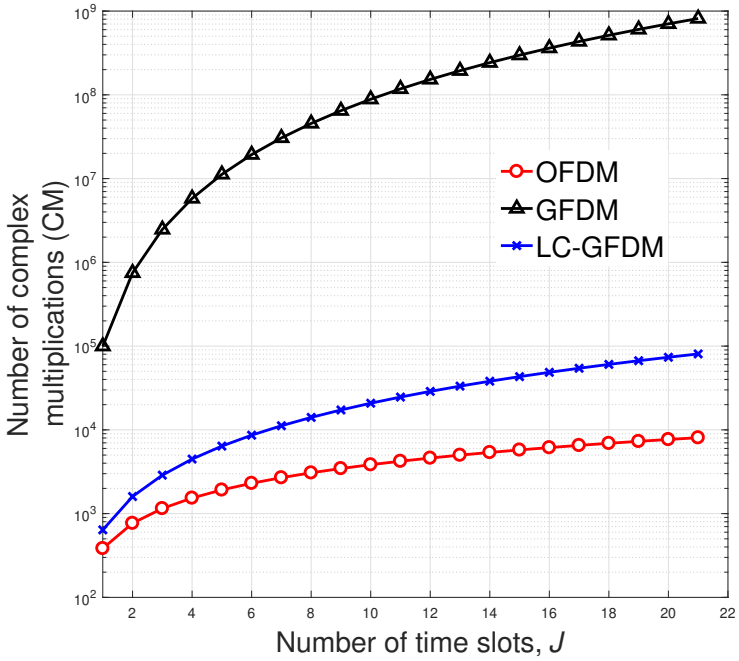


Figure 4.5: Comparison of computational complexity of OFDM, GFDM, LC-GFDM.

## 4.4 Simulation Results and Discussion

In this section, we compare DC and non-DC techniques namely the OGFDM-DC with DCO-OFDM and OGFDM-NDC with ACO-OFDM, based on their PAPR, SER and subcarrier frequency shift tolerance. Table 4.2 [5], states the optical channel parameters [37, 109, 110]. Table 4.3, shows the simulation parameters parameters [104], calculated for the condition when OGFDM-DC, DCO-OFDM, OGFDM-NDC, and ACO-OFDM are designed to have the same spectral efficiency, and accordingly the number of subcarriers are selected for these schemes.

Table 4.2: Optical channel parameters

| **Channel Parameter** | **Value** |
|---|---|
| Lambertian mode number, $m$ | 45 |
| Area of PD, $A_{\text{PD}}$ | 9.8 $mm^2$ |
| PD's field of View, $\Psi_c$ | 60° |
| Transmitter location $(x_t,y_t,z_t)$ | (2.5 m, 2.5 m, 3m) |
| Receiver location, $(x_r,y_r,z_r)$ | (2.5 m, 2.5 m, 1m ) |
| Optical concentrator gain, $g_{\text{c}}$ | 0 dB |
| Optical filter gain, $g_{\text{f}}$ | 0 dB |
| Responsivity of PD, $R_{\text{PD}}$ | 0.53 A/W |

Table 4.3: Simulation parameters

| **Parameters** | **ACO-OFDM/ DCO-OFDM** | **OGFDM-NDC/ OGFDM-DC** |
|---|---|---|
| Number of subcarriers* | 128/64 | 8/4 |
| Constellation order | 4 | 4 |
| Upsampling factor | NA | 4 |
| Signal bandwidth | 20 MHz | 20 MHz |
| Transmitter filter | Rectangular | RRC |
| Roll-off factor | NA | 0.1 |

*Calculated for the condition when OGFDM-DC, DCO-OFDM, OGFDM-NDC, and ACO-OFDM are designed to have the same spectral efficiency.

### 4.4.1 PAPR

PAPR of a transmitted signal $x(t)$ can be defined as:

$$PAPR = \frac{\max[x(t)x^*(t)]}{E[x(t)x^*(t)]} \tag{4.21}$$

A high PAPR signal requires LEDs with large dynamic range in order to avoid clipping distortion. The probability of PAPR of block greater than the threshold value ($PAPR_o$) is defined by complementary cumulative distribution function (CCDF).

Fig. 4.6(a) shows the CCDF curves for OGFDM-DC and DCO-OFDM. OGFDM-DC exhibits a superior performance compared to DCO-OFDM. Similarly, Fig. 4.6(b) shows CCDF curves for OGFDM-NDC and ACO-OFDM. It is observed that the OGFDM-NDC displays a lower PAPR than ACO-OFDM. If we set probability $(PAPR > PAPR_0)$ to $10^{-2}$ and compare the CCDF curves for all schemes, it is seen that $PAPR_0$ has values of 6.5, 15.9, 9.3, and 13.8 dB for OGFDM-DC, DCO-OFDM, OGFDM-NDC, and ACO-OFDM respectively. The PAPR reduction in O-GFDM is due to the distribution of the data among time slots and subcarriers, unlike O-OFDM where the data is transmitted only over subcarriers. Additionally, PAPR effects the illumination-to-communication conversion efficiency [19]. Therefore, reduced PAPR makes O-GFDM efficient and robust against the clipping distortion due to LED saturation.

### 4.4.2 SER

By using MATLAB simulation for the systems defined in section 4.2, the SER performance for OGFDM-DC, OGFDM-NCD, DCO-OFDM and ACO-OFDM was obtained. Fig. 4.7(a) and 4.7(b) illustrates the SER performance of OGFDM-DC and DCO-OFDM and the SER performance of OGFDM-NDC and ACO-OFDM respectively for optical channel. Further, the corresponding analytical SER is obtained substituting equation (4.19) and (4.16) into (4.15),

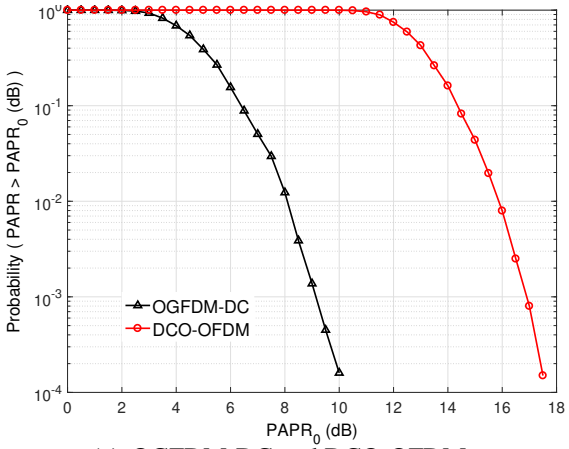


(a) OGFDM-DC and DCO-OFDM.

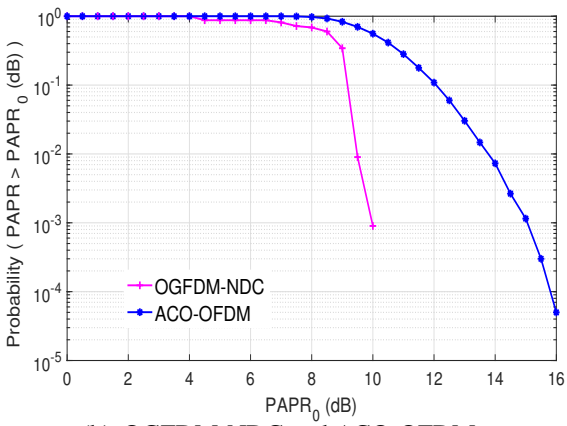


(b) OGFDM-NDC and ACO-OFDM.

Figure 4.6: CCDF distribution of PAPR (dB) for OGFDM and corresponding O-OFDM counterparts.

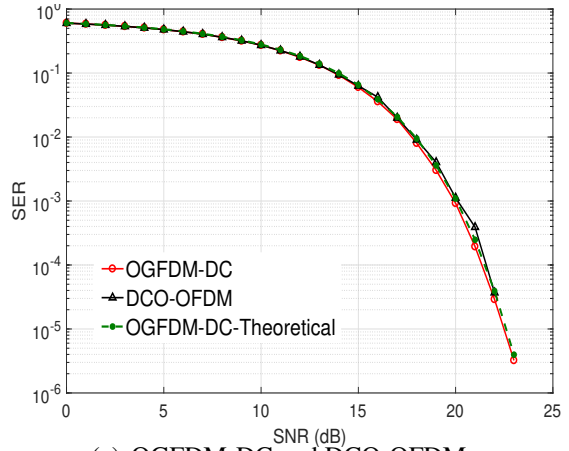


(a) OGFDM-DC and DCO-OFDM.

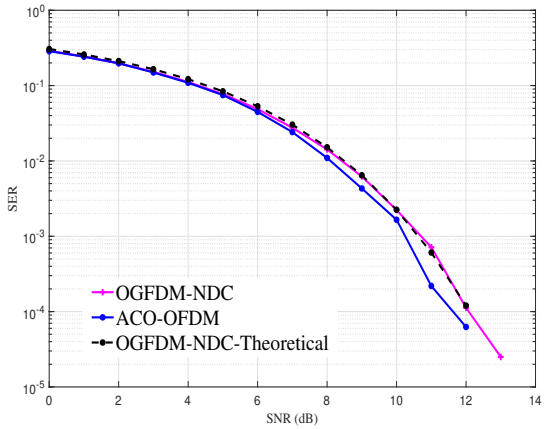


(b) OGFDM-NDC and ACO-OFDM

Figure 4.7: SER Performance of OGFDM and corresponding O-OFDM counterparts.

for OGFDM-DC and OGFDM-NCD, respectively. Based on these equations the analytical SER have been plotted in Fig. 4.7.When a zero forcing equalizer is used for O-GFDM, the performance of O-GFDM closely matches to the O-OFDM counterparts.

### 4.4.3 Tolerance to Subcarrier Frequency Shift at Transmitter and Receiver

The local oscillator responsible for sub-carrier frequency up-conversion at transmitter and down-conversion at the receiver may have a mismatch between them. It gives rise to ICI that

significantly degrades the systems performance [111]. The mismatch is defined by normalized frequency shift ($\varepsilon$), which is the ratio of frequency shift between transmitter and receiver to intercarrier spacing. The performance of OGFDM-DC and DCO-OFDM are shown in Fig. 4.8(a) with respect to subcarrier frequency shift. It is observed that DCO-OFDM is unable to achieve the desired SER of $10^{-3}$ for $\varepsilon \geq 0.09$, it reaches to irreducible error floor condition where even an infinite SNR cannot provide the desired performance.

From Fig. 4.8(b), the performance of OGFDM-NDC and ACO-OFDM for different subcarrier frequency shift is observed, ACO-OFDM is less tolerant to subcarrier frequency shift errors as it can not provide the desired SER performance for $\varepsilon \geq 0.08$. As subcarrier frequency shift increases, the orthogonality of O-OFDM system is disturbed which results in poor performance, whereas O-GFDM being inherently non-orthogonal is not severely affected by subcarrier frequency shift.

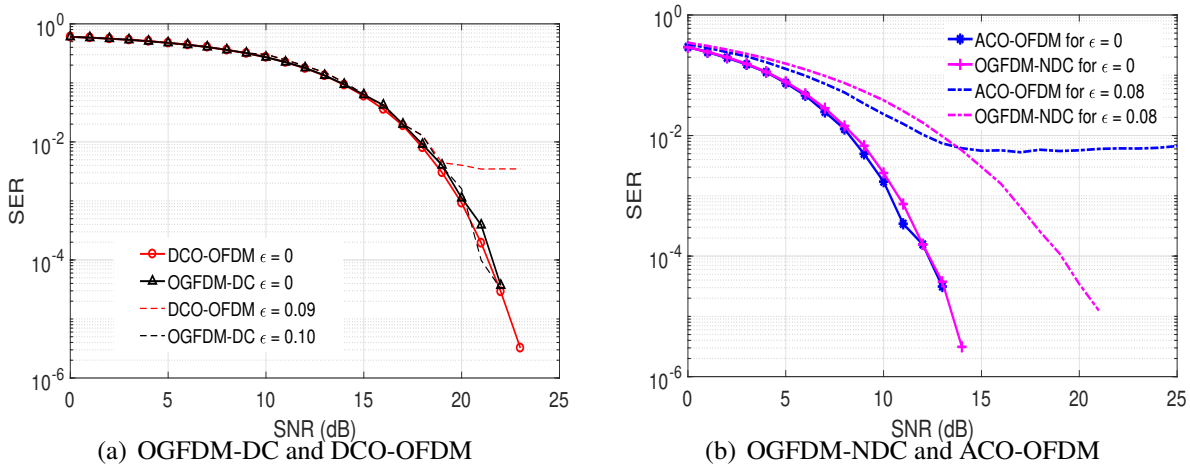


(a) OGFDM-DC and DCO-OFDM (b) OGFDM-NDC and ACO-OFDM

Figure 4.8: Tolerance to frequency shift for OGFDM and corresponding O-OFDM counterparts.

### 4.4.4 Power Saving

The power saving ($P_{saving}$) achieved by the O-GFDM over the O-OFDM counterpart is defined as:

$$P_{saving} = 10\log_{10}\left(\frac{P_1}{P_2}\right) \tag{4.22}$$

where, $P_1$ is the DC power consumed by the transmitter for transmitting O-OFDM signal and $P_2$ is the corresponding power for transmitting the O-GFDM counterpart. DC power ($P$)

consumed by a scheme is calculated by [97].

$$P = \frac{P_{avg} * \xi}{\kappa} \tag{4.23}$$

s where, $\xi$ is the inverse function of the CCDF for a given clipping probability $(PAPR > PAPR_0)$, $\kappa$ is a constant and $P_{avg}$ is the average power per time slot. From simulation results, $P_{avg}$ is found to be 0.035, 0.36, 0.50 and 0.50 for ACO-OFDM, OGFDM-NDC, DCO-OFDM and OGFDM-DC respectively. The value of $\xi$ is calculated when probability $(PAPR > PAPR_0)$ is set to $10^{-3}$ in the CCDF curve (Fig. 4.6). By substituting the corresponding values in (4.22) and (4.23), $P_{saving}$ for OGFDM-DC over DCO-OFDM is found to be 8.74 dB and for OGFDM-NDC over ACO-OFDM is found to be $-2.28$ dB. There is a net saving of power for OGFDM-DC over DCO-OFDM due to the fact that PAPR is significantly lower for OGFDM-DC as compared to DCO-OFDM and $P_{avg}$ is same for both the schemes. On the other hand, $P_{saving}$ for OGFDM-NDC over ACO-OFDM is negative because of the higher $P_{avg}$ of OGFDM-NDC as compared to ACO-OFDM.

## 4.5 Summary

The results of this chapter are summarized in Table 4.4.

Table 4.4: Summary of the OGFDM results

| **Parameters** | **DCO-OFDM** | **OGFDM-DC** | **ACO-OFDM** | **OGFDM-NDC** |
|---|---|---|---|---|
| $PAPR_o$ for CCDF prob $= 10^{-3}$ | 15.9 | 8 | 15.1 | 10 |
| SNR (dB) for FEC limit | 19 | 19.2 | 10.3 | 10.7 |
| Tolerance to subcarrier frequency shift * | 0.09 | 0.10 | 0.08 | 0.10 |
| Spectral efficiency gain w.r.t. DCO-OFDM | 1 | 1.07 | 0.5 | 0.53 |
| Power saving in O-GFDM (dB) | 8.74 | | -2.28 | |

*Tolerance to subcarrier frequency shift when SNR is increased by 10 dB for target SER = $10^{-3}$

GFDM is being considered by the wireless community for 5G systems because of its flexible structure and other advantages like simple transmit/receive waveforms and low power consumption due to reduced PAPR. In this chapter, we proposed O-GFDM scheme for VLC and evaluated it based on spectral efficiency, complexity, power saving, PAPR, SER, and subcarrier frequency shift tolerance. Results were compared with existing DCO-OFDM and ACO-OFDM schemes. From the Table, we observed a significant reduction in PAPR for proposed O-GFDM

schemes compared to O-OFDM counterparts. However, the SER and subcarrier frequency shift tolerance performance of the proposed O-GFDM matched the corresponding O-OFDM. Further, the analytical SER expressions of optical GFDM were derived, and results were validated through simulations. The proposed schemes provided better spectral efficiency and significant power saving in case of OGFDM-DC. However, this came at the cost of increased complexity, which can be reduced by using a low-complexity GFDM (LC-GFDM) modem structure. It is, therefore, concluded that O-GFDM is an improved alternative to O-OFDM. The proposed O-GFDM based VLC is expected to very well gel with next generation systems to deliver seamless last-mile communication services and provide greater flexibility to optimize the network using software-defined networking.

Chapter 5

# Overview of LiFi and its Coexistence with WiFi

This chapter provides overview of HLWN in Section 5.1 followed by brief discussion on the HLWN system model in Section 5.2. In Section 5.3, the RSS and optimization based Load balancing for HLWN are discussed. The simulation results are presented in Section 5.3.3. Finally, Section 5.4 summaries the chapter.

## 5.1 Introduction

The point-to-point VLC discussed in previous chapters can be extended to fully networked, bidirectional, and high-speed optical wireless communication technology known as LiFi. The major differences between VLC and LiFi are highlighted in Table 5.1.The universal availability of LEDs, license-free deployment and data rate of Gbps order, makes LiFi an attractive choice for indoor communications [112]. However, LiFi suffers from a major drawback of blockage. Thus, the throughput of LiFi users fluctuates spatially, as a result stand-alone LiFi can not guarantee the QoS to the user through out the indoor environment. On the other hand, WiFi can support moderate data rates with more ubiquitous coverage. Table 5.2 summaries the key features of LiFi and WiFi technology. From this, it is obvious that LiFi and WiFi operate in non-overlapping spectrums and while LiFi can support high data rates when the receiver is in direct LoS, WiFi can support moderate data rates with more ubiquitous coverage. Therefore, coexistence of LiFi and WiFi technologies to form a heterogeneous LiFi WiFi network (HLWN) is suggested. A HLWN provides higher system throughput as compared to standalone LiFi or WiFi networks [26].

| Parameter | VLC | LiFi |
|---|---|---|
| Spectrum | VL | IR/VL/UV |
| Mobility Support | optional | Mandatory |
| Communication topology | Unidirectional or bidirectional | Bidirectional |
| Communication Mode | Point-to-point or point-to-multipoint | Point-to-multipoint |

Table 5.1: Differences between VLC and LiFi [1].

| Parameters | LiFi | WiFi |
|---|---|---|
| Coverage range | 3-5m | 10m |
| Datarate | 10-100 Gbps [113] | Few Gbps |
| Frequency spectrum | VL/IR | RF |
| IEEE standard | 802.15 | 802.11 |
| Security | Highly secure | Less secure |
| Communication power consumption | Very low | Relatively high |
| Interference from other RF devices | No | High |

Table 5.2: Comparison between LiFi and WiFi [8].

## 5.2 HLWN System Model

The downlink HLWN considered in this work is assumed to be deployed in a typical office room of $5 \times 5 \times 3$ m$^3$, as shown in Fig. 5.1. The HLWN system has four LiFi APs and one WiFi AP. The WiFi AP is located in the center of the room ceiling and is assumed to provide coverage to the entire room, whereas the coverage of each LiFi AP is confined to a smaller area, called an attocell. The focus of this work is to understand the effectiveness of RL based LB in HLWN, therefore, a simple scenario with four LiFi APs [9, 114] has been considered in this study. The proposed work is scalable to a larger room with more number of APs and users. Furthermore, as all LiFi APs reuse the same modulation bandwidth, therefore, users in overlapping attocell areas may experience optical interference, which is treated as additional noise in the system. The spectrum reuse in LiFi provides the advantage of higher spatial-spectral efficiency at the cost of a significantly low data rate in the overlapping attocell areas. The LiFi and WiFi channel models used for HLWNs are defined in Sections 5.2.1 and 5.2.2. A central controller (CC) unit is required for efficient utilization of the HLWN [27]. In this work, it is assumed that a CC is connected to both WiFi and LiFi APs through an error-free feedback link, and it is responsible for making the load balancing decisions. Besides, the users are distributed across the room, and they may follow different mobility models, explained in Section 6.2.1 and Section 7.2.1. Furthermore, the users are assumed to be accessing the high definition (HD) videos from the internet, hence their require data rates are modeled as a Poisson process with the parameter $R_o$. In this work, to support multiple user connections to a single AP, different types of medium access methods have been explored in this thesis;

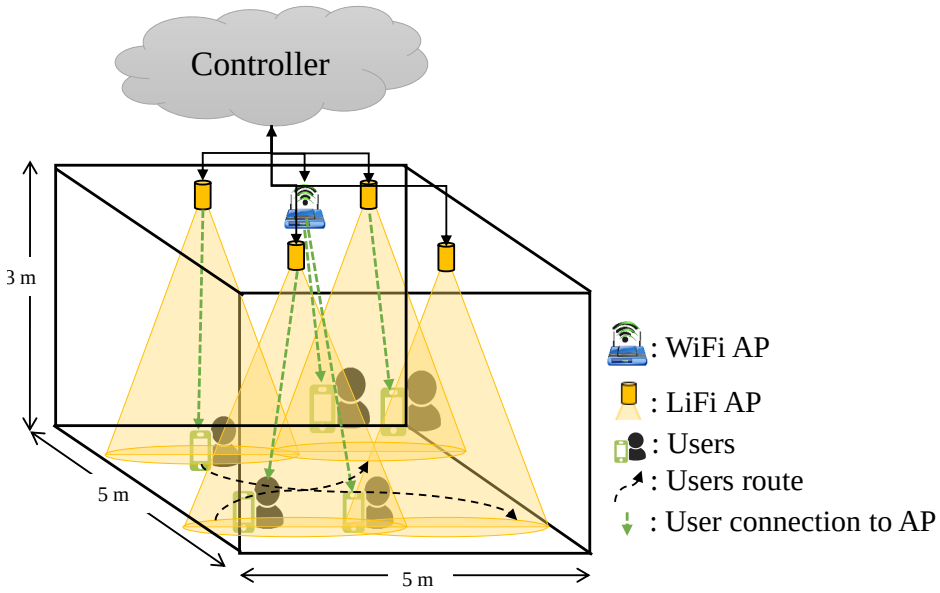


Figure 5.1: Schematic diagram of a HLWN.

namely, time-division multiple access (TDMA), orthogonal frequency-division multiple access (OFDMA), and carrier-sense multiple access with collision avoidance (CSMA/CA) [115].
In the HLWN, the set of users is denoted by $\mathbb{U} = \{\mu | \mu \in [1, N_{\text{u}}]\}$ . The set of LiFi APs is denoted by $\mathbb{LAP} = \{\alpha | \alpha \in [1, N_{\text{AP-LiFi}}]\}$ and WiFi AP is denoted as $\mathbb{W}$. The complete AP set is given by $\mathbb{AP} = \{\mathbb{W}, \mathbb{LAP}\}$ . The total number of APs and users present in the system are represented by $N_{\text{AP}} = N_{\text{AP-LiFi}} + N_{\text{AP-WiFi}}$ and $N_{\text{u}}$, respectively. The data requirement of each user $\mu$ is given by $R_{\mu}$.

### 5.2.1 LiFi Model

The signal-to-noise ratio (SNR) for the user $\mu$ connected to LiFi AP $\alpha$ is represented as $SNR_{\mu,\alpha}$, and can be expressed as:

$$SNR_{\mu,\alpha} = \frac{(H_{\text{LiFi}(\mu,\alpha)} P_{\text{opt}} R_{\text{PD}})^2}{N_{\text{LiFi}} B_{\text{LiFi}}}, \tag{5.1}$$

where $H_{\text{LiFi}(\mu,\alpha)}$ is the channel gain between AP $\alpha$ and user $\mu$, $R_{\text{PD}}$ indicates photo receiver responsivity , $P_{\text{opt}}$ represents transmitted optical power, $N_{\text{LiFi}}$ is the noise spectral density of LiFi, $B_{\text{LiFi}}$ indicates the LiFi AP bandwidth. It may please be noted that the digital modulation techniques are common for both VLC and LiFi system [116], thus all the physical layer equations are valid for both systems. The value of $H_{\text{LiFi}(\mu,\alpha)}$ can be calculated using (2.3), (2.9) and (2.11). It is important to note that as the same frequency is reused in each LiFi AP,

therefore, the signal received from other than intended LiFi AP is perceived as interference. Thus, the signal-to-interference-noise ratio (SINR) for the user $\mu$ connected to LiFi AP $\alpha$ is denoted by $SINR_{\mu,\alpha}$ and can be expressed as:

$$SINR_{\mu,\alpha} = \frac{(H_{\text{LiFi}(\mu,\alpha)} P_{\text{opt}} R_{\text{PD}})^2}{N_{\text{LiFi}} B_{\text{LiFi}} + \sum_{\beta \in \mathbb{AP} \setminus \{\alpha\}} (H_{\text{LiFi}(\mu,\beta)} P_{\text{opt}} R_{\text{PD}})^2} \tag{5.2}$$

where $H_{\text{LiFi}(\mu,\beta)}$ is the channel gain between interfering LiFi APs $\beta$ and the user $\mu$ and $\mathbb{AP} \setminus \{\alpha\}$ represents a set that includes all elements of set $\mathbb{AP}$ excluding element $\alpha$. The lower bound on achievable data rate of the user $\mu$ connected to LiFi AP $\alpha$ can be calculated using [9, 28]:

$$dr_{\mu,\alpha} = \frac{B_{\text{LiFi}}}{2} \log_2 \left(1 + \left(\frac{6}{\pi e}\right) SINR_{\mu,\alpha}\right). \tag{5.3}$$

The simulation parameters used for LiFi channel are summarized in Table 5.3 [9, 117].

Table 5.3: LiFi channel parameters

| **Channel Parameter** | **Symbol** | **Value** |
|---|---|---|
| Height difference between the user and AP | $h$ | 2 m |
| Area of PD | $A_{\text{PD}}$ | 1 cm$^2$ |
| The gain of opitcal filter | $g_{\text{f}}$ | 1 |
| Half intensity radiation angle | $\Phi_{1/2}$ | 60° |
| Field of View (FOV) of PD | $\Psi_c$ | 60° |
| Responsivity | $R_{\text{PD}}$ | 0.53 A/W |
| Reflection coefficient | $\rho$ | 0.8 |
| Transmit opitcal power per LiFi AP | $P_{\text{opt}}$ | 3 Watt |
| Bandwidth per LiFi AP | $B_{\text{LiFi}}$ | 40 MHz |
| PSD of noise in LiFi | $N_{\text{LiFi}}$ | $10^{-21}$ $A^2$/Hz |

### 5.2.2 WiFi Model

The SNR for user $\mu$ connected to WiFi AP $\alpha$ is given by:

$$SNR_{\mu,\alpha}(f) = \frac{|G_{\mu,\alpha}|^2(f) P_{\text{T}}}{N_{\text{WiFi}} B_{\text{WiFi}}}, \tag{5.4}$$

where $G_(\mu,\alpha)(f)$ represents WiFi channel gain, $P_{\text{T}}$ indicates transmitted power, $N_{\text{WiFi}}$ denotes noise spectral density for WiFi receiver, and $B_{\text{WiFi}}$ is the bandwidth of WiFi AP. The WiFi

channel gain, $G_(\mu,\alpha_1)(f)$ is given by [9]:

$$G_{\mu,\alpha}(f) = \sqrt{10^{\frac{-L(d)}{10}}} h_{\mathrm{r}}, \tag{5.5}$$

where $f$ indicates the carrier frequency, $h_{\mathrm{r}}$ represents the small-scale fading gain which follows independent identical Rayleigh distribution with 2.46 dB average power. The $L(d)$ denotes the large-scale fading loss and it is given as [9]:

$$L(d) = \begin{cases} L_{\mathrm{FS}}(d) + X_{\mathrm{SF}}, & d < d_{\mathrm{BP}} \\ L_{\mathrm{FS}}(d_{\mathrm{BP}}) + 35\log(\frac{d}{d_{\mathrm{BP}}}) + X_{\mathrm{SF}}, & d \geq d_{\mathrm{BP}} \end{cases}, \tag{5.6}$$

where, $d$ represents distance between user $\mu$ and WiFi AP $\alpha$, $L_{\mathrm{FS}}$ denotes the free space loss, $d_{\mathrm{BP}}$ indicates breakpoint distance and $X_{\mathrm{SF}}$ refers to the shadowing loss. The free space loss can be calculated by $L_{\mathrm{FS}}(d) = 20\log_{10} d + 20\log_{10} f - 147.5$ (dB). As the system model consist of single WiFi AP, there will be no interference for WiFi users The achievable data rate between WiFi AP $\alpha$ and user $\mu$ , can be calculated using:

$$dr_{\mu,\alpha} = B_{\mathrm{WiFi}} \log_2(1 + SNR_{\mu,\alpha}). \tag{5.7}$$

The WiFi channel parameters used in simulation are stated in Table 5.4 [9, 117].

Table 5.4: WiFi channel parameters

| **Channel Parameter** | **Symbol** | **Value** |
|---|---|---|
| Breakpoint distance | $d_{\mathrm{BP}}$ | 5 cm |
| Shadowing loss | $X_{\mathrm{SF}}$ | 3 dB |
| Central carrier frequency | $f_{\mathrm{c}}$ | 2.4 GHz |
| WiFi AP's transmit Power | $P_{\mathrm{WiFi}}$ | 20 dBm |
| WiFi AP's bandwidth | $B_{\mathrm{WiFi}}$ | 20 MHz |
| PSD of noise in WiFi | $N_{\mathrm{WiFi}}$ | -174 dBm/Hz |

## 5.3 Load Balancing in HLWN

### 5.3.1 Received Signal Strength (RSS) Based Load Balancing

Conventionally the RSS method selects the AP that offers highest signal strength. However, in a heterogeneous LiFi and WiFi network since the bandwidth and physical receiver noise differs for LiFi and WiFi, therefore, received signal strength does not fully represent the quality of channel [9, 117]. Therefore, the SNR is taken into account in RSS based load balancing

for heterogeneous LiFi WiFi networks. It may please be noted that the term RSS and signal strength strategy (SSS) are used interchangeably throughout this thesis. The objective function of the RSS method for a given user $\mu$ is defined as:

$$\max_{\alpha} \; SNR_{\mu,\alpha} \quad \text{s.t} \;\; \alpha \in \mathbb{AP}. \tag{5.8}$$

where, $\mathbb{AP}$ is the set of APs including one WiFi and four LiFi APs and $SNR_{\mu,\alpha}$ represents the SNR values between $\mu$ user and $\alpha$ AP, which can be calculated by (5.4) and (5.1) for WiFi and LiFi APs, respectively.

### 5.3.2 Optimization Based Load Balancing

For the optimum load balancing in HLWN, the optimization problem can be defined as:

$$\begin{aligned} \max_{g_{\mu,\alpha}k_{\mu,\alpha}} \sum_{\mu\in\mathbb{U}}\sum_{\alpha\in\mathbb{AP}} g_{\mu,\alpha}\log\left(\frac{dr_{\mu,\alpha}k_{\mu,\alpha}}{R_\mu}\right) \\ \text{s.t.} \sum_{\mu\in\mathbb{U}} (g_{\mu,\alpha}k_{\mu,\alpha}) = 1 \,\forall \alpha \in \mathbb{AP} \\ \sum_{\alpha\in\mathbb{AP}} g_{\mu,\alpha} = 1 \,\forall \mu \in \mathbb{U} \\ g_{\mu,\alpha} \in \{0,1\}, k_{\mu,\alpha} \in [0,1], \forall \mu \in \mathbb{U}, \forall \alpha \in \mathbb{AP} \end{aligned} \tag{5.9}$$

where, the optimization variable $k_{\mu,\alpha}$ defines the time slot allocated to the users $\mu$ connected to AP $\alpha$ and the binary optimization variable $g_{\mu,\alpha}$ indicates the connection between AP $\alpha$ and user $\mu$. The $g_{\mu,\alpha}$ is defined as:

$$g_{\mu,\alpha} = \begin{cases} 1, & \text{user } \mu \text{ is connected to AP } \alpha \\ 0, & \text{user } \mu \text{ is not connected to AP } \alpha \end{cases} \tag{5.10}$$

The first constraint of (5.9) ensures that the sum of time allocation of all users associated to one AP is 1 and the second constraint states that each user can get connected to only one AP at a time. This optimisation problem (5.9) is a mixed integer non-linear programming (MINLP) problem which is mathematically intractable. Therefore, it is not possible to obtain a closed form solution for this problem.

However, it is possible to find a sub-optimal solution for (5.9). In [118], the authors have tried to solve similar problem to maximize the network throughput, however, throughput is not appropriate parameter to ensure QoS. Therefore, in this work, we tried to maximize the user satisfaction, which is defined as the ratio of achieved data-rate ($dr_{\mu,\alpha}k_{\mu,\alpha}$) by the requested data-rate ($R_\mu$) for each user. We have divided MINLP (5.9) into two sub-problems:

AP assignment ($g_{\mu,\alpha}$) and resource allocation ($k_{\mu,\alpha}$). For given AP $\alpha$, $g_{\mu,\alpha}$, the set and total user connected to AP $\alpha$ can be represented by $U_\alpha$ and $M_\alpha$. In this case, optimum $k_{\mu,\alpha}$ is [118]

$$k_{\mu,\alpha} = \frac{1}{M_\alpha} \tag{5.11}$$

Thus, the problem (5.9) can be rewritten as:

$$\begin{aligned} \max_{g_{\mu,\alpha} M_\alpha} \sum_{\mu\in\mathbb{U}} \sum_{\alpha\in\mathbb{AP}} g_{\mu,\alpha} \log\left(\frac{dr_{\mu,\alpha}}{R_\mu M_\alpha}\right) \\ \text{s.t.} \sum_{\mu\in\mathbb{U}} g_{\mu,\alpha} = M_\alpha \, \forall \alpha \in \mathbb{AP} \\ \sum_{\alpha\in\mathbb{AP}} g_{\mu,\alpha} = 1 \, \forall \mu \in \mathbb{U} \\ g_{\mu,\alpha} \in \{0,1\}, k_{\mu,\alpha} \in [0,1], \forall \mu \in \mathbb{U}, \forall \alpha \in \mathbb{AP} \end{aligned} \tag{5.12}$$

To solve this problem, the Lagrangian method is utilized. For the constraints, two Lagrangian multipliers $\lambda_\mu$ and $w_\alpha$ are used. The Lagrangian function for this problem, can be written as:

$$L = \sum_{\mu\in\mathbb{U}} \sum_{\alpha\in\mathbb{AP}} g_{\mu,\alpha} \log\left(\frac{dr_{\mu,\alpha}}{R_\mu M_\alpha}\right) + \sum_{\alpha\in\mathbb{AP}} w_\alpha (M_\alpha - \sum_{\mu\in\mathbb{U}} g_{\mu,\alpha}) + \sum_{\mu\in\mathbb{U}} \lambda_\mu (1 - \sum_{\alpha\in\mathbb{AP}} g_{\mu,\alpha}) \tag{5.13}$$

This equation can be rearranged and divided into two sub-problems, as:

$$L_1 = \sum_{\mu\in\mathbb{U}} \sum_{\alpha\in\mathbb{AP}} \left[ g_{\mu,\alpha} \log\left(\frac{dr_{\mu,\alpha}}{R_\mu}\right) - w_\alpha - \lambda_\mu \right] \tag{5.14}$$

$$L_2 = \sum_{\alpha\in\mathbb{AP}} \left[ M_\alpha (w_\alpha - \log(M_\alpha)) \right] + \sum_{\mu\in\mathbb{U}} \lambda_\mu \tag{5.15}$$

The optimum value of $g_{\mu,\alpha}$ is calculated as:

$$g_{\mu,\alpha} = \begin{cases} 1 & \alpha = \text{argmax}\left( \log(\frac{dr_{\mu,\alpha}}{R_\mu}) - \lambda_\mu - \omega_\alpha \right) \\ 0 & \text{otherwise} \end{cases}, \tag{5.16}$$

$$M_\alpha = \exp(w_\alpha - 1) \tag{5.17}$$

where, $\lambda_\mu$ and $\omega_\alpha$ are the Lagrangian's multipliers and their values can be determined by using similar procedure as mentioned in [118].

### 5.3.3 Results and Discussion

The results of the proposed optimized load balancing scheme are compared against the RSS based user association scheme in terms of average network throughput and user satisfaction. In order to obtain these results, a room of 5 m x 5 m x 3 m with one WiFi AP in centre of the room and four LiFi APs, as shown in Fig. 5.1 has been simulated in MATLAB. The simulation parameters used for LiFi and WiFi channel are summarized in Table 5.3 and Table 5.3 and Table 5.4 [9, 117].

The user association for RSS and proposed optimization-based scheme obtained using equation (5.8) and (5.16), respectively. Fig. 5.2 illustrates the user association for RSS and proposed optimization-based scheme. It can be noted that in RSS based method, most of the users are connected to WiFi, hence the WiFi is overloaded, however, in case of proposed optimized method the load of the network is properly balanced between the LiFi and WiFi APs, i.e., more users are associated with LiFi APs, thus, WiFi AP resources are freed up and can be utilized for mobile users.

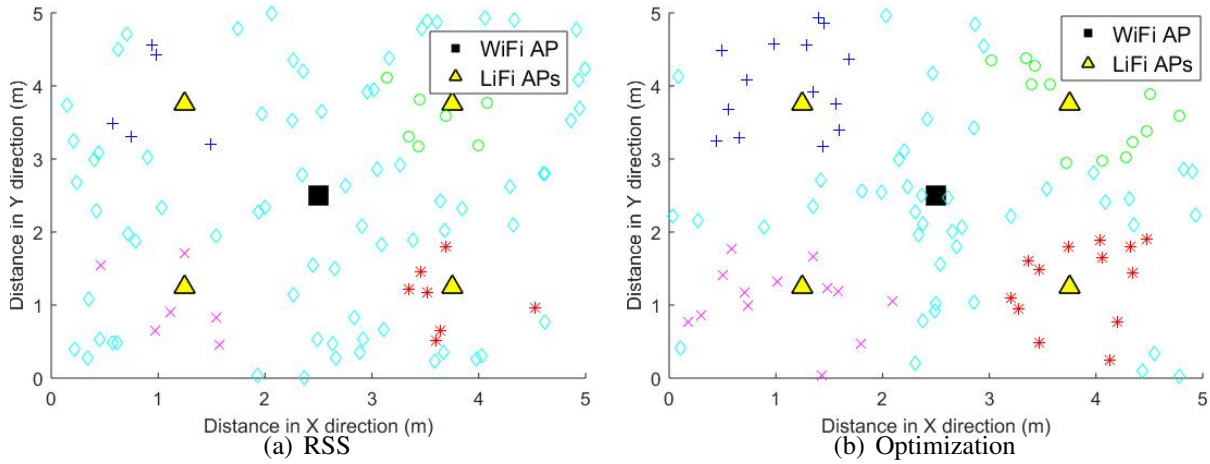


(a) RSS (b) Optimization

Figure 5.2: User Association in HLWN.

The average throughput is obtained by $Tavg = \frac{\Sigma_{\mu \in \mathbb{U}} dr_{\mu,\alpha} k_{\mu,\alpha}}{N_u}$. The effect of number of users on system throughput for two schemes is shown in Fig. 5.3. It can be observed that the system throughput decreases with increase in the number of users. Further, it can be noted that the optimized scheme is able to provide significantly high throughput as compared to the conventional RSS based scheme. However, as the number of users increases, the network saturates and hence the difference in system throughput for the two schemes decrease.
The user satisfaction is calculated as $\min(1, \frac{dr_{\mu,\alpha} k_{\mu,\alpha}}{R_\mu})$, where $R_\mu$ is the data rate requirement of user $\mu$. In Fig. 5.4, the cumulative density function (CDF) of user satisfaction is presented. It can be observed that for optimization-based user association approx. 46% of the users are

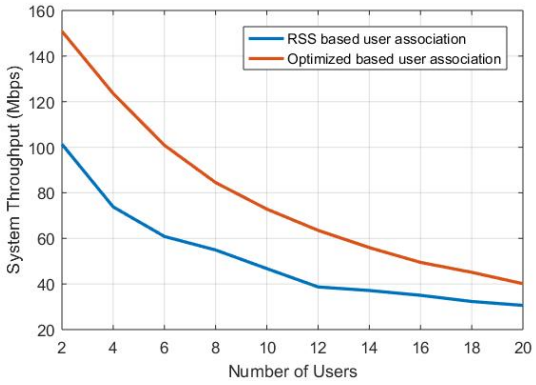


Figure 5.3: System throughput

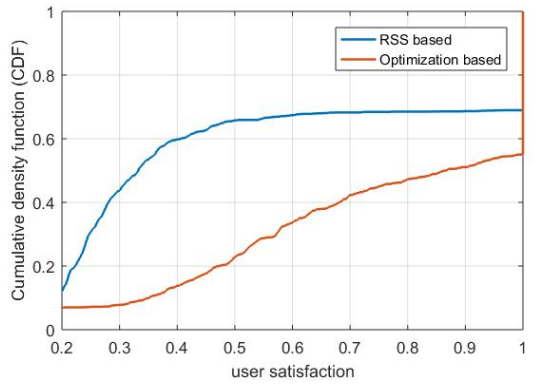


Figure 5.4: CDF of User satisfaction

fully satisfied (i.e., $US_{\mu,\alpha} = 1$), whereas only 32% of the users are able to achieve the full user satisfaction for RSS based association. Further, it can be interpreted from the results that if a user satisfaction threshold of 0.51 is considered for the system, in optimization-based scheme around 80% of users will achieve the desired performance whereas in RSS based scheme only 34% of the users will achieve the desired performance.

## 5.4 Summary

In this chapter, an overview of a HLWN system was presented along with the details related to LiFi and WiFi channel model. Further, an optimization based load balancing for HLWN has been explored in this chapter and its performance has been compared against the conventional RSS HLWN LB in terms of average network throughput and user satisfaction. It was observed that optimized scheme provided significant improvement in system throughput and user satisfaction as compared to conventional RSS based user association method. The improvement in system throughput was higher for low-density network (i.e., less than 10), however as the

number of user increased, the network saturated. For low user density, the optimized method provided at least 50% improvement in throughput as compared to conventional RSS based method. Further, for minimum user satisfaction threshold of 0.51, around 80% of the users were able to achieve the desired performance for optimization-based user association whereas in case of RSS based method, only 34% of the users were able to achieve the desired performance. It is interesting that optimization method provided an improvement but it is at the cost of higher complexity. In the next chapter, we will explore RL based HLWN LB and will compare its performance against optimization based HLWN LB.

Chapter 6

# Reinforcement Learning Based Near-optimal Load Balancing for HLWNs

In the last chapters, an optimization based HLWN LB was proposed. In this chapter, we will explore the application of RL in HLWN LB. This chapter evaluates the performance of RL based HLWN LB system in the presence of LiFi CCI, randomwaypoint (RWP) and hotspot random waypoint (HRWP) mobility model. Further, for the sake of simplicity time-division multiple access (TDMA) has been considered in this chapte. The brief introduction and contributions related to the above mentioned system are given in Section 6.1 followed by Section 6.2 which provides a brief overview of the HLWN system. Section 6.3 describes the RL based HLWN LB. Section 5.4 derives the closed-form expression of SER and system capacity. The simulation results are presented in Section 6.4. Finally, Section 6.5 concludes the chapter.

## 6.1 Introduction

The VLC can be extended to LiFi which is fully networked, bidirectional, and high-speed optical wireless communication. The universal availability of LEDs, license-free deployment and data rate of Gbps order, makes LiFi an attractive choice for indoor communications [112]. However, LiFi suffers from a major drawback of blockage. Thus, the throughput of LiFi users fluctuates spatially, as a result stand-alone LiFi can not guarantee the QoS to the user through out the indoor environment. While LiFi can support high data rates when the receiver is in direct LoS, WiFi can support moderate data rates with more ubiquitous coverage. Therefore, coexistence of LiFi and WiFi technologies to form a HLWN is suggested. A HLWN provides higher system throughput as compared to standalone LiFi or WiFi networks [26]. An appropriately designed HLWN can support higher data rate, better user satisfaction, outage performance,

and lower handover rates [27]. The problem of load balancing in HLWN is a MINLP problem. It may be noted that the problem of throughput maximization in HLWN is neither concave nor convex in binary connection variable [119, 120], therefore, the conventional optimization algorithms fails to find a global optimum for this problem. Hence, researchers have started exploring machine learning based solution for the aforementioned problem. The problem of AP assignment in HLWN has been addressed by different methods, which can broadly be classified into three categorise, namely, optimization, fuzzy logic (FL) and machine learning. Different studies have used optimization based method in order to achieve different objectives in hybrid LiFi WiFi notworks. In [121], user mobility and handover signalling overheads are taken into account, and the utility function considered both the system throughput and fairness. Further, in that work, two different cases, namely, with and without optical co-channel interference (CCI) were considered. In [119], the optimization problem for maximizing the achievable user QoS with certain outage probability is formulated and solved by two different optimization algorithms that jointly and separately optimize the resource allocation and AP assignment. In [121], a novel Load balancing method is proposed for optimizing the network throughput over a period of time instead of maximizing the instantaneous network throughput. In [122], authors have formulated a power allocation optimization problem for the hybrid LiFi WiFi scenario, under common backhaul constraint. In [123], the authors formulated an optimization problem in terms of power and bandwidth allocation in order to maximize the energy efficiency of a heterogeneous VLC RF communication system. In [124], the authors have presented unified resource allocation and mobility management algorithm for indoor VLC networks based upon particle swarm optimization. It is important to note that all these schemes are formulated as optimization problems to be solved at every time-step, therefore, resulting into a high computational complexity. Other studies have used FL method to assign APs to users. In [125], authors have explored FL based dynamic load balancing scheme in order to mitigate the handover effects. This scheme considers the desired data rate and speed of user, to determine whether a handover is required or not. The user speed information is exploited by FL, so that more suitable APs can be assigned to users moving at a fast speed or users experiencing transient shadowing effect. Furthermore, by using FL ping-pong pattern of handover was avoided. In [117], two-stage AP selection method was proposed, the first stage determines the association of users to WiFi AP based on FL, and the second stage assigns the remaining users to the LiFi network. The results achieved by this method was close to the optimization based method in terms of throughput, at a significantly reduced complexity.

Some studies have explored machine learning based approaches to solve the problem of AP assignment in HLWN. In [126], authors proposed the concept of responsive association where the associations are established by taking into account both the users' current geo-locations and their current queue backlog states. Furthermore, they considered the concept of anticipatory

association where the associations are established by taking into account both the users' time-variant geo-locations and their evolving queue backlog states. They have reported the results in terms of delay versus throughput trade-offs. In [127], authors proposed transfer learning based network selection algorithm, i.e., reinforcement learning with knowledge transfer. Specifically, in their work, context information is leveraged to tackle the network selection on two aspects. On one hand, the asymmetric uplink and downlink performance requirements of traffic are explicitly modeled. On the other hand, some distinguishing features of network as well as the stationary distribution law of network load are used to assist the algorithm design. Their work is different from proposed work as reinforcement learning algorithm used is Q-Learning with knowledge transfer whereas in our work we have used trust region policy optimization (TRPO) method. Moreover, their work only reported the improvement in the reward which is a function of instantaneous uplink and downlink throughput. However, the QoS parameters: user's satisfaction and fairness has not been studied in that paper. In [128], authors presented AP selection strategies for HLWN based on the multi-armed bandit, where the decision probability distribution is updated based on the 'exponential weights for exploration and exploitation' algorithm and the 'exponentially weighted algorithm with linear programming' algorithm. The proposed work is different from the earlier work as the it uses single agent gradient decent based learning as compared to multi-agent being used in the previous work.

### 6.1.1 Main Contributions

Motivated by these earlier works, in this work, we have used reinforcement learning (RL) based method for performing the load balancing in a hybrid LiFi WiFi network. It has been shown that RL based load balancing provides improved average network throughput, user satisfaction, fairness and outage performance. The system is analyzed under two different user behaviour.

The main contributions of this work are summarized as follows:

- We have proposed RL based dynamic load balancing for hybrid LiFi WiFi network. The reward function of RL has been designed not only to maximize the long-term average network throughput but also to improve both users satisfaction and fairness.
- The results are compared against the state-of-the-art signal strength strategy (SSS), an iterative optimization method and exhaustive search, explained in Section 7.3.2. The results are presented in terms of computational complexity, average network throughput, user satisfaction, fairness and capacity outage probability.

- Two different scenarios with different user behavior models have been considered to demonstrate the adaptability of the proposed RL method, they are referred as random waypoint (RWP) and hotspot random waypoint (HRWP), explained in Section 6.2.1.

## 6.2 System Model

In this chapter, a multi-user HLWN as described in Section 5.2 is considered for indoor communication. The users are assumed to be distributed across the room and they follow random way point and hotspot random waypoint mobility model, explained in Section 6.2.1. Moreover, it is assumed that each user can connect to a single AP at a time (i.e., either a LiFi AP or the WiFi AP). In order to support multiple users connection to single AP, TDMA is considered in this work and it is assumed that all the users connected to AP $\alpha$ will share resources equally. Fig. 6.1 shows the schematic diagram of considered HLWN.

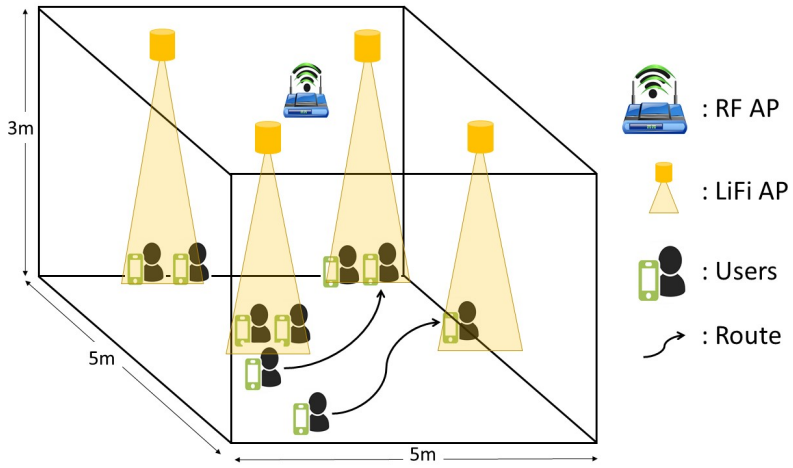


Figure 6.1: Schematic diagram of a HLWN.

### 6.2.1 Mobility Models

In general, most of the studies consider RWP model for mobility. It is a simple model in which a user selects a random destination and moves towards that destination at a constant speed. After reaching the destination, user picks up a new destination and starts moving in that direction and this process continues. However, it is also interesting to consider that inside a room, there are hotspots, where the users would gather with high probability. For example, users may gather under the LEDs to have better illumination level.

In [129], authors have introduced a modified random waypoint model, that allows to create hotspots by modifying the distribution of destination points. The distribution of the destination

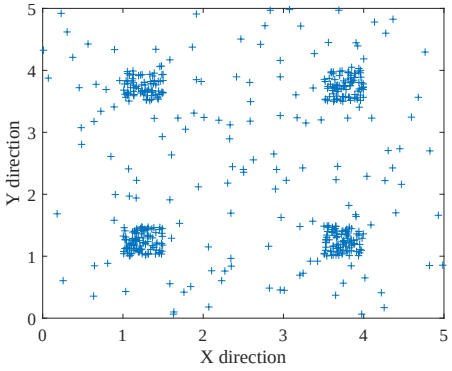


Figure 6.2: Distribution pattern of 100 nodes inside room for modified random waypoint model

points $(x_d, y_d)$ is given by [129]:

$$f(x_d,y_d) = \frac{1}{A_{\text{room}} + (\xi_i - 1)A_a}\Big[(u(x_d + x_m) - u(x_d - x_m)) \\ (u(y_d + y_m) - u(y_d - y_m)) + (\xi_i - 1) \\ (u(x_d - x_{a,max}) - u(x_d - x_{a,min})) \\ (u(y_d - y_{a,max}) - u(y_d - y_{a,min}))\Big] \tag{6.1}$$

where $A_{\text{room}}$ is the area of the room, $A_a$ is the area of the hotspot and $\xi_i$ is the intensity. The room is defined as $-x_m \leq x \leq x_m$ and $-y_m \leq y \leq y_m$ and hotspot is defined by $x_{a,min} \leq x \leq x_{a,max}$ and $y_{a,min} \leq y \leq y_{a,max}$,

In our work, we have considered four hotspots located around four LEDs in the room with $\xi_i = 200$ and $A_a = 0.25\text{m}^2$. Additionally, a wait time has been introduced i.e., once a user reaches to a hotspot, it will wait for some time at that particular location. Afterwards, the user will select a new destination and the process will continue. This particular mobility model will be referred as for hotspot random waypoint model (HRWP) in this work. Fig. 6.2, shows the distribution of 100 nodes inside the room with above mentioned specifications for HRWP model.

### 6.2.2 Performance Metrics

In this work, the performance is compared based on four metrics namely, average network throughput, user satisfaction, fairness and outage probability.

- The **user's satisfaction** $S_{\mu,\alpha}$ is defined as the ratio of data rate achieved by the user to the data rate required by that user, it can be expressed as [9]:

$$S_{\mu,\alpha} = \min\{1, \frac{k_{\mu,\alpha} dr_{\mu,\alpha}}{R_\mu}\} \tag{6.2}$$

  where $R_\mu$ is the requested data rate by user $\mu$. The maximum value of user satisfaction is 1, which implies that the user has achieved its requested data rate.

- For fairness, **Jain's fairness index** is used. Jain's index can be computed as [130]:

$$\eta_f = \frac{\left(\sum\limits_U S_{\mu,\alpha}\right)^2}{N_U \sum\limits_U (S_{\mu,\alpha})^2} \tag{6.3}$$

  where $N_\mathrm{U}$ is the number of users.

- The **rate outage probability** can be defined as [9]:

$$\Phi = \mathrm{Prob}(k_{\mu,\alpha} dr_{\mu,\alpha} < R_o) \tag{6.4}$$

  where $R_o$ is the average required value of throughput.

## 6.3 Proposed RL Based Load balancing

RL is a promising machine learning approach, where an agent continuously interacts with the environment in order to observe the state of the environment and to take actions based on these observations, as shown in Fig. 6.3. The ultimate goal of RL agent is to determine a stochastic policy, which maps states to a probability distribution over actions, in order to maximize the cumulative reward. RL can be viewed as an stochastically optimized solution for Markov Decision Processes (MDPs), when the MDP is not known. In the standard formulation of MDP, at time step $t \geq 0$, an agent is in state $s_t \in \mathbb{S}$, takes an action $a_t \in \mathbb{A}$, receives an instant reward $r_t = r(s_t, a_t) \in \mathbb{R}$ and transits to a next state $s_{t+1} \sim P(\cdot|s_t, a_t) \in \mathbb{S}$. $\pi : S \to P(A)$ is the policy, where $P(A)$ is the set of distributions over the action space $A$ [131]. The discounted cumulative reward under policy $\pi$ is [132]:

$$\eta(\pi) = \mathbb{E}_{s_0, a_0, \ldots}\left[\sum_{t=0}^{\infty} \gamma^t r(s_t, a_t)\right],$$
$$s_0 \sim \rho_0(s_0), a_t \sim \pi(a_t|s_t), s_{t+1} \sim P(s_{t+1}|s_t, a_t)$$

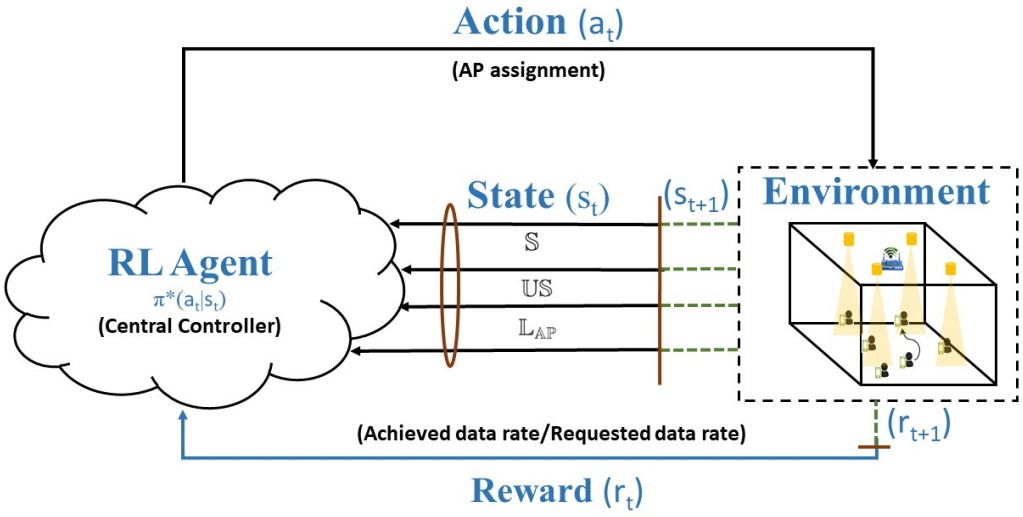


Figure 6.3: RL for a HLWN.

where $\gamma \in (0,1)$ is the discount factor where lower values of $\gamma$ means more emphasis on immediate rewards. The goal of RL is to find an optimal policy, $\pi^*$, which achieves the maximum $\eta(\pi)$ i.e.,

$$\pi^* = \underset{\pi}{\operatorname{argmax}}(\eta(\pi))$$

We have formulated the given HLWN AP assignment problem as an infinite-horizon discounted MDP defined by $(S, A, P, r, \rho_0, \gamma)$ where

- $\mathbb{S}$ is the set of continuous states, which includes SINR for all the users from all the APs represented by a matrix $\mathbb{SI}$, the current load on each AP ($\mathbb{L}_{\mathbb{AP}}$) i.e., number of users connected to a particular AP out of total number of users, and user satisfaction represented as $\mathbb{US}$. The dimensions of $\mathbb{SI}$ is $[N_{\mathrm{U}} \times N_{\mathrm{AP}}]$, dimensions of ($\mathbb{L}_{\mathbb{AP}}$) is $[N_{\mathrm{AP}}]$ and dimensions of $\mathbb{US}$ is $[N_{\mathrm{U}}]$. Therefore, dimension of the observation space is $[N_{\mathrm{U}} + N_{\mathrm{AP}} + N_{\mathrm{U}} \times N_{\mathrm{AP}}]$.

- $\mathbb{A}$ is a finite set of discrete actions, which is AP assignment, therefore, the dimension for discrete action space is $[N_U]$.

- $r : S \times A \to \mathbb{R}$ is the reward function, which is $(\frac{dr_{\mu,\alpha} k_{\mu,\alpha}}{R_\mu})$, where $dr_{\mu,\alpha} k_{\mu,\alpha}$ is the achievable data-rate between AP $\alpha$ and user $\mu$, which is given by (5.3), (5.7) and (5.11). The reward function is carefully designed to take into account both the throughput and user satisfaction.

- The discount factor $\gamma$ is set to 0.9, $P : S \times A \times S \to \mathbb{R}$ is the transition probability distribution, $\rho_0 : S \to \mathbb{R}$ is the distribution of the initial state $s_0$.

In this work we have used a multi-layer perceptron (MLP) as policy network with parameters $\theta$, for the task of access point assignment. Thus, the policy $\pi$ can be written as $\pi(a_t|s_t;\theta)$. The state-action value function $Q_\pi$, value function $V_\pi$, and the advantage function $A_\pi$ are defined as [132]:

$$Q_\pi(s_t,a_t) = \mathbb{E}_{s_{t+1},a_{t+1},\ldots}\left[\sum_{l=0}^{\infty}\gamma^l r(s_{t+l},a_{t+l})\right],$$
$$V_\pi(s_t) = \mathbb{E}_{a_t,s_{t+1},\ldots}\left[\sum_{l=0}^{\infty}\gamma^l r(s_{t+l},a_{t+l})\right],$$
$$A_\pi(s,a) = Q_\pi(s,a) - V_\pi(s),$$

where $a_t \sim \pi(a_t|s_t;\theta), s_{t+1} \sim P(s_{t+1}|s_t,a_t)$ for $t \geq 0$.

The training process involves the optimization of policy parameter $\theta$ of the MLP in order to maximize the expected discounted return. For this purpose, Trust Region Policy Optimization (TRPO) is used, which is a scalable algorithm for optimizing policies by using gradient descent [132]. The policy gradient methods are model free and provides better training stability than value iteration methods [133]. Moreover, TRPO provides guaranteed monotonic improvements under certain assumptions [132], which means the policy update in each TRPO iteration creates a better policy. TRPO methods directly learn the policy $\pi(a|s;\theta)$ using gradient descent, while constraining the update size of $\theta$ at each step. In particular, TRPO enforces this by introducing a KL divergence constraint on the size of update between the old and new policy at each iteration. The optimization problem in TRPO can be written as:

$$\underset{\theta}{\text{maximize}}\, \mathbb{E}_{s\sim\rho_{\theta_{old}},a\sim q}\left[\frac{\pi_\theta(a|s)}{q(a|s)}Q_{\theta_{old}}(s,a)\right] \tag{6.5}$$
$$\text{subject to } \mathbb{E}_{s\sim\rho_{\theta_{old}}}\left[D_{\mathrm{KL}}(\pi_{\theta_{old}}(.|s)||\pi_\theta(.|s))\right] \leq \delta$$

where $\delta$ is a tunable parameter.

The exact steps required to determine the optimal policy $\pi^*_\theta(a_t|s_t)$ are explained in Algorithm 2. At the end of the training process the optimal policy $\pi^*(a|s;\theta)$ is obtained, as shown in Fig. 6.4. This policy can be used in the real time in order to predict appropriate AP assignment, calculate reward and next state, as explained in Algorithm 3. The computational complexity of such system is usually smaller as compared to optimization based method. In the next sub section we have defined the optimzation problem with an objective function same as the reward function of the RL.

**Algorithm 2** :TRPO Algorithim to find optimal policy [132]

**Input**: Initial policy parameter, $\theta_0$

**Output**: Optimal policy, $\pi^*_\theta(a_t|s_t)$

1: **for** k=0,1,2,... **do**
2: Run policy $\pi_\theta$ to collect the set of trajectories
3: Estimate the advantage function $A_{\pi k}$
4: Compute policy gradient $g_k$ and KL-divergence Hessian-vector product function $f(v) = H_k v$
5: Use conjugate gradient to calculate $x_k \approx {H_k}^{-1} {g_k}^{-1}$
6: Estimate step update $\Delta_k \approx \sqrt{\frac{2\delta}{x_k^T H_k x_k}} x_k$
7: Update step $\theta_{k+1}$, using line search.
$\theta_{k+1} = \theta_k + \alpha^k \Delta_k$
8: **end for**

**Algorithm 3** : Algorithm for load balancing using RL [9]

**Input**: Current state of HLWN, $s_t$ and optimal policy $\pi^*_\theta(a_t|s_t)$

**Output**: Reward $r_{t+1}$ and state $s_{t+1}$

Use $\pi^*_\theta(a_t|s_t)$ for given $s_t$, in order to predict $a_t$.
Update the AP assignment in the environment based on $a_t$.
Based on new AP assignment calculate reward $r_{t+1}$ and new state $s_{t+1}$.
**return** $r_{t+1}$ and $s_{t+1}$

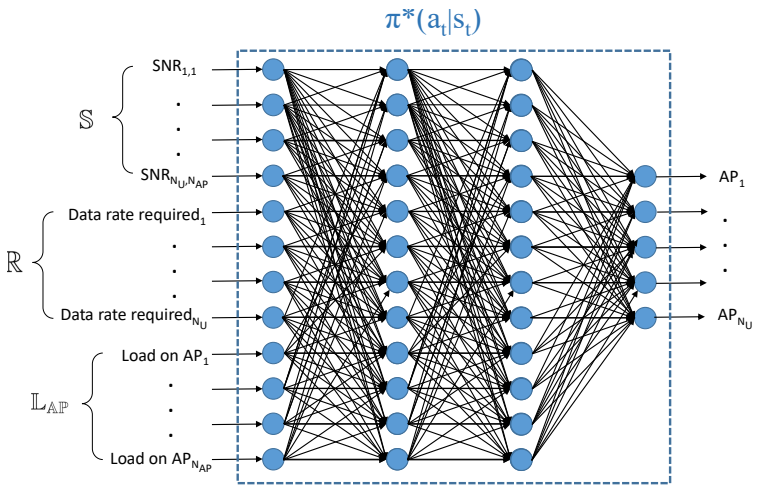


Figure 6.4: Optimum multi-layer perceptron (MLP) policy structure

### 6.3.1 Training Performance and Convergence of RL

In this work, we have used TRPO which imposes a trust region constraint on the policy to stabilize learning. For the sake of simplicity, we have reported the training results for 5 users, similar trend can be observed for 10 users. Fig. 6.5 shows the training performance of RL algorithm in terms of average reward for different discount factor, $\gamma$.

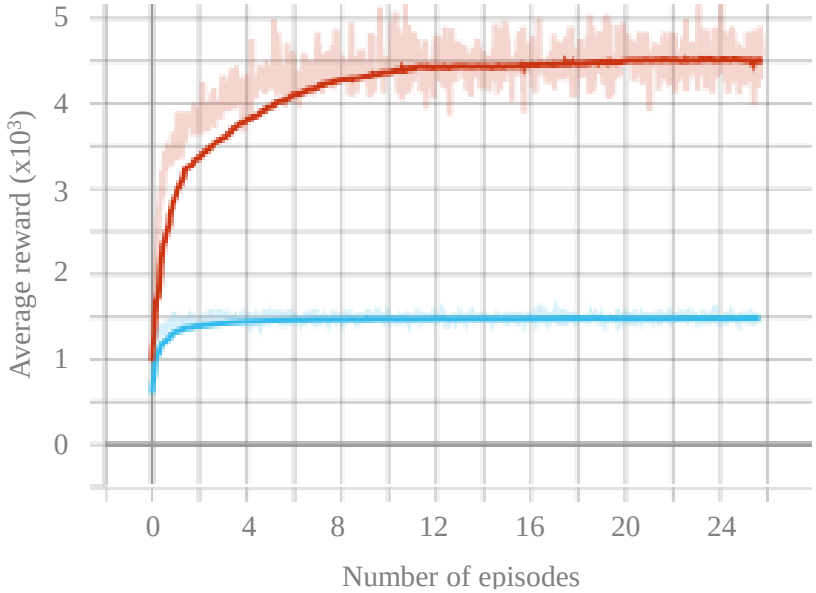


Figure 6.5: Training performance and convergence of RL in terms of average reward w.r.t number of episodes for $\gamma = 0.9$ (red) and $\gamma = 0.7$ (blue).

It can be seen that the average reward of the algorithm converges after a certain number of episodes for both $\gamma$ values. However, there is significant difference in value of average rewards obtained by the algorithm for different $\gamma$ values. It can be observed that $\gamma = 0.9$ achieves average reward of around 3 times of average reward achieved by $\gamma = 0.7$. Therefore, $\gamma = 0.9$ has been chosen for simulation. However, the convergence of the algorithm for $\gamma = 0.9$ takes more time. In future work, we aim to include the concept of knowledge transfer in our algorithm to improve its convergence speed. TRPO being model-free algorithms, directly learns the optimal policy without estimating the model (transition and reward functions) of the environment. Therefore, TRPO requires relatively little tuning of hyperparameters; however, it suffers from higher sample complexity [134]. TRPO is an on-policy method, which means it explores by sampling actions according to the latest version of its stochastic policy. The exploration depends on both initial conditions and the training procedure. There are various methods proposed in literature to deal with the sample complexity of TRPO [135–137]; however, as this work is mainly focused on RL based load balancing for hybrid LiFi WiFi network, for the sake of simplicity, we have considered the simplest form of TRPO in this

work. In future work, we aim to include the concept of knowledge transfer in our algorithm to improve its performance and convergence speed.

## 6.4 Results and Discussion

We have considered a 5 m $\times$ 5 m $\times$ 3 m indoor space which is entirely covered by a WiFi AP, and partially covered by 4 Li-Fi APs, as shown in Fig. 6.1. It is assumed that all the optical attocells reuse the same bandwidth so there exists interference, which has been included in the LiFi SINR calculation as given in equation (5.2). The users are assumed to be uniformly distributed across the room, and two different mobility models are considered, namely, RWP and HRWP. The parameters for LiFi and WiFi channels are stated in Table 6.1 and 6.2, respectively [117, 125].

Table 6.1: LiFi channel parameters

| **Channel Parameter** | **Symbol** | **Value** |
|---|---|---|
| Height difference between the user and AP | $h$ | 2 m |
| Area of PD | $A_{\text{PD}}$ | 1 $\text{cm}^2$ |
| The gain of opitcal filter | $g_{\text{f}}$ | 1 |
| Half intensity radiation angle | $\Phi_{1/2}$ | $60^\circ$ |
| Field of View (FOV) of PD | $\Psi_c$ | $60^\circ$ |
| Responsivity | $R_{\text{PD}}$ | 0.53 A/W |
| Reflection coefficient | $\rho$ | 0.8 |
| Transmit opitcal power per LiFi AP | $P_{\text{opt}}$ | 3 Watt |
| Bandwidth per LiFi AP | $B_{\text{LiFi}}$ | 40 MHz |
| PSD of noise in LiFi | $N_{\text{LiFi}}$ | $10^{-21}$ $A^2$/Hz |

Table 6.2: WiFi channel parameters

| **Channel Parameter** | **Symbol** | **Value** |
|---|---|---|
| Breakpoint distance | $d_{\text{BP}}$ | 2.5 m |
| Shadowing loss | $X_{\text{SF}}$ | 3 dB |
| Central carrier frequency | $f_{\text{c}}$ | 2.4 GHz |
| WiFi AP's transmit Power | $P_{\text{WiFi}}$ | 20 dBm |
| WiFi AP's bandwidth | $B_{\text{WiFi}}$ | 20 MHz |
| PSD of noise in WiFi | $N_{\text{WiFi}}$ | -174 dBm/Hz |

In order to obtain the results a simulation scenario as illustrated in Fig. 6.1 has been coded in MATLAB. Further, We have considered the data rate requested by the users defined by Poisson distribution process with parameter $R_o$, which is set to 50 Mbps for simulation. The

performance of the proposed RL method has been compared against exhaustive optimization, iterative optimization and signal strength methods, explained in Section 5.3.1 and 5.3.2. The SSS method selects the AP that offers highest signal strength. Unlike homogeneous network, in a hybrid LiFi and WiFi network since the bandwidth and receiver noise differs for LiFi and WiFi, therefore, received signal strength does not fully represent the quality of channel. Hence, SNR is used as decision metric for SSS method. Further, exhaustive optimization have been considered as the performance upper bound at the cost of higher complexity. The Table 6.3 summarises the system parameters.

Table 6.3: System parameters

| **System Parameter** | **Value** |
|---|---|
| Room dimension | $5 \times 5 \times 3$ m$^3$ |
| Number of APs | 4 LiFi + 1 WiFi |
| WiFi AP location | (2.5 m, 2.5 m) |
| LiFi AP locations | (2.5 $\pm$1.25 m,2.5 $\pm$1.25 m) |
| Mobility model | RWP, HRWP |
| Hotspot intensity, $\xi_i$ | 200 |
| Hotspot area, $A_a$ | 0.25 m$^2$ |
| User speed | 1 m/s |
| RWP Pause time | 0 s |
| HRWP Pause time | 5 s |
| Requested data rate, $R_\mu$ | Poisson with 50 Mbps |
| Gym environment | LiFi WiFi network |
| policy | MLP, 2 layers of 64 |
| max KL divergence, $\delta$ | 0.01 |
| Discount factor, $\gamma$ | 0.9 |
| Episode length, E | 1000 |

### 6.4.1 Complexity Analysis

The SSS method simply selects the AP with highest SNR value out of total APs ($N_{\mathrm{AP}}$). Therefore, its complexity is $\mathrm{O}(N_{\mathrm{AP}}N_{\mathrm{U}})$ [117]. The optimization method based on exhaustive search is computationally expensive as it searches over all possible connections between users and APs, therefore, the complexity is $\mathrm{O}((N_{\mathrm{AP}})^{N_{\mathrm{U}}})$. The complexity of optimization problem based on iterative methods depends on number of iterations $I$ that it takes to converge. Its complexity can be estimated as $\mathrm{O}(N_{\mathrm{U}}N_{\mathrm{AP}}I)$ [119]. The computational complexity of training phase of RL depends upon the number of states ($n$) in the MDP and it is given by $\mathrm{O}(n)$, however, this is just one time training cost. During the real time the complexity of RL algorithm depends on the optimal policy which is represented in form of MLP, the complexity depends upon

the dimensions of observation and action space which in given in Section 6.3, therefore, the complexity for RL is $O(N_U^2 N_{AP} + N_U^2 + N_U N_{AP})$.

The complexity of SSS increases linearly with number of users, whereas for exhaustive optimization the complexity increases exponential with number of user. The complexity for iterative method is dependent on $I$ and in case of RL the complexity has a quadratic relation with number of users. It is observed from Table 6.4 that the real time complexity of RL is much smaller as compared to exhaustive and iterative optimization. For better understanding, we have plotted the computational complexity of these methods for different number of users, assuming $I = 30$ [119], shown in Fig. 6.6. It can be observed from the graph that the complexity of RL is lower than exhaustive and iterative method.

Table 6.4: Computational Complexity [9]

| **Scheme** | Complexity |
|---|---|
| SSS | $O(N_{AP} N_U)$ |
| Iterative | $O(N_U N_{AP} I)$ |
| Exhaustive | $O((N_{AP})^{N_u})$ |
| RL | $O(N_U^2 N_{AP} + N_U^2 + N_U N_{AP})$ |

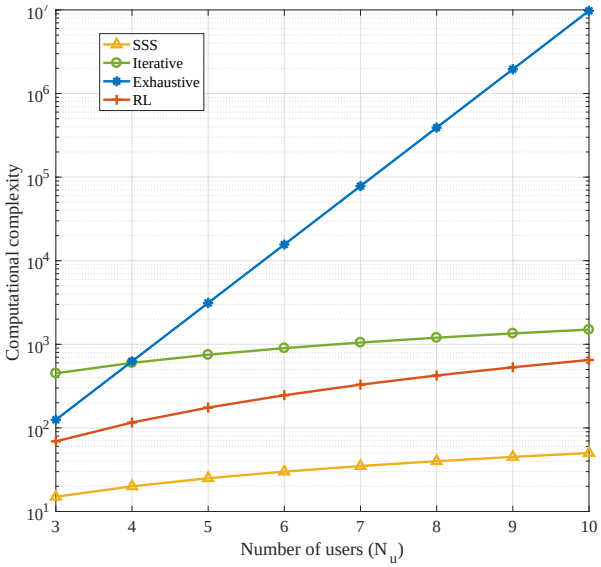


Figure 6.6: Computational Complexity

## 6.4.2 Effect of Number of Users

The average network throughput for different number of users under various load balancing schemes are stated in Table 6.5. For 5 users, the iterative optimization based AP assignment

Table 6.5: Average network throughput (Mbps) for different number of users

| $N_U$ | SSS | Iterative | Exhaustive | RL |
|---|---|---|---|---|
| 5 | 116.23 | 174.04 | 239.90 | 218.81 |
| 10 | 73.12 | 98.72 | 138.41 | 110.69 |

provides 49.74% increment in average network throughput over SSS, whereas the RL and exhaustive optimization provide an improvement of 88.26% and 106.41% over SSS in average network throughput respectively.

As the number of users are increased to 10, RL and exhaustive search provides 51.37% and 89.29% improvement in average network throughput over SSS, respectively. The RL is able to provide significant improvement over SSS in throughput as compared to iterative algorithm for which the improvement in average network throughput over SSS is limited to 34.24 %. It is important to note that as the number of users increases, the network performance saturates, because of this the gain achieved by different load balancing methods is restricted.

The values of Jain's fairness index $\eta_f$ for different number of users under various load balancing schemes are calculated using equation 6.3, they are tabulated in Table 6.6. For 5 users, all the schemes are able to achieve the fairness value very close to 1. However, for 10 users, SSS fairness is limited to 0.96, whereas both RL and optimization achieve a fairness of 0.97. The fairness index for exhaustive optimization was highest i.e., 0.97. Since the Jain's fairness index and average network throughput provide an average overview of the network performance. In order to provide a better insight on the performance of these schemes, the CCDF of user satisfaction and outage probability for particular throughput are provided.

Table 6.6: Fairness for different number of users

| $N_U$ | SSS | Iterative | Exhaustive | RL |
|---|---|---|---|---|
| 5 | 0.9998 | 0.9999 | 1.0000 | 1.0000 |
| 10 | 0.9568 | 0.9743 | 0.9872 | 0.9727 |

The user satisfaction can be calculate using equation 6.2, afterwards the CCDF of user satisfaction can be calculated using MATLAB code. Fig. 6.7 shows the CCDF of user satisfaction for different number of users under four different load balancing schemes. The value of satisfaction is calculated using Eq. 6.2. From the results, it can be observed that SSS based scheme performs worst in terms of user satisfaction, less than 40% and 25% of the users are completely satisfied for SSS based AP assignment method for 5 and 10 users, respectively. For iterative optimization, it is around 85% when there are 5 users but this value drops drastically to far less than 30% when the number of users are increased to 10. For exhaustive optimization and RL around 98% and 96% of users achieve complete satisfaction when there are 5 users, but as the number of users increases to 10, this value drops to around 45% and 40% respectively.

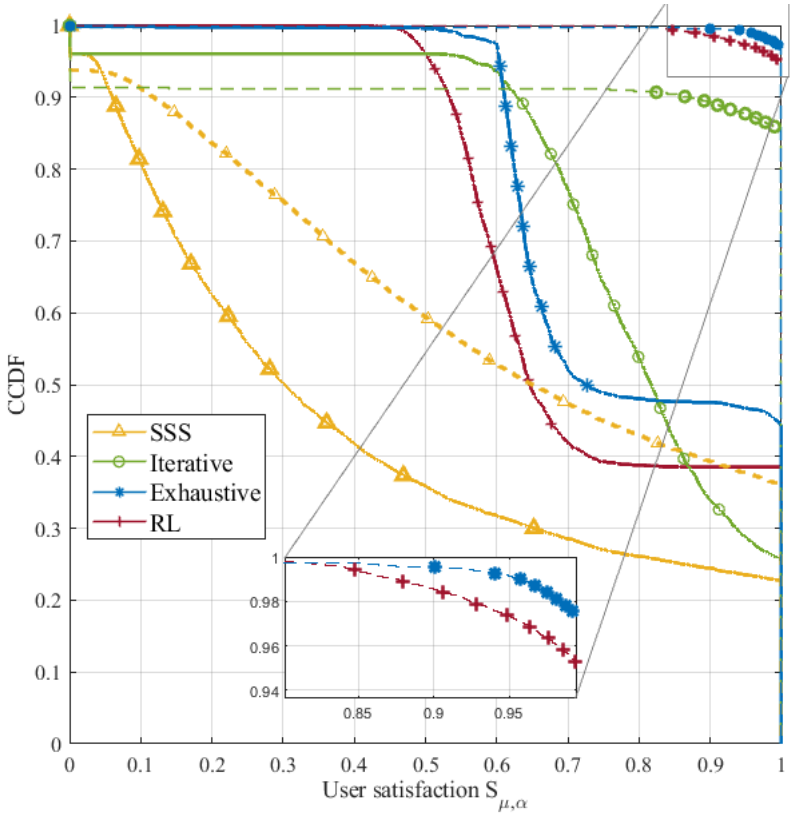


Figure 6.7: User Satisfaction: $N_u$=5 (dashed lines) and $N_u$=10 (solid lines)

Therefore, it can be observed that highest percentage of full user satisfaction is achieved by exhaustive search method followed by RL, which provides close enough performance. Moreover, an increase in number of users reduces the user satisfaction for all schemes.

The outage probability for a threshold throughput of $R_o$ can be calculated from the simulation results using the equation (6.4). Fig. 6.8 illustrates the outage probability for a threshold throughput of $R_o$. It can be observed that for 5 users, if a system allows 10% of the users to be in outage in terms of capacity, than the average network throughput can be around 210 and 180 Mbps for exhaustive search and RL respectively. In case of iterative algorithm this value is limited to less than 100 Mbps, where as for SSS it is around 40 Mbps.It can be observed that SSS performs worst, followed by iterative optimization. For larger outage probabilities, beyond 0.6, the performance of RL and exhaustive optimization converges. Further, as the number of users increases from 5 to 10, for a particular outage probability for the throughput value decreases significantly. Overall, exhaustive search provides highest possible throughput for a a particular outage probability, followed by RL, which provides almost similar performance at higher outage probability. Increase in the number of users degrades the performance for all schemes, but mostly RL performs close to exhaustive search.

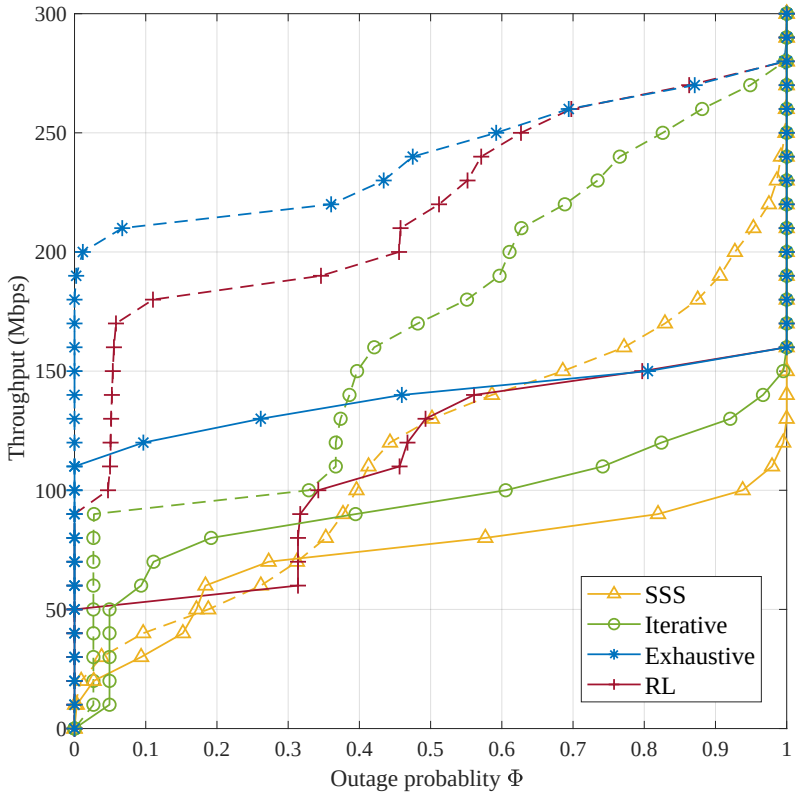


Figure 6.8: Outage probability: $N_u$=5 (dashed lines) and $N_u$=10 (solid lines)

### 6.4.3 Effect of Mobility Models

In this work, we have also considered different user behaviours such as HRWP mobility model, which has four attraction points located around the four LEDs. Table 6.7 summarizes the average network throughput for 5 users under two different mobility models.

Table 6.7: Average Network throughput (Mbps) for different mobility models

| $N_U$ | SSS | Iterative | Exhaustive | RL |
|---|---|---|---|---|
| 5 (RWP) | 116.23 | 174.04 | 239.90 | 218.81 |
| 5 (HRWP) | 122.23 | 197.28 | 267.86 | 214.85 |

It is interesting to note that the pattern of performance remained the same for both mobility models. The exhaustive optimization provides the highest improvement in terms of average network throughput over SSS method, followed by RL and iterative optimization. The Jain's fairness index for 5 users under different mobility models are tabulated in Table 6.8. It can be observed that all the schemes are able to achieve full fairness ($\eta_f = 1$) for 5 users under both mobility models.

Table 6.8: Fairness for different mobility models

| $N_U$ | SSS | Iterative | Exhaustive | RL |
|---|---|---|---|---|
| 5 (RWP) | 0.9998 | 0.9999 | 1.0000 | 1.0000 |
| 5 (HRWP) | 0.9990 | 0.9968 | 1.0000 | 1.0000 |

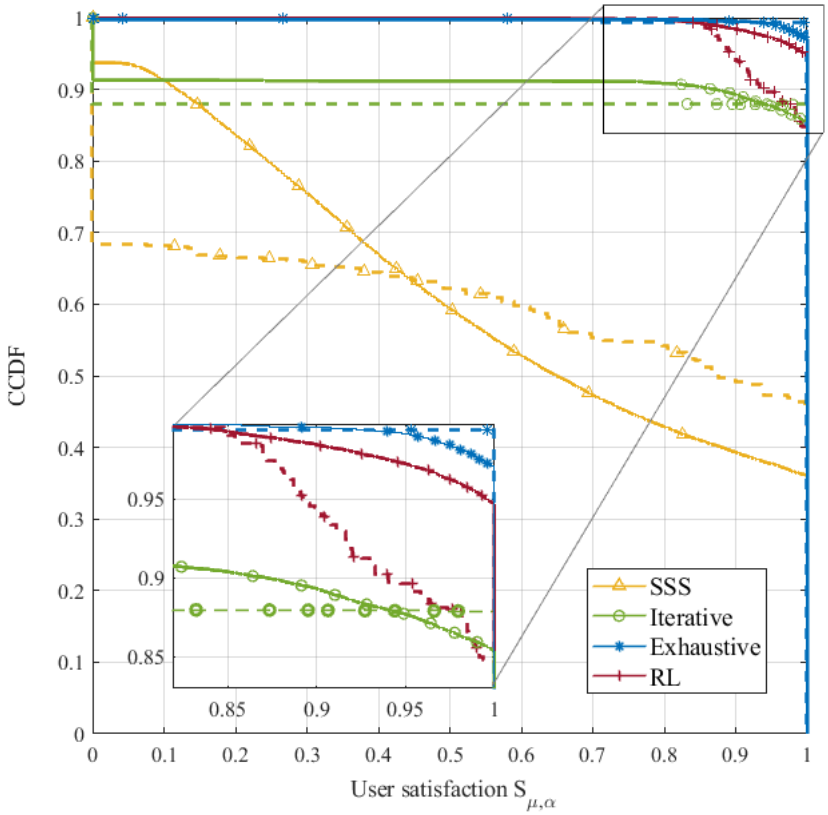


Figure 6.9: User Satisfaction (5 users) : with RWP (soild lines) and HRWP (dashed lines)

Fig. 6.9 shows the CCDF of user satisfaction for 5 users under different mobility models. It can be observed that the user satisfaction changes significantly for the two mobility models. For SSS, in case of HRWP around 45% of the users are able to achieve full satisfaction whereas in case of simple RWP, it is only limited to 35%. Further, exhaustive search provides slight improvement in user satisfaction for HRWP. At the same time, RL provides performance matching to iterative optimization method for HRWP. Further, RL ensures 0.85 user satisfaction for all users for both mobility models, whereas iterative optimzation scheme is only able to ensure the user satisfaction for 90% of the users, which means that at least 10% of users never achieves the desired user satisfaction for iterative algorithm. Moreover, SSS can ensure the user satisfaction only for 70% of the users in HRWP model.

Fig. 6.10 illustrates the outage probability of a particular throughput $R_o$ for 5 users under two different mobility models. It can be observed that in case of HRWP the achievable throughput

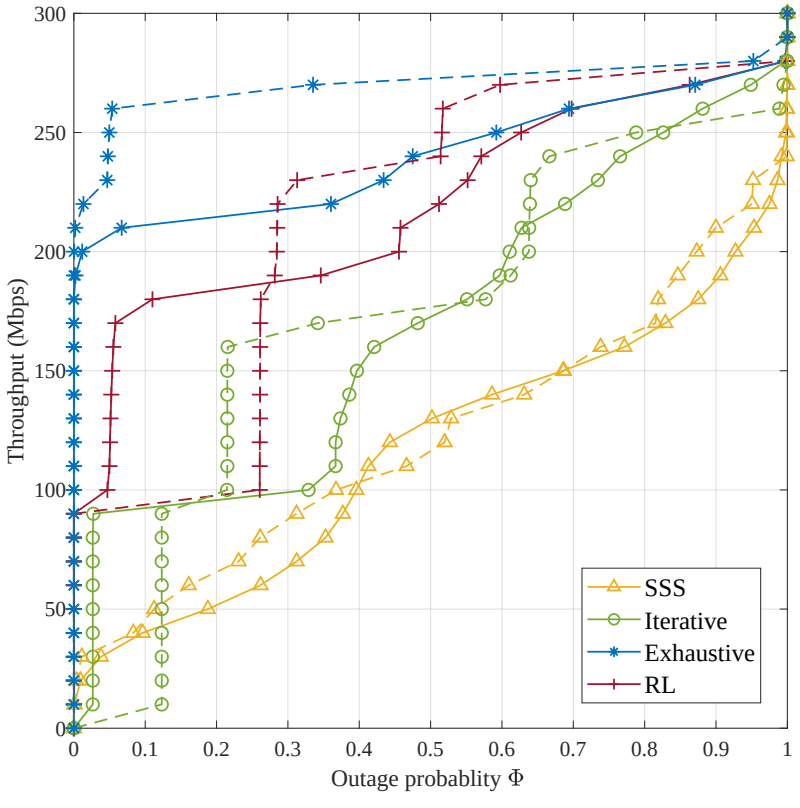


Figure 6.10: Outage probability (5 Users) : with RWP (soild lines) and HRWP (dashed lines)

with certain outage probability increases for exhaustive search. For SSS, the performance remained almost same with RWP and HRWP. Iterative algorithm and RL exhibits similar behaviour for the two mobility models, for smaller values of outage probability, they support higher throughput in RWP models, but for larger values of outage probability, they support higher throughput in HRWP models. Overall, the trend of performance for four methods remained same for both the mobility models and it is shown that RL provides robustness against different user behaviour.

## 6.5 Summary

In this chapter, an RL based dynamic load balancing scheme has been considered for HLWNs. The reward function of RL was carefully crafted to increase the average system throughput while ensuring the required QoS. The RL was trained to determine the optimal policy, by using TRPO algorithm. Afterwards, the optimal policy was exploited to determine the appropriate AP assignment for the given state. Based on simulation results and complexity analysis, it is shown that the proposed method achieves a significantly better performance at lower run-time complexity compared to the conventional SSS scheme and the iterative algorithm.

The exhaustive optimization provided the best performance at the cost of high computational complexity which is impractical for real life scenarios. However, it is shown that the RL scheme can achieve a close performance as exhaustive search with a lower complexity. Furthermore, the performance trends of RL compared to other schemes remained unchanged for different mobility models, which proves the robustness of the proposed scheme

Chapter 7

# Load Balancing in Link Aggregation Enabled HLWNs

In chapter 6, it was assumed that a HLWN user can either connect to a LiFi or WiFi AP at a time, however in a HLWN, it is possible for a user to connect to both LiFi and WiFi AP simultaneously. In this chapter, the performance of an link aggregation enabled HLWN is investigated and compared against HLWN that allows connection with single AP at a time. Further, a RL based HLWN LB has been proposed for link aggregation enabled HLWN. This chapter evaluates the performance of RL based HLWN LB in the presence of LiFi CCI, orientation based RWP, and handover. Furthermore, the concept from domain knowledge are also included in RL based LB to further reduce its complexity. The brief introduction and contributions related to the above mentioned system are given in Section 7.1 followed by Section 7.2 which provides a brief overview of the HLWN system. Section 7.3 describes the LB methods for link aggregation enabled HLWN LB. The simulation results are presented in Section 7.4. Finally, Section 7.5 concludes the chapter.

## 7.1 Introduction

In a HLWN, it is possible for a user to connect to both LiFi and WiFi AP simultaneously. A HLWN where user can aggregate data from both LiFi and WiFi link is known as link aggregation enabled HLWNs. There exists limited literature on the aggregation of LiFi WiFi links in a HLWN [29, 126, 138–140]. In [126], authors proposed the concept of responsive and anticipatory association, the associations were established based on users' geo-locations and queue backlog states. Their objective was to find the optimal trade-off between the average system queue backlog and the average per-user throughput. In [29, 138], authors have implemented channel aggregation for HLWN, and demonstrated proof-of-concept by

using state-of-the-art LiFi and WiFi frontends. Both of these works focused on practical demonstration and employed AP assignment based on the received signal strength and ignored the effect of AP overloading. In [139], authors have proposed an online two-timescale power allocation algorithm for users with multi-homing capability that allows the users to aggregate the resources from both RF and LiFi APs. However, they have not considered the effect of interference between LiFi APs. Further, they implemented Q-learning based methods and compared their results only with stand-alone LiFi and WiFi AP, whereas in the current work policy-gradient based method has been implemented. In [140], the authors utilized Lyapunov optimization function for determining the optimal scheduling based on queue lengths for achieving the desired throughput. The authors have practically validated the performance of proposed protocol by implementing it on a real-life prototype. Their focus was on queue length-based scheduling algorithm to achieve optimal throughput. On the other hand, the current proposed work focuses on optimal AP assignment for a higher average network throughput while ensuring a particular user satisfaction. There are various research gaps in the above-mentioned works. Firstly, these works did not compare their results with two benchmarks RSS and exhaustive search method which has been done in the current work. Secondly, the current work also compares the performance of the system without and with link aggregation which was missing in most of the previous studies. Thirdly, the current work considers a more realistic scenario with effect of handover overhead, interference between neighbouring LiFi APs, user mobility and receiver device orientation. Additionally, in the current work, three different reward functions for different objectives have been explored, whereas most of the existing research works have explored only single reward function. Finally, in order to reduce the complexity of RL algorithm the concept of domain knowledge has been exploited in the current work. In our previous work [9], we have applied RL for AP assignment in HLWN and reported promising results, but we assumed a simplistic system model. We assumed time-division multiple access, and assumed that a user can connect to single AP, i.e. it can either connect to WiFi AP or LiFi AP at a time. Furthermore, we did not considered the effect of receiver orientation or handover overhead in our previous system model. However, in current work the effect of link aggregation and different reward functions is studied. Further, concept of domain knowledge has been exploited to reduce the complexity of the proposed system. Additionally, in this work, we have considered a more realistic framework for modeling the HLWN with CSMA/CA and handover overhead.

### 7.1.1 Motivation and Main Contributions

Motivated by earlier works to study link aggregation effect on HLWN performance, two different types of receiver, namely, single AP (SAP) and link aggregation (LA) receiver, are

considered in this work. The SAP receiver will allow users to receive data from either a LiFi or WiFi AP, whereas the LA receiver will allow users to receive data simultaneously from both LiFi and WiFi APs. For LA user, it is assumed that the physical and medium access layer of WiFi receiver and LiFi receiver will work independently [29]. Furthermore, in literature, it has been proven that load balancing of HLWN is a non-convex MINLP problem [119, 120] which is mathematically intractable, thus, the conventional optimization algorithms can not find the global optimum solution for this kind of problem. Therefore, to overcome this limitation of the conventional optimization algorithm, we have proposed a centralized RL algorithm to perform LB in a HLWN. The RL algorithm determines its actions based on online-learning from the HLWN environment. Moreover, the effect of different reward functions on the proposed algorithm's performance is also studied in this work. The concepts of domain knowledge have been exploited to reduce the algorithm's computational complexity. It has been shown that RL based LB in a HLWN with an appropriate reward function provides significantly improved performance.

The main contributions of this chapter are summarized as follows:

- Two different types of receivers, namely SAP and LA, have been considered to study the effect of link aggregation on the performance of HLWNs. A user equipped with a SAP receiver device can receive data from a single AP at a time, whereas a LA receiver equipped user can receive data simultaneously from both LiFi and WiFi APs.

- We have proposed a centralized RL based algorithm for dynamic LB in HLWN, and to prove the generalization of the proposed RL algorithm: three different reward functions have been considered, as explained in 7.3.0.3 and their effect have been investigated on the average sum throughput and user satisfaction.

- A more realistic framework with orientation-based random waypoint (ORWP) mobility model, CSMA/CA-based multi-user access, and handover overhead has been considered in this work.

- Furthermore, the concepts of domain knowledge have been utilized to reduce the observation and action space, which reduces the RL algorithm complexity.

- The proposed RL scheme is compared against the RSS and exhaustive search method, explained in Section 7.3.2. The results are presented in terms of computational complexity, average network throughput, and user satisfaction.

## 7.2 System Model

In this work, a typical office room of $5 \times 5 \times 3$ m$^3$ with multi-user HLWN is considered, as shown in Fig. 7.1. The coverage range of WiFi AP is assumed to be around 10 m, whereas the coverage range of each LiFi AP is limited to few meters. A CC unit is required for efficient utilization of the HLWN [27]. In this work, it is assumed that a CC is connected to both WiFi and LiFi APs through an error-free feedback link which is responsible for making the load balancing decisions. Furthermore, in order to study the effect of link aggregation, two different types of receiver are considered in this work, (1) SAP scheme which allows each user to receive data from a single AP, and (2) LA scheme which allows user to receive data simultaneously from both LiFi and WiFi AP. It is important to note that, although LA receiver, allows the user to simultaneously receive data from both LiFi and WiFi AP, but the CC can still decide to connect a LA user to only a LiFi/WiFi AP in order to avoid unnecessary overloading on a particular AP. Furthermore, the users are assumed to be accessing the high definition (HD) videos from the internet, hence their require data rates are modeled as a Poisson process with the parameter value of 70 Mbps. Moreover, in order to have a more realistic framework, the ORWP mobility model and CSMA/CA [115] based multi-user access have been considered in this work.

In the HLWN, the set of users is denoted by $\mathbb{U} = \{\mu | \mu \in [1, N_{\text{u}}]\}$. The set of LiFi APs is

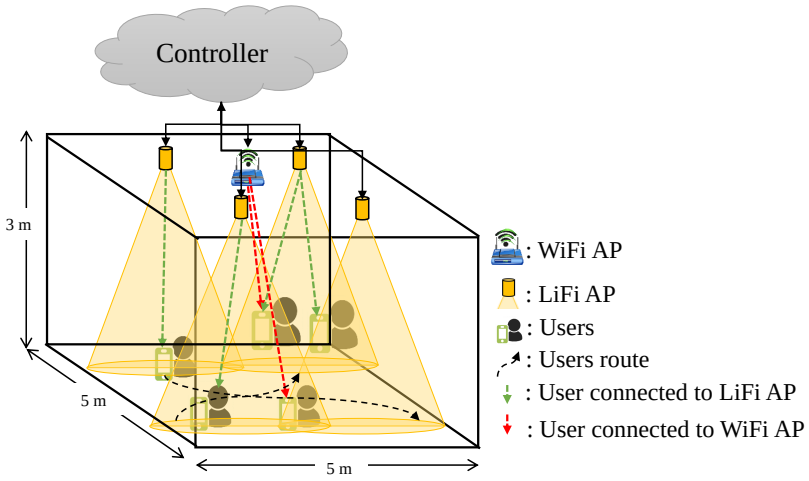


Figure 7.1: Schematic diagram of a link aggregation enabled HLWN.

denoted by $\mathbb{LAP} = \{\alpha | \alpha \in [1, N_{\text{AP-LiFi}}]\}$ and WiFi AP is denoted as $\mathbb{W}$. The complete AP set is given by $\mathbb{AP} = \{\mathbb{W}, \mathbb{LAP}\}$. The total number of APs and users present in the system are represented by $N_{\text{AP}} = N_{\text{AP-LiFi}} + N_{\text{AP-WiFi}}$ and $N_{\text{u}}$, respectively. The LA user is capable of receiving data from both LiFi and WiFi AP simultaneously, therefore, let $\alpha_1 \in \{0, \mathbb{W}\}$ and $\alpha_2 \in \{0, \mathbb{LAP}\}$ indicate the WiFi and LiFi AP conntected to the LA users. The binary

association variable $g_{\mu,\alpha}$ is defined as:

$$g_{\mu,\alpha} = \begin{cases} 1, & \text{user } \mu \text{ is connected to AP } \alpha \\ 0, & \text{user } \mu \text{ is not connected to AP } \alpha \end{cases} \tag{7.1}$$

The achievable datarate of a user $\mu$ connected to an AP $\alpha$ is represented by $dr_{\mu,\alpha}$. Further, the achievable datarate of a user $\mu$ connected to a WiFi AP $\alpha_1$ is given by $dr_{\mu,\alpha_1}$. Similarly, the achievable datarate of a user $\mu$ connected to a LiFi AP $\alpha_2$ is given by $dr_{\mu,\alpha_2}$. Their values can be calculated using the corresponding equations 5.7 and 5.3.

### 7.2.1 Orientation-based Random Waypoint Mobility Model

Generally, most studies consider RWP model for mobility. In RWP, a user pick a random destination and travels at a constant speed towards that destination. Once the user arrives at the destination, the user selects a new destination and starts moving in that direction at a constant speed and this process continues. However, in case of LiFi users, the receiver device orientation plays a crucial role. Therefore, in this work we have considered Orientation based RWP (ORWP) model which was initially proposed in [141] and developed in [142] and [143]. In fact, the ORWP considers the orientation of receiver device while the users move. A correlated Gaussian random process should be generated for the polar angle during the movement of users. The parameters of the ORWP model are chosen from [141]. The ORWP mobility model has been used for the first time in the hybrid LiFi and WiFi networks in [144] to assess the performance of the hybrid system more realisticly and support dynamic load balancing for mobile users. In this study, we considered pause time in the simulation of ORWP which is ignored in [144]. Users may tend to stop for a while at each destination and then continue their movement. We assume pause time at each destination follow an exponential distribution with a mean value of 10 seconds [143].

### 7.2.2 Handover

During a network handover, an overhead occurs that causes a drop in the average data rate of the user involved in the handover. In order to model this reduction in data rate, handover efficiency was introduced in [119] which is defined as the fraction of overhead time to actual transmission time. However, it is important to note that the exact handover efficiency can not be calculated [144]. Therefore, an average handover efficiency is used to estimate the negative effect of handover on users' data rate.

In a HLWN environment, two types of handover exists, namely, vertical and horizontal handover. When a SAP user moves from LiFi AP to WiFi AP or vice-versa, it is termed as

vertical handover (VHO) and when a user moves from LiFi AP to another LiFi AP, it is termed as horizontal handover (HHO). Assuming that user $\mu$ was previously served by AP $\alpha^{t-1}$ and is now being served by AP $\alpha^{t}$. For SAP user, the estimated handover efficiency can be modelled as [145]:

$$\eta_{\text{SAP}}(t) = \begin{cases} 1, & \alpha^{t} = \alpha^{t-1} \ \forall \ \alpha^{t}, \alpha^{t-1} \in \mathbb{AP} \\ \eta_{0,\text{HHO}}, & \alpha_2^{t} \neq \alpha_2^{t-1} \ \forall \ \alpha_2^{t}, \alpha_2^{t-1} \in \mathbb{LAP} \\ \eta_{0,\text{VHO}}, & \text{otherwise.} \end{cases}$$
$$\forall \ \alpha \in \mathbb{AP} \tag{7.2}$$

where, $\eta_{0,\text{HHO}}$ and $\eta_{0,\text{VHO}}$ denote average handover efficiency for HHO and VHO, respectively. Typically, the HHO require a lower amount of overhead and they occur faster in comparison to the VHO. The reason is that the HHO happen among the same domain using the same wireless technology whereas VHO fall among different technologies, which in this work is between LiFi and WiFi. Thus, a higher value of $\eta_{0,\text{HHO}}$ =0.9 is chosen in comparison to the $\eta_{0,\text{VHO}}$ = 0.6 [144]. However, it may please be noted that the choice of these values does not affect the generality of our proposed algorithm.

On the other hand, a LA user can either connect to both LiFi and WiFi AP, or connect to only one of them, therefore, the modelling of VHO will be different from SAP. In this work, VHO for LA user is modelled as handover from both LiFi and WiFi connection to either LiFi or WiFi and vice-versa. Therefore, the estimated handover efficiency for LA user, can be modelled as [145]:

$$\eta_{\text{LA}}(t) = \begin{cases} 1, & \alpha_1^{t} = \alpha_1^{t-1} \text{ and } \alpha_2^{t} = \alpha_2^{t-1}. \\ \eta_{0,\text{HHO}}, & \alpha_1^{t} = \alpha_1^{t-1} \text{ or } \alpha_2^{t} \neq \alpha_2^{t-1}. \\ \eta_{0,\text{VHO}}, & otherwise \end{cases}$$
$$\forall \ \alpha_1 \in \mathbb{W}, \alpha_2 \in \mathbb{LAP}. \tag{7.3}$$

## 7.3 RL-based Load Balancing Method for LA Enabled HLWN

RL is a popular machine learning approach. An RL agent is capable of providing an optimal solution (policy) without the exact knowledge of the underlying mathematical model. RL agents directly learns its policy based on the interaction with the environment, the communication happens between agent and environment in terms of *action* and *reward*. The ultimate goal of RL agent is to determine a stochastic policy, which maps states to a probability distribution over actions, in order to maximize the cumulative *reward* [9]. RL works based on three vectors, namely, *state, action*, and *reward*. The *state* vector defines the present status of the hybrid LiFi WiFi environment. The *action* vector defines the action of AP assignment taken by the RL agent, after observing the present status of the environment. The *reward* vector defines the reward received by the system after an action is taken by the system. Let $\mathbb{S}$ and $\mathbb{A}$ represent the state and action space, respectively. At a given time step $t \geq 0$, an agent will be in state $s_t \in \mathbb{S}$, it will take an action $a_t \in \mathbb{A}$, and will receives a corresponding instant reward $r_t = r(s_t, a_t) \in \mathbb{R}$ and transits to a next state $s_{t+1}$. The CC trains the learning algorithm in order to obtain its policy $\pi_\theta(a_t|s_t)$ for AP association. This process is repeated and with each iteration, the system keeps moving toward the actions that provides maximum cumulative reward. At the end of the training process the optimal policy $\pi^*(a|s;\theta)$ is obtained, this policy can be used in the real time in order to predict appropriate AP assignment, calculate reward and next state, as explained in algorithm 3 of chapter 6.

In this work, the state, action and reward are formulated as follows:

#### 7.3.0.1 State Space *S*

The *state* vector $\mathbb{S}$ defines the current status of the hybrid LiFi WiFi environment, it provides necessary information to the agent to make its decision. In this work, as we are training the agent to determine the optimal AP assignment strategy, therefore we need to take into account the SNR between the user and various APs, which is define by (5.1) and (5.4). Furthermore, as we are dealing with HLWN which is susceptible to AP overloading, we need to provide the information regarding load on a particular AP to the RL agent. Therefore, *S* is the set of continuous states, which includes:

- SNR between users and APs represented by a matrix $\mathbb{S}\ltimes$
- Current load on each AP i.e., number of users connected to a particular AP represented by $\mathbb{L}_{\mathbb{AP}}$. The dimensions of $\mathbb{L}_{\mathbb{AP}}$ is $[N_{\text{AP}}]$

The dimensions of $\mathbb{S}\ltimes$ depends upon the number of APs considered, conventionally the SNR matrix is considered between all the users and all the APs resulting into $\mathbb{S}\ltimes$ dimension of

$[N_{\mathrm{u}} \times N_{\mathrm{AP}}]$. However, based upon our domain knowledge, we have observed that in a standalone LiFi network, usually 2 APs on average provides a SNR difference of 10 dB. Therefore, instead of including the information about all the APs, it would be more efficient to transmit the SNR information between the user and two highest SNR providing APs to the controller. Therefore, by using this simple domain knowledge (DK) the dimension of the observation space can be reduced from $[N_{\mathrm{AP}} + N_{\mathrm{u}} \times N_{\mathrm{AP}}]$ to $[N_{\mathrm{AP}} + N_{\mathrm{u}} \times (2+1)]$.

#### 7.3.0.2 Action Space A

In this work, $\mathbb{A}$ is a finite set of multi-discrete actions. As we are considering the LA receivers, which allows the users to connect to both LiFi and WiFi AP at the same time. However, sometimes the simultaneous connection might not contribute towards a higher reward, this could happen due to AP overloading. In such cases, the controller can decide to transmit the information to LA user via single link only, therefore, converting LA into SAP receiver. Hence, the action space must have discrete values to indicate the standalone connection with LiFi or WiFi AP and simultaneous connection to both LiFi and WiFi AP as well. The action space for a particular user $\mu$ in our setup, can be defined as $A = \{0,1,2,3,4,5,6,7,8\}$, where,

- $a_t = 0$ indicates the user is connected to WiFi AP,
- $a_t = 1,2,3,4$ indicates that the user is connected to LiFi AP 1,2,3, or 4 respectively
- $a_t = 5,6,7,8$ indicates that user is connected to both WiFi AP and LiFi AP 1, 2, 3 or 4 respectively.

However, as we already discussed that two highest SNR APs are usually sufficient to serve the user demands. Therefore, by using this DK, we can reduce the action space. We can store the IDs of highest SNR providing APs at the user and can reduce the action space to $\mathbb{A} = \{0,1,2,3,4\}$, where

- $a_t = 0$ indicates the user is connected to WiFi AP,
- $a_t = 1,2$ indicates that the user is connected to highest or second highest SNR LiFi AP respectively
- $a_t = 3,4$ indicates that user is connected to both WiFi AP and highest or second highest SNR LiFi AP respectively.

Inclusion of this simple DK, reduces both the action and observation space, which reduces the computational complexity and improve the convergence of the RL algorithm.

#### 7.3.0.3 Reward

In this work, we have used three different reward functions ($R_1, R_2, R_3$) for three different objectives:

- $R_1$ : This reward is designed to maximize the long-term average network throughput. The immediate reward $r_t$, is given as [145]:

$$r_t = \frac{\sum_{\mu \in \mathbb{U}} \sum_{\alpha \in \mathbb{AP}} (t_{\mu,\alpha})}{N_u}, \tag{7.4}$$

  where, $t_{\mu,\alpha}$ is defined as [145]:

$$t_{\mu,\alpha} = \begin{cases} \eta_{\text{SAP}} g_{\mu,\alpha} dr_{\mu,\alpha} k_{\mu,\alpha}, & \text{for SAP user.} \\ \eta_{\text{LA}} (g_{\mu,\alpha_1} dr_{\mu,\alpha_1} k_{\mu,\alpha_1} & \\ \quad + g_{\mu,\alpha_2} dr_{\mu,\alpha_2} k_{\mu,\alpha_2}), & \text{for LA user.} \end{cases} \tag{7.5}$$

  where, $k_{\mu,\alpha}$ represents the time slot allocation between AP $\alpha$ and user $\mu$, which is given as [145]:

$$k_{\mu,\alpha} = \frac{1}{\sum_{\mu'} g_{\mu',\alpha}}, \;\; s.t. \;\; \mu' \in \mathbb{U}$$

- $R_2$: This reward is designed to maximize the average long-term user satisfaction and the immediate reward $r_t$ is defined as [145]:

$$r_t = \frac{\sum_{\mu \in \mathbb{U}} \sum_{\alpha \in \mathbb{AP}} US_{\mu,\alpha} \times C_1}{N_u}, \tag{7.6}$$

  where, $C_1$ scaling factor is included in order to avoid problem of local convergence and $US_{\mu,\alpha}$ is defined as [145]:

$$US_{\mu,\alpha} = \begin{cases} \frac{\eta_{\text{SAP}} g_{\mu,\alpha} dr_{\mu,\alpha} k_{\mu,\alpha}}{R_\mu}, & \text{for SAP user} \\ \frac{1}{R_\mu} \eta_{\text{LA}} (g_{\mu,\alpha_1} dr_{\mu,\alpha_1} k_{\mu,\alpha_1} & \\ \quad + g_{\mu,\alpha_2} dr_{\mu,\alpha_2} k_{\mu,\alpha_2}), & \text{for LA user} \end{cases} \tag{7.7}$$

  where, $R_\mu$ is the required data rate of user $\mu$.

- $R_3$ : It is important to note that reward $R_2$ tries to maximize the average user satisfaction, which means even if a user is achieving very low user satisfaction and others are achieving high user satisfaction, the resultant average will be high. Therefore, the reward $R_2$ is incapable of ensuring the required QoS for every user. The reward $R_3$ is designed to

maximize the long term average network throughput while ensuring 50% user satisfaction ($US_{\mu,\alpha} = 0.5$) for each user. A negative reward with appropriate scaling has been used to ensure 50% user satisfaction. The immediate reward $r_t$, is defined as [145]:

$$r_t = \frac{\sum_{\mu \in \mathbb{U}} \sum_{\alpha \in \mathbb{AP}} Q_{\mu,\alpha}}{N_u}, \tag{7.8}$$

where, $Q_{\mu,\alpha}$ is defined as [145]:

$$Q_{\mu,\alpha} = \begin{cases} -C_2 \times (1 - US_{\mu,\alpha}), & US_{\mu,\alpha} \leq 0.5. \\ C_1 \times US_{\mu,\alpha}, & otherwise. \end{cases} \tag{7.9}$$

where, $US_{\mu,\alpha}$ depends upon the receiver type and is defined by (7.7). Additionally, $C_1$ and $C_2$ scaling factors are included to avoid the problem of local convergence. Furthermore, value of $C_2 > C_1$ ensures that the condition of $US_{\mu,\alpha} \leq 0.5$ is highly discouraged. The values $C_1$ and $C_2$ have been found intuitively by searching the space for values greater than 1. It was found that for $C_1 = 100$, the policy was able to converge to a global solution and beyond 100 there was no change in the system performance. Additionally, a higher value of $C_2$ means the agent will try more aggressively to avoid $US_{\mu,\alpha} \leq 0.5$ but this would penalise the average network throughput performance because there exists a trade-off between the average network throughput and user satisfaction. Therefore, $C_2 = 1000$ was set to provide a balanced performance in terms of the average network throughput and user satisfaction [145].

### 7.3.1 RL Training Algorithm

The objective of the training process is to optimize the policy parameters $\theta$ in order to find the optimal policy, $\pi^*$ which maximize the expected discounted return $\eta(\pi)$ [132].

$$\pi^* = \underset{\pi}{\operatorname{argmax}}(\eta(\pi)),$$
$$\eta(\pi) = \mathbb{E}_{s_0,a_0,\ldots}\left[\sum_{t=0}^{\infty} \gamma^t r(s_t, a_t)\right],$$

where $\gamma \in (0,1)$ indicates the discount factor.

In this work, we have used a MLP with parameters $\theta$ for the policy network and represented the policy as $\pi_\theta(a|s)$. For training of the policy network, we have used TRPO algorithm [132], which is a model-free policy gradient algorithm. TRPO supports good training stability [133] and guarantees monotonic improvement under certain assumptions [132].

*Training performance and convergence of RL*: TRPO stabilizes the learning by imposing trust region constraints on the policy updation. TRPO being a model-free algorithm requires

relatively lower hyper-parameter tuning, but its suffer with high sample complexity [9]. In literature, various methods have been proposed to reduce the sample complexity of TRPO [135, 136]; in this work we have tried to reduce the complexity of TRPO by utilizing the DK which enables us to reduce the action and observation space. Therefore, reduces the overall complexity of the proposed system. By using the TensorBoard visualization toolkit of python the training performance of RL algorithm for three different reward functions with and without knowledge transfer was obtained, as shown in Fig. 7.2.

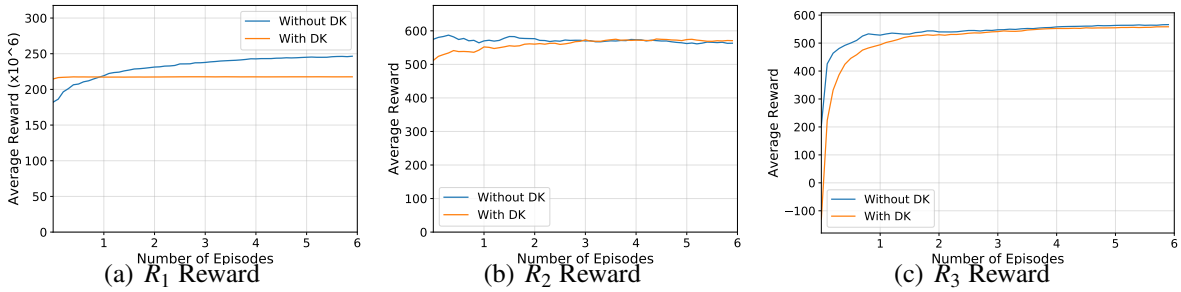


(a) $R_1$ Reward (b) $R_2$ Reward (c) $R_3$ Reward

Figure 7.2: Training performance and convergence of RL for different reward functions without (blue) and with (orange) DK.

It can be observed that for all the reward functions the RL algorithm converges. From Fig. 7.2, it is clear that the RL agent converges to larger rewards when SNR from all the LiFi APs is considered, which is represented by blue colour curve. However, when only 2 best LiFi APs are considered the RL converges to a smaller average reward value indicated by orange colour curves. When $R_1$ is considered the difference in average reward with and without DK is significant, however, for $R_2$ reward both with and without DK converges to same values, as shown in Fig. 7.2 (b). Similarly, for $R_3$ reward both with and without DK converges to same value. It must be noted that only Fig. 7.2(c) has a negative value of average reward, this is due to the design of $R_3$ given in (7.8).

### 7.3.2 Other Load Balancing Methods

- **Received Signal Strength (RSS)** [117]: For a HLWN due to different physical receivers and bandwidth of LiFi and WiFi, the noise component observed at receiver is not uniform. Therefore, received signal strength does not fully represent the quality of channel. Hence, SNR must be used as the decision metric for RSS method in HLWN [9]. For SAP receiver, there will be single value of $\alpha$, the objective function of the RSS method for a

given user $\mu$ is defined as [145]:

$$\max_{\alpha} \ SNR_{\mu,\alpha} \quad \text{s.t} \ \ \alpha \in \mathbb{AP}. \tag{7.10}$$

where, $\mathbb{AP}$ is the set of APs including one WiFi and four LiFi APs and $SNR_{\mu,\alpha}$ represents the SNR values between $\mu$ user and $\alpha$ AP, which can be calculated by Eq. (5.4) and Eq. (5.1) for WiFi and LiFi APs, respectively. For LA receiver, the user will connect to two APs simultaneously, therefore, there will be $\alpha_1$ and $\alpha_2$, corresponding to highest SNR WiFi and LiFi AP, respectively. As there is only one WiFi AP present in the considered scenario, therefore $\alpha_1 = 1$, indicating that user is always connected to WiFi AP. Another variable $\alpha_2$, will give the value corresponding to highest SNR LiFi AP, which is defined as [145]:

$$\alpha_2 = \max_{\alpha_2} \ SNR_{\mu,\alpha_2} \quad \text{s.t} \ \ \alpha_2 \in \mathbb{LAP}. \tag{7.11}$$

- **Exhaustive search**: Exhaustive search also known as brute force search guarantees the best performance at the cost of high complexity. In line with the objective of the proposed RL scheme, the SAP users' objective function for exhaustive search with different rewards $r_t$ is defined as [145]:

$$\begin{aligned} &\max_{g_{\mu,\alpha}k_{\mu,\alpha}} \sum_{\mu\in\mathbb{U}} \sum_{\alpha\in\mathbb{AP}} (r_t), \\ &\text{s.t.} \sum_{\mu\in\mathbb{U}} (g_{\mu,\alpha}k_{\mu,\alpha}) = 1 \forall \alpha \in \mathbb{AP}, \\ &\sum_{\alpha\in AP} g_{\mu,\alpha} = 1 \forall \mu \in \mathbb{U}, \\ &g_{\mu,\alpha} \in \{0,1\}, k_{\mu,\alpha} \in [0,1], \forall \mu \in \mathbb{U}, \forall \alpha \in \mathbb{AP}. \end{aligned} \tag{7.12}$$

where, $r_t$ is defined according to (7.4), (7.6), and (7.8) based on the corresponding rewards function. The first constraint ensures that the sum of time allocation of all users associated to one AP is 1 and the second constraint states that each user can get connected to only one AP at a time. Similarly, for LA receiver, user can connect to both AP's simultaneously, therefore, let $\alpha_1 \in \{0, \mathbb{W}\}$ and $\alpha_2 \in \{0, \mathbb{LAP}\}$ indicate the users connection with WiFi and LiFi APs respectively. For LA receiver, the objective function for exhaustive search in line with proposed RL algorithm with different rewards $r_t$ is

defined as [145]:

$$\begin{aligned} &\max_{g_{\mu,\alpha}k_{\mu,\alpha}} \sum_{\mu\in\mathbb{U}}\sum_{\alpha\in\mathbb{AP}}(r_t), \\ \text{s.t.} &\sum_{\mu\in\mathbb{U}}(g_{\mu,\alpha}k_{\mu,\alpha}) = 1\,\forall\alpha\in\mathbb{AP}, \\ &\sum_{\alpha_1\in\mathbb{W}} g_{\mu,\alpha_1} \le 1\,\forall\mu\in\mathbb{U}, \\ &\sum_{\alpha_2\in\mathbb{LAP}} g_{\mu,\alpha_2} \le 1\,\forall\mu\in\mathbb{U}, \\ &g_{\mu,\alpha}\in\{0,1\}, k_{\mu,\alpha}\in[0,1], \\ &\forall\mu\in\mathbb{U},\forall\alpha\in\mathbb{AP},\forall\alpha_1\in\mathbb{W},\forall\alpha_2\in\mathbb{LAP}. \end{aligned} \tag{7.13}$$

The first constraint is same as that of SAP user objective function. The second and third constraint states the condition that each user can get connected to maximum one WiFi and one LiFi AP at a time. The exhaustive search has been considered in order to provide the upper bound performance at the cost of higher complexity. The exhaustive search implementation has been made possible for this problem because of the room dimension, which restricts the number of users and APs, therefore limits the computational complexity to a reasonable value [9].

## 7.4 Performance Evaluation and Discussion

We have considered a typical $5 \times 5 \times 3$ $m^3$ indoor space, with one WiFi and four LiFi APs, as shown in Fig. 7.1. It is assumed that the WiFi AP fully covers the room, whereas, the four LiFi APs partially covers the room. The focus of this work is to understand the effectiveness of RL based LB in HLWN, therefore, a simple scenario with four LiFi APs [9, 114] and one WiFi AP has been considered in this study. The proposed work is scalable to a larger room with more number of APs and users. Furthermore, two different types of receiver, i.e., SAP and LA schemes have been implemented in simulation. The effect of scheduling and reordering overhead is out of the scope of this work, as that require the protocol design, which has been addressed in [140]. Moreover, in order to study the effect of different reward functions on system performance, three different rewards for optimising various system metrics, as explained in Section 7.3.0.3 have been considered in this work. The simulation setup is coded in python 3.7 and MATLAB 2018. An Open AI Gym environment has been built from scratch for the HLWN. We have used stable-baseline GitHub repository [146] for RL algorithm (TRPO) and implemented ORWP [143]. The results reported are average over 200 episodes, and the values of system parameters are chosen in accordance with previously published works [9, 117, 144] and summarized in Table 7.1.

Table 7.1: System parameters

| **System Parameter** | **Value** |
|---|---|
| Room dimension | $5 \times 5 \times 3$ m$^3$ |
| Number of APs | 4 LiFi + 1 WiFi |
| WiFi AP location | (2.5 m, 2.5 m) |
| LiFi AP locations | (2.5$\pm$1.25 m,2.5$\pm$1.25 m) |
| User distribution | Uniform |
| Mobility Model | ORWP |
| User speed | 1 m/s |
| User receiver | LA, SAP |
| Requested data rate, $R_\mu$ | Poisson with 70 Mbps |
| RL Gym environment | LiFi WiFi network |
| RL policy | MLP, 2 layers of 64 |
| RL max KL divergence, $\delta$ | 0.01 |
| RL Discount factor, $\gamma$ | 0.9 |
| RL Episode length, E | 1000 |
| RL reward scaling factor, $C_1$ | 100 |
| RL reward scaling factor, $C_2$ | 1000 |

The performance of the proposed RL with LA (RL-LA) method has been compared against exhaustive search with LA (Exh-LA), exhaustive search with SAP (Exh-SAP), RSS with LA (RSS-LA) and RSS with SAP (RSS-SAP), based on computational complexity, average network throughput and user satisfaction. Furthermore, this section also compares performance of RL-LA with DK (RL-LA-DK) against the Exh-LA with DK (Exh-LA-DK), Exh-SAP with DK (Exh-SAP-DK), RSS-LA with DK (RSS-LA-DK) and RSS-SAP with DK (RSS-SAP-DK). The details regarding performance metrics are explained in next section.

### 7.4.1 Performance Metrics

In this work, the performance comparison is based on complexity, average network throughput and user satisfaction.

- The average network throughput ($T_{\text{avg}}$) is calculated as [145]:

$$T_{\text{avg}} = \frac{\sum_{\mu \in \mathbb{U}} \sum_{\alpha \in \mathbb{AP}} (t_{\mu,\alpha})}{N_u}, \tag{7.14}$$

  where $t_{\mu,\alpha}$ represents the data rate of each user $\mu$ from the AP $\alpha$, and can be calculated using (7.5)

- The user's satisfaction $S_{\mu,\alpha}$ is defined as the ratio of data rate achieved by the user to the data rate required by that user, it can be expressed as [145]:

$$S_{\mu,\alpha} = \min\{1, US_{\mu,\alpha}\}, \tag{7.15}$$

where $US_{\mu,\alpha}$ is defined by (7.7). The user satisfaction ranges from 0 to 1, $S_{\mu,\alpha} = 1$ implies that the user has achieved the requested data rate.

### 7.4.2 Complexity Analysis

As RL-LA requires training and its convergence dependence on the state action space, and the RL algorithm. The training complexity of RL-LA cannot be directly compared with exhaustive search and RSS as these methods do not have a training phase. Therefore, in this work, the training and convergence of RL is addressed separately in Section 7.3.1 and in this section, only run-time complexity of all methods is considered. In order to calculate complexity of RL-LA, it is important to note that the RLs' real time complexity in test phase is nothing but the complexity incurred in the forward pass of the trained policy network which in this work, is a MLP with 2 hidden layers. Let's assume, the number of neurons in each layer to be $L_1$ and $L_2$, respectively. The input and output layers will be defined based on the dimensions of observation and action space which are explained in section 7.3. Therefore, the complexity of RL-LA is given by $\mathrm{O}((N_{\mathrm{AP}}N_{\mathrm{u}} + N_{\mathrm{AP}})L_1 + (L_1L_2) + (L_2N_{\mathrm{u}}))$ [145].

The RSS-SAP method simply selects the AP with highest SNR value out of total APs ($N_{\mathrm{AP}}$). Therefore, its complexity is $\mathrm{O}(N_{\mathrm{AP}}N_{\mathrm{u}})$ [117]. In RRS-LA method, user is always connected to WiFi AP and selects the highest SNR LiFi AP, therefore, its complexity is $\mathrm{O}(N_{\text{AP-LiFi}}N_{\mathrm{u}})$. The exhaustive search is computationally more expensive, since it looks for all possible connections between users and APs, therefore, the complexity of Exh-SAP is $\mathrm{O}((N_{\mathrm{AP}})^{N_{\mathrm{u}}})$. In case of Exh-LA, the complexity further increases to $\mathrm{O}((N_{\text{AP-WiFi}} + 2N_{\text{AP-LiFi}})^{N_{\mathrm{u}}})$.

The complexity of various schemes with four LiFi and one WiFi AP is illustrated in Fig. 7.3 which is obtained by plotting the corresponding expressions using MATLAB. It is clear that LA receiver has higher complexity as compared to SAP receiver. The application of DK can reduce the complexity of RL-LA and Exh-LA to $\mathrm{O}(((N_{\text{AP-WiFi}}+2)N_{\mathrm{u}} + (N_{\text{AP-WiFi}}+2))L_1 + (L_1L_2) + (L_2N_{\mathrm{u}}))$ and $\mathrm{O}((N_{\text{AP-WiFi}}+4)^{N_{\mathrm{u}}})$, respectively. It is to be noted that RL run-time complexity can be reduced using neural network pruning [147] which is beyond the scope of this work. The effect of DK on the computational complexity for Exh-LA-DK and RL-LA-DK is shown in Fig. 7.4.

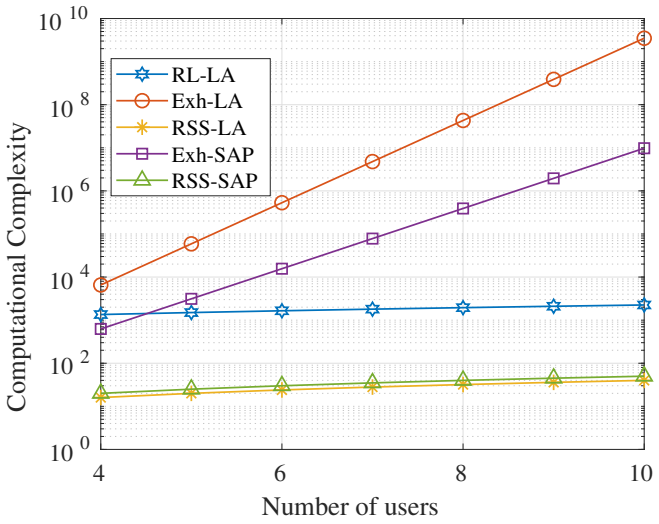


Figure 7.3: Computational complexity of different schemes.

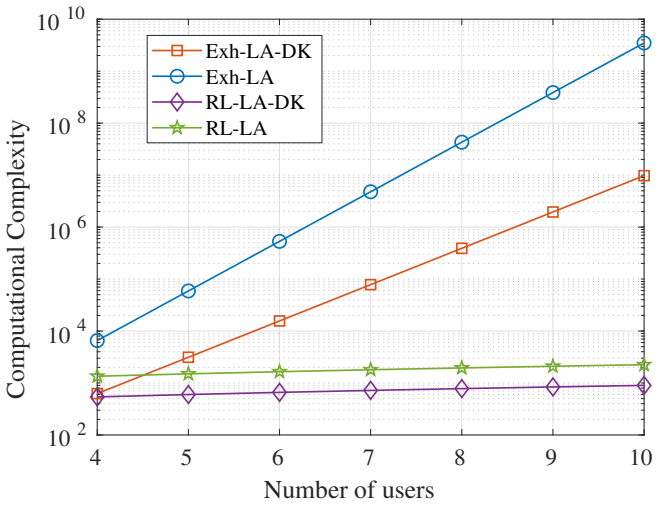


Figure 7.4: Reduced computational complexity with DK.

### 7.4.3 Effect of Different Reward Functions

In this section the effect of different reward functions on average network throughput and user satisfaction has been presented.The average network throughput for different reward functions is summarized in Table 7.2.

It can be observed that the performance of RSS-LA and RSS-SAP remains unchanged for different reward functions, this is due to the fact that for RSS-LA and RSS-SAP, the decision of AP assignment depends alone on the received signal strength and does not take into account the other factors.

Table 7.2: Average network throughput (Mbps) for different reward function.

| Reward | RSS-SAP | Exh-SAP | RSS-LA | Exh-LA | RL-LA |
|---|---|---|---|---|---|
| R1 | 40.66 | 190.83 | 97.60 | 235.81 | 220.90 |
| R2 | 40.45 | 158.81 | 97.52 | 197.10 | 189.50 |
| R3 | 40.86 | 174.81 | 97.80 | 218.90 | 215.90 |

For all rewards, Exh-LA performs best followed by RL-LA in terms of average network throughput. The advantage of link aggregation can be clearly observed from Table 7.2. The RSS-LA provides an improvement of around 57 Mbps over RSS-SAP, similarly, Exh-LA provides an improvement of around 30 Mbps over Exh-SAP. The largest average network throughput of 235 Mbps is achieved by Exh-LA for reward $R_1$, followed by RL-LA which is able to achieve 220 Mbps for reward $R_1$. The value of average network throughput in Exh-LA,RL-LA and Exh-SAP reduces for reward $R_2$, as $R_2$ focuses on maximization of average user satisfaction alone. The reward function $R_3$ provides a more balanced approach that ensures 50% user satisfaction and also tries to maximize the throughput. For reward $R_3$, the average network throughput improves over $R_2$, for Exh-LA, RL-LA and Exh-SAP.

The user satisfaction for each scheme is obtained using the equation (7.15) then CCDF of user satisfaction was plotted using MATLAB. The performance of various schemes in-terms of CCDF of user satisfaction for different reward functions is shown in Fig. 7.5.

It is observed from Fig. 7.5 (a), that none of the schemes are able to ensure full user satisfaction for reward $R_1$, this is due to the fact that the reward $R_1$, is designed specifically to maximize the average network throughput. Therefore, we can see that a system with high average data rate does not guarantee a high QoS for users. The RSS-SAP receiver performs worst as it simply select one highest SNR AP for association. However, when a LA receiver is used, which allows the user to receive simultaneously from highest SNR LiFi and WiFi AP, the performance of RSS-LA improves significantly. As the reward function is focused on improvement of average network throughput, the performance of RL and exhaustive search with SAP and LA receiver suffers in-terms of user satisfaction. For the second reward function $R_2$, the results are shown in Fig. 7.5 (b). It can be seen that the performance of RSS-SAP and RSS-LA remains unchanged, as they are independent of the reward function. The reward function $R_2$ is specifically designed to maximize the average user satisfaction. For Exh-LA, there is significant improvement as it is able to provide full user satisfaction to all the users. Similar trend is observed for RL-LA, which is able to ensure full user satisfaction for 90% of the users and is able to ensure 96% user satisfaction for all users. There is also improvement in Exh-SAP, for reward function $R_2$, but this improvement is limited due to receiver restriction of single AP connection. The user satisfaction performance for $R_3$ reward function is shown in Fig. 7.5 (c). The results for RSS-SAP and RSS-LA remains unchanged. However, there is significant improvement in

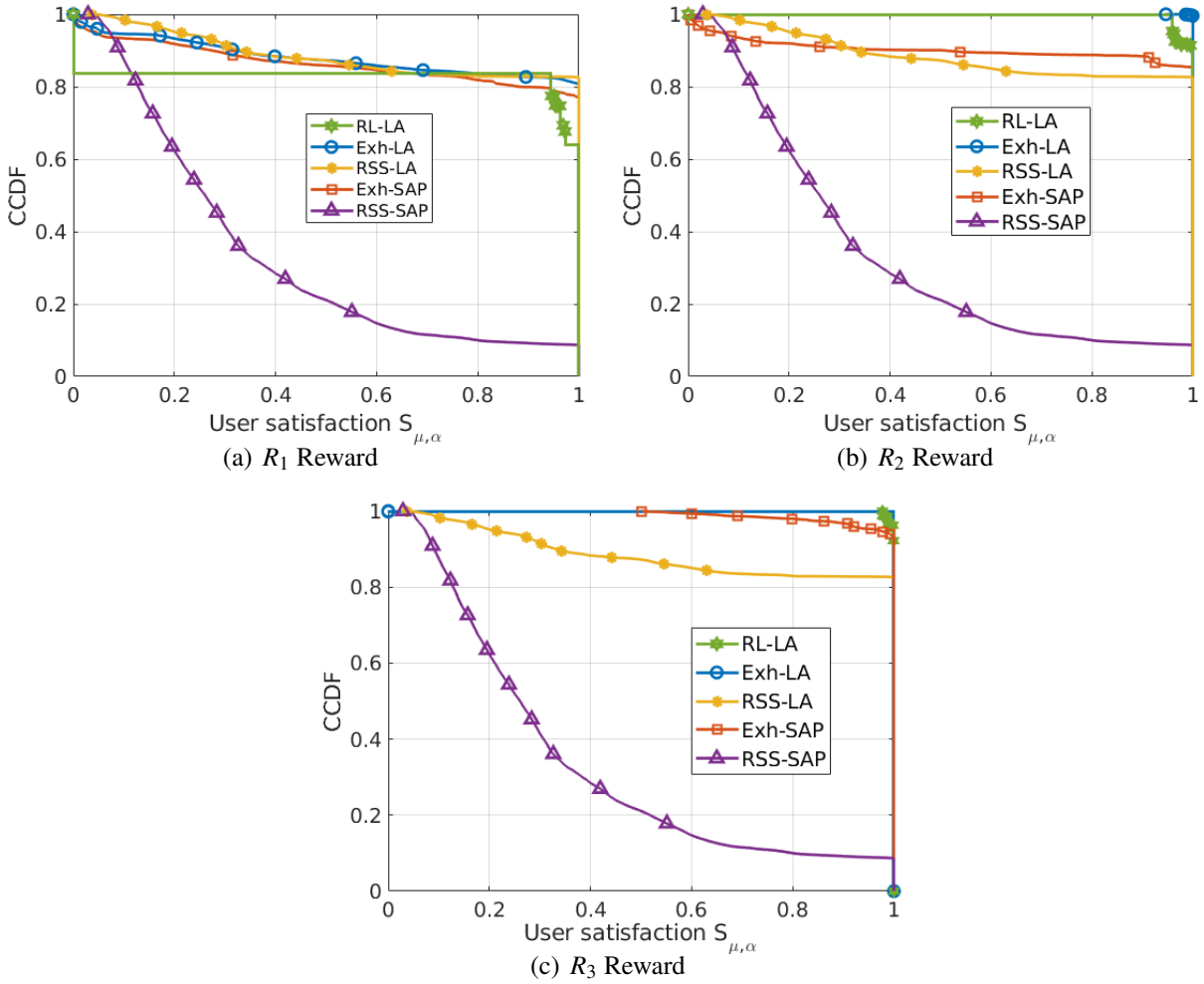


(a) $R_1$ Reward (b) $R_2$ Reward

(c) $R_3$ Reward

Figure 7.5: User satisfaction assessment for different reward functions.

Exh-SAP. The reward $R_3$ ensures that all the users must achieve a user satisfaction of more than 50% and same can be observed from the Fig. 7.5 (c). For $R_3$ reward, RL-LA is able to provide full 98% user satisfaction to all the users. As Exh-LA, was already able to achieve full user satisfaction, therefore, no changes were observed in its performance.

### 7.4.4 Effect of Domain Knowledge

In this section, we present the results of domain knowledge transfer on various schemes with different reward functions. From the VLC domain knowledge, we understand that SNR information from two highest SNR LiFi APs is sufficient for making a decision of AP assignment, inclusion of this simple DK improves the convergence and reduces the computational complexity of proposed schemes. The Exh-LA-DK provides an improvement of around 40

Table 7.3: Average network throughput (Mbps) with Domain knowledge.

| Reward | RSS-SAP-DK | Exh-SAP-DK |
|---|---|---|
| R1 | 40.78 | 178.08 |
| R2 | 40.15 | 143.76 |
| R3 | 40.56 | 159.10 |

| Reward | RSS-LA-DK | Exh-LA-DK | RL-LA-DK |
|---|---|---|---|
| R1 | 97.94 | 216.78 | 205.68 |
| R2 | 97.17 | 180.97 | 173.20 |
| R3 | 97.78 | 203.44 | 199.45 |

Mbps over Exh-SAP-DK. The trend of average network throughput for various schemes with different rewards remains same as it is without the application of DK. However, in order to clearly understand the effect of DK, the values of Table 7.3 are compared with corresponding values from Table 7.2. It can be clearly observed that if only two highest SNR LiFi APs considered for decision making the average network throughput for Exh-LA-DK, RL-LA-DK and Exh-SAP-DK reduces as compared to when all the LiFi APs are considered. However, it is interesting to note that by the application of this simple DK reduces the gap between RL-LA-DK and Exh-LA-DK performance.

The user satisfaction for various schemes with DK, under different reward functions is illustrated in Fig. 7.6.

As the reward $R_1$ focuses on maximization of average network throughput, the user satisfaction performance suffers, as shown in Fig. 7.6(a). For reward $R_2$, the user satisfaction performance for Exh-LA-DK, RL-LA-DK and Exh-SAP-DK improves significantly. From Fig. 7.6(b), it can be observed that Exh-LA-DK is able to provide full user satisfaction to around 95% of the users for reward $R_2$ as compared to 80% in case of reward $R_1$. Similarly, RL-LA-DK with $R_2$, is able to provide full user satisfaction to 90% of users as compared to 85% users when reward $R_1$ was used. The Exh-SAP-DK also observe 10% improvement in the number users achieving full user satisfaction for reward $R_2$ as compared to $R_1$. The user satisfaction performance of various schemes for reward $R_3$ with DK is shown in Fig. 7.6(c). It can be observed that reward $R_3$ provides best user satisfaction performance from individual users point of view. Even after application of DK and reduction of exploration space to only two highest SNR LiFi APs, Exh-LA-DK is able to provide full user satisfaction to 97% and RL-LA-DK is able to support around 96% of the users. The Exh-SAP-DK can ensure full user satisfaction to around 95% of the users. The application of reduced exploration space has a direct effect on the system performance which can be directly seen from Fig. 7.6. However, for reward $R_3$, a good user satisfaction and average network throughput can be achieved even while considering only two highest SNR LiFi APs. The application of DK reduces the system complexity significantly and its effect would be more prominent for a high density network deployment.

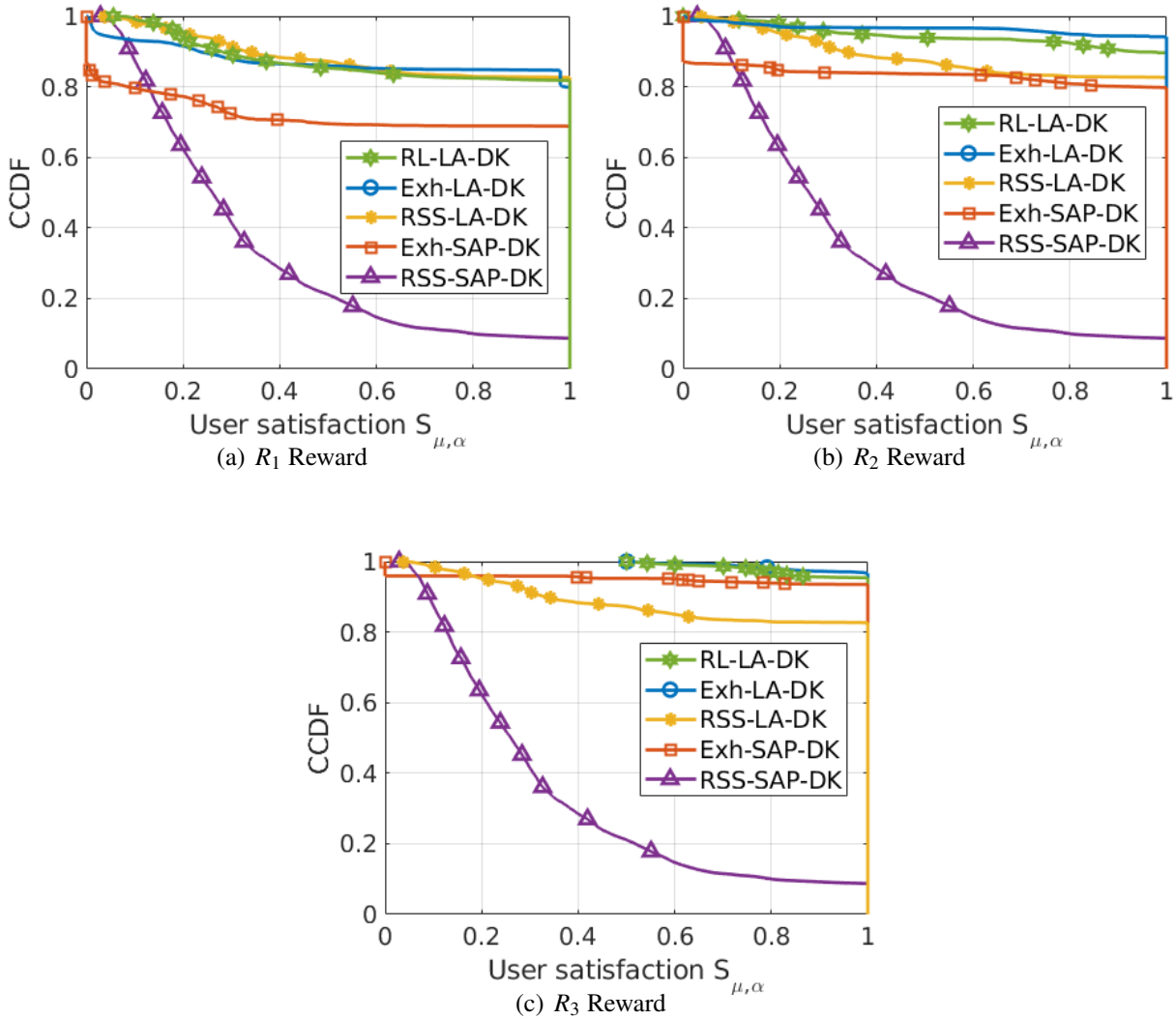


(a) $R_1$ Reward (b) $R_2$ Reward

(c) $R_3$ Reward

Figure 7.6: User Satisfaction performance for different rewards with Domain knowledge.

## 7.5 Summary

In this chapter, RL-based dynamic LB scheme for HLWNs has been considered and three different rewards $R_1$, $R_2$, and $R_3$ have been investigated. From the results, it was observed that for reward $R_1$, RL-LA provided a 106% improvement in average network throughput as compared to RSS-LA, but the user satisfaction was compromised. In the $R_2$ reward, RL-LA ensured complete user satisfaction for 90% of the users and 96% user satisfaction for all users but the average network throughput was reduced. Further, it was observed that RL-LA with reward $R_3$ provided a balanced system performance with high average network throughput (215.90 Mbps) and good user satisfaction (98%). Furthermore, the effects of link

aggregation receivers on the system performance was also investigated. It was observed that Exh-LA provided a minimum improvement of 23% over Exh-SAP in terms of average network throughput. Similarly, RSS-LA provided an improvement of around 57 Mbps over RSS-SAP. Therefore, it can be concluded that LA significantly improved the system performance at the cost of increased complexity. Additionally, it was observed that the computational complexity for RL and exhaustive search increased quadratically and exponentially with the number of users. For the LA receiver scheme, the complexity further increased, which made Exh-LA impractical for real-life scenarios. Therefore, in order to reduce the computational complexity, this chapter introduced a concept from the domain knowledge transfer. It was observed that DK significantly reduced the complexity at the cost of marginal performance degradation for Exh-LA-DK and RL-LA-DK. Overall, the RL-LA-DK with reward $R_3$ provided balanced average network throughput and user satisfaction performance matching to the Exh-LA-DK at a significantly lower complexity.

Chapter 8

# Conclusion and Future Work

In this dissertation, techniques for improving LiFi physical layer and its coexistence with WiFi were investigated. First, we proposed an ALA-based predistoter to mitigate the effect of LED nonlinearity. The proposed method achieved near-linear performance in terms of amplitude-amplitude (AM/AM) distortions and constellation plots. Secondly, in order to combat the issue of high PAPR for O-OFDM, advanced modulation schemes such as DPOOFDM and O-GFDM were analyzed and evaluated against the conventional O-OFDM. It was observed that these proposed modulation schemes significantly reduced the PAPR compared to the O-OFDM counterpart. Additionally, to improve the coexistence of LiFi and WiFi, in this thesis, we investigated a novel reinforcement learning (RL) based load balancing for downlink heterogeneous LiFi and WiFi networks (HLWN). The proposed load balancing algorithm optimized the overall throughput and improved users' satisfaction. Further, the effect of mobility models, receiver orientation, handover, link aggregation, and optimum resource allocation were evaluated. The results were reported in terms of the average system throughput and user satisfaction. The results were compared against conventional signal strength strategy (SSS) and exhaustive search. The proposed RL-based load balancing for HLWN provided a near-optimal performance at significantly lower complexity. The rest of the chapter is organized as follows: Section 8.1 provides summary of the main contributions, followed by Section 8.2 which highlights the possible future research direction.

## 8.1 Summary of Contribution

The main contributions of this dissertation can be summarised as follows:

- The performance of grouped DFT precoded OFDM based on real and imaginary part separation in conjunction with GMSK based pulse shaping termed as DP-OOFDM

was analyzed and evaluated for VLC system. A comprehensive performance analysis of proposed DP-OOFDM in-terms of PAPR, power saving, SER, spectral efficiency and computational complexity against conventional DFT-precoded OOFDM and ACO-OFDM was provided. It was observed that DP-OOFDM schemes had low PAPR and were spectrally efficient as compared to DFT-precoded OFDM and ACO-OFDM. The I-DP-OOFDM outperformed all the other schemes from PAPR perspective and G-I-DP-OOFM was desirable from SER and power-saving points of view. Therefore, when high reliability and power saving is required either G-L-DP-OOFDM or G-I-DP-OOFDM must be used whereas I-DP-OOFDM is the most appropriate modulation scheme for low PAPR.

- An advanced more flexible modulation scheme for next-generation VLC: optical-generalized frequency division multiplexing (O-GFDM) was analyzed and evaluated on the basis of spectral efficiency, complexity, power saving, PAPR, SER, and subcarrier frequency shift tolerance. The performance was compared with the existing O-OFDM counterpart. It was observed that proposed O-GFDM significantly reduced PAPR as compared to O-OFDM counterparts. Further, the proposed OGFDM-DC had better spectral efficiency and significant power saving. The proposed O-GFDM based VLC is expected to very well gel with next generation communication technology to deliver seamless last mile communication services and provide greater flexibility to optimize the network using software-defined networking.

- A reinforcement learning (RL) based dynamic load balancing scheme for downlink heterogeneous LiFi WiFi network was proposed and evaluated. The load balancing in HLWN is a non-convex mixed integer non-linear programmable problem that is mathematically intractable. Thus, an appropriately designed RL based load balancing algorithm wa evaluated in this work. The convergence and effectiveness of this algorithm were studied under different mobility models. It was observed that the RL algorithm achieved better performance than the conventional SSS and iterative optimization algorithm in literature. Further, exhaustive search was also explored to determine the upper-bound. It was observed that the exhaustive optimization provided the best performance at the cost of high computational complexity which is impractical for real life scenarios. In contrast, RL scheme achieved a matching performance to exhaustive search at a significantly lower complexity.

- A reinforcement learning-based load balancing scheme for link aggregation enabled heterogeneous LiFi WiFi network was proposed and evaluated. The system model was modified to take into account the effect of receiver orientation and handover overhead. Additionally, three different reward functions, namely, average network throughput ($R_1$),

average user satisfaction ($R_2$), ensuring min user satisfaction for each user ($R_3$), were evaluated. Furthermore, domain knowledge was included to reduce the action space, which significantly reduced the complexity. The performance was compared against the benchmark in terms of complexity, average throughput, and user satisfaction. It was observed that only reward $R_3$ provided a balanced performance in terms of user satisfaction and average network throughput. Further, the domain knowledge significantly reduced the complexity at the cost of marginal performance degradation for Exh-LA-DK and RL-LA-DK. Overall, the RL-LA-DK with reward R3 provided balanced average network throughput and user satisfaction performance which matched the Exh-LA-DK and offered the advantage of low complexity.

This dissertation can be utilized for improving the LiFi physical layer and efficient coexistence of LiFi and WiFi. This work illustrates the effectiveness of RL based algorithms for solving the load balancing problem in HLWN.

## 8.2 Future Work

There are many possible directions in which the work articulated in this dissertation can be extended. Some of the future research directions are as follows:

- In this dissertation, although the ORWP mobility model considers the effect of receiver orientation, the effect of mobility pattern and blockages which depends upon room layout and other user movement has been neglected. A typical RWP mobility model does not consider the effect of time, space (room layout and furnishing locations), or interaction with other users. Hence, typical RWP fails to capture realistic spatio-temporal channel characteristics. Thus, RWP is not most accurate for considering the mobility-aware load balancing in HLWN [148, 149]. Further, since RL based load balancing is capable of learning and leveraging through the spatio-temporal channel characteristics to skip unnecessary handovers and predict the load on APs, therefore, in order to make a more effective performance evaluation of RL based dynamic LB schemes, an accurate user mobility model must be adopted. The performance of the RL based LB algorithm for HLWN in presence of spatio-temporal channel model will be investigated in our future work.

- The current RL based LB algorithm focuses on the improvement of QoS in terms of average user satisfaction, but other parameters that effects the QoS such as latency and buffer overflow in link-layer are overlooked. Therefore, either the reward function must be redefined to incorporate them or appropriate Markov decision process (MDP) model

must be included in the system model to account for these factors. Furthermore, it is imperative that the link aggregation enabled HLWN will require additional processing at either the network or link layer for splitting and reordering of the packets transmitted over two different links. This processing overhead must be included in the system model to provide more realistic performance evaluation of RL based dynamic LB schemes. These topics will be studied in our future research.

- The current work is limited to downlink HLWNs. In future, this can be extended for bi-directional load balancing. Specifically, based on the user service requirement, the asymmetric downlink-uplink features of network performance can be leveraged [150]. Furthermore, based on different user service requirement, optimal resource allocation must be adopted rather than equal resource allocation that is considered in current work. This will be investigated in our future work.

- In this dissertation, a centralized controller is responsible for all the decision making, it is assumed that the central controller has all the information available instantaneously. However, this is not practical. Therefore, a more suitable approach can be to utilize the central controller to determine the association parameter for each AP [151] and perform the optimal resource allocation at AP level. It is important to note that since link aggregation based system has been considered, therefore, the central controller also needs to determine the split ratio between the LiFi and WiFi network. This can be another future direction.

Chapter 9

# Publications

## 9.1 Journals (Published)

[J1] **Rizwana Ahmad**, Mohammad Dehghani Soltani, Majid Safari, and Anand Srivastava. “Reinforcement Learning-based Near-Optimal Load Balancing for Heterogeneous LiFi WiFi network”. ***IEEE System Journal***, 2021.

[J2] **Rizwana Ahmad** and Anand Srivastava."PAPR Reduction of OFDM Signal Through DFT Precoding and GMSK Pulse Shaping in Indoor VLC." ***IEEE Access***, vol. 8. 2020.

[J3] **Rizwana Ahmad** and Anand Srivastava. "Reinforcement Learning based Load Balancing for Hybrid LiFi WiFi Networks." ***IEEE Access***, vol. 8. 2020.

[J4] **Rizwana Ahmad** and Anand Srivastava. "Optical GFDM: an improved alternative candidate for indoor visible light communication." ***Photonic Network Communications***, 39, 2020.

[J5] Aggarwal, Parag, Tanay Kabra, **Rizwana Ahmad**, Vivek Ashok Bohara, and Anand Srivastava. "Adaptive learning architecture-based predistorter for nonlinear VLC system." ***Photonic Network Communications*** 38, 2019.

## 9.2 Conferences (Published)

[C1] **Rizwana Ahmad**, M. D. Soltani, M. Safari and A. Srivastava, "Load Balancing of Hybrid LiFi WiFi Networks Using Reinforcement learning," in *IEEE 31st Annual International Symposium on Personal, Indoor and Mobile Radio Communications (PIMRC)*, London, U.K., 2020.

[C2] **Rizwana Ahmad** and A. Srivastava, "Optimized User Association for Indoor Hybrid LiFi WiFi Network," in *IEEE International Conference on Transparent Optical Networks (ICTON)*, Angers, France, 2019.

[C3] **Ahmad, Rizwana,** and Anand Srivastava. "Throughput improvement in CAP based indoor VLC system using GMSK filters." In Broadband Access Communication Technologies XIII, vol. 10945, p. 109450P. International Society for Optics and Photonics, SPIE Photonics West, San Francisco, California, United States, 2019.

[C4] **Rizwana Ahmad**, Anand Srivastava, and Hossam A. I. Selmy "Novel modulation scheme for VLC", *Proceedings of SPIE OPTO*, Broadband Access Communication Technologies XII, 105590K, San Francisco, California, United States, Jan. 2018.

[C5] **Ahmad, Rizwana,** Anand Srivastava, and Hossam AI Selmy. "Advanced modulation techniques for low PAPR in VLC system." in *IEEE 20th International Conference on Transparent Optical Networks (ICTON)*, Bucharest, Romania, July 2018.

[C6] Aggarwal, Parag, **Rizwana Ahmad**, Vivek Ashok Bohara, and Anand Srivastava. "Adaptive predistortion technique for nonlinear LED with dimming control in VLC system." in *IEEE International Conference on Advanced Networks and Telecommunications Systems (ANTS)*, Bhubaneswar, India, 2017.

# References


[1] M. Z. Chowdhury, M. K. Hasan, M. Shahjalal, M. T. Hossan, and Y. M. Jang, "Optical wireless hybrid networks: Trends, opportunities, challenges, and research directions," *IEEE Communications Surveys & Tutorials*, 2020.

[2] S. Arnon, *Visible light communication*. Cambridge University Press, 2015.

[3] R. Singh, T. O'Farrell, and J. P. David, "An enhanced color shift keying modulation scheme for high-speed wireless visible light communications," *Journal of Lightwave Technology*, vol. 32, no. 14, pp. 2582–2592, 2014.

[4] P. Chvojka, S. Zvanovec, K. Werfli, P. A. Haigh, and Z. Ghassemlooy, "Variable m-cap for bandlimited visible light communications," in *2017 IEEE International Conference on Communications Workshops (ICC Workshops)*, 2017, pp. 1–5.

[5] M. Z. Afgani, H. Haas, H. Elgala, and D. Knipp, "Visible light communication using OFDM," in *2nd International Conference on Testbeds and Research Infrastructures for the Development of Networks and Communities, 2006. TRIDENTCOM 2006.*, 2006, pp. 6 pp.–134.

[6] H. Schulze, "Frequency-domain simulation of the indoor wireless optical communication channel," *IEEE Transactions on Communications*, vol. 64, no. 6, pp. 2551–2562, 2016.

[7] L. Wu, Z. Zhang, J. Dang, and H. Liu, "Adaptive modulation schemes for visible light communications," *Journal of Lightwave Technology*, vol. 33, no. 1, pp. 117–125, 2015.

[8] M. Z. Chowdhury, M. T. Hossan, A. Islam, and Y. M. Jang, "A comparative survey of optical wireless technologies: Architectures and applications," *IEEE Access*, vol. 6, pp. 9819–9840, 2018.

[9] R. Ahmad, M. D. Soltani, M. Safari, A. Srivastava, and A. Das, "Reinforcement learning based load balancing for hybrid LiFi WiFi networks," *IEEE Access*, vol. 8, pp. 132 273–132 284, 2020.

[10] V. Cisco, "Cisco annual internet report (2018–2023)," *White Paper*, 2019. [Online]. Available: https://www.cisco.com/c/en/us/solutions/collateral/executive-perspectives/annual-internet-report/white-paper-c11-741490.html

[11] T. Cogalan and H. Haas, "Why would 5G need optical wireless communications?" in *2017 IEEE 28th Annual International Symposium on Personal, Indoor, and Mobile Radio Communications (PIMRC)*, 2017, pp. 1–6.

[12] L. U. Khan, "Visible light communication: Applications, architecture, standardization and research challenges," *Digital Communications and Networks*, vol. 3, no. 2, pp. 78–88, 2017.

[13] D. O'Brien, S. Rajbhandari, and H. Chun, "Transmitter and receiver technologies for optical wireless," *Philosophical Transactions of the Royal Society A*, vol. 378, no. 2169, p. 20190182, 2020.

[14] P. S. Preeti Wadhwani, "LiFi market size forecast worth 8 billion usd by 2030," *Global Market Insights*, 2020. [Online]. Available: https://www.gminsights.com/pressrelease/LiFi-market

[15] IEEE 802.15 WPAN task group 13 (TG13) multi-Gigabit/s optical wireless communications. [Online]. Available: https://www.ieee802.org/15/pub/TG13.html

[16] IEEE 802.11 Light Communication TG. [Online]. Available: https://www.ieee802.org/11/Reports/tgbb_update.htm

[17] ITU-T G.9991 (G.VLC). [Online]. Available: https://www.itu.int/ITU-T/workprog/wp_item.aspx?isn=13397

[18] P. H. Pathak, X. Feng, P. Hu, and P. Mohapatra, "Visible light communication, networking, and sensing: A survey, potential and challenges," *IEEE communications surveys & tutorials*, vol. 17, no. 4, pp. 2047–2077, 2015.

[19] Z. Yu, R. J. Baxley, and G. T. Zhou, "Peak-to-average power ratio and illumination-to-communication efficiency considerations in visible light OFDM systems," in *International Conference on Acoustics, Speech and Signal Processing (ICASSP)*. IEEE, 2013, pp. 5397–5401.

[20] Z.-p. Wang and S.-z. Zhang, "Grouped DCT precoding for PAPR reduction in optical direct detection OFDM systems," *Optoelectronics Letters*, vol. 9, no. 3, pp. 213–216, 2013.

[21] G. Wunder, P. Jung, M. Kasparick, T. Wild, F. Schaich, Y. Chen, S. Ten Brink, I. Gaspar, N. Michailow, A. Festag *et al.*, "5GNOW: non-orthogonal, asynchronous waveforms for future mobile applications," *IEEE Communications Magazine*, vol. 52, no. 2, pp. 97–105, 2014.

[22] H. Haas, L. Yin, C. Chen, S. Videv, D. Parol, E. Poves, H. Alshaer, and M. S. Islim, "Introduction to indoor networking concepts and challenges in LiFi," *IEEE/OSA Journal of Optical Communications and Networking*, vol. 12, no. 2, pp. A190–A203, 2020.

[23] R. Bian, I. Tavakkolnia, and H. Haas, "15.73 Gb/s visible light communication with off-the-shelf LEDs," *Journal of Lightwave Technology*, vol. 37, no. 10, pp. 2418–2424, 2019.

[24] E. Khorov, A. Kiryanov, A. Lyakhov, and G. Bianchi, "A Tutorial on IEEE 802.11ax High Efficiency WLANs," *IEEE Communications Surveys Tutorials*, vol. 21, no. 1, pp. 197–216, 2019.

[25] H. Haas, "LiFi: Conceptions, misconceptions and opportunities," in *2016 IEEE Photonics Conference (IPC)*, Oct 2016, pp. 680–681.

[26] H. Haas, L. Yin, C. Chen, S. Videv, D. Parol, E. Poves, H. Alshaer, and M. S. Islim, "Introduction to indoor networking concepts and challenges in LiFi," *Journal of Optical Communications and Networking*, vol. 12, no. 2, pp. A190–A203, 2020.

[27] X. Wu, M. D. Soltani, L. Zhou, M. Safari, and H. Haas, "Hybrid LiFi and WiFi Networks: A Survey," *IEEE Communications Surveys Tutorials*, pp. 1–1, 2021.

[28] S. Ma, R. Yang, H. Li, Z. Dong, H. Gu, and S. Li, "Achievable rate with closed-form for SISO channel and broadcast channel in visible light communication networks," *Journal of Lightwave Technology*, vol. 35, no. 14, pp. 2778–2787, Jul. 2017.

[29] W. Zhang, L. Chen, X. Chen, Z. Yu, Z. Li, and W. Wang, "Design and realization of indoor VLC-WiFi hybrid network," *Journal of Communications and Information Networks*, vol. 2, no. 4, pp. 75–87, Dec 2017.

[30] A. G. Bell, W. Adams, W. Preece *et al.*, "Discussion on the photophone and the conversion of radiant energy into sound," *Journal of the Society of Telegraph Engineers*, vol. 9, no. 34, pp. 375–383, 1880.

[31] U. S. D. of Energy, "Energy savings forecast of solid-state light-ing in general illumination applications," *Global Market Insights*, 2020. [Online]. Available: http://apps1.eere.energy.gov/buildings/publications/pdfs/ssl/energysavingsforecast14.pdf

[32] T. Komine and M. Nakagawa, "Fundamental analysis for visible-light communication system using LED lights," *IEEE transactions on Consumer Electronics*, vol. 50, no. 1, pp. 100–107, 2004.

[33] A. Memedi and F. Dressler, "Vehicular visible light communications: A survey," *IEEE Communications Surveys & Tutorials*, 2020.

[34] H. Kaushal and G. Kaddoum, "Underwater optical wireless communication," *IEEE access*, vol. 4, pp. 1518–1547, 2016.

[35] Y. Zhuang, L. Hua, L. Qi, J. Yang, P. Cao, Y. Cao, Y. Wu, J. Thompson, and H. Haas, "A survey of positioning systems using visible LED lights," *IEEE Communications Surveys & Tutorials*, vol. 20, no. 3, pp. 1963–1988, 2018.

[36] J. M. Kahn and J. R. Barry, "Wireless infrared communications," *Proceedings of the IEEE*, vol. 85, no. 2, pp. 265–298, 1997.

[37] J. R. Barry, J. M. Kahn, W. J. Krause, E. A. Lee, and D. G. Messerschmitt, "Simulation of multipath impulse response for indoor wireless optical channels," *IEEE journal on selected areas in communications*, vol. 11, no. 3, pp. 367–379, 1993.

[38] H. Schulze, "Frequency-domain simulation of the indoor wireless optical communication channel," *IEEE Transactions on Communications*, vol. 64, no. 6, pp. 2551–2562, June 2016.

[39] V. Jungnickel, V. Pohl, S. Nonnig, and C. von Helmolt, "A physical model of the wireless infrared communication channel," *IEEE Journal on Selected Areas in Communications*, vol. 20, no. 3, pp. 631–640, 2002.

[40] D. Tsonev, S. Videv, and H. Haas, "Light fidelity (li-fi): towards all-optical networking," in *Broadband Access Communication Technologies VIII*, vol. 9007. International Society for Optics and Photonics, 2014, p. 900702.

[41] P. Chvojka, K. Werfli, S. Zvanovec, P. A. Haigh, V. H. Vacek, P. Dvorak, P. Pesek, and Z. Ghassemlooy, "On the m-cap performance with different pulse shaping filters parameters for visible light communications," *IEEE Photonics Journal*, vol. 9, no. 5, pp. 1–12, 2017.

[42] N. Fernando, Y. Hong, and E. Viterbo, "Flip-OFDM for optical wireless communications," in *Information Theory Workshop (ITW)*. IEEE, 2011, pp. 5–9.

[43] J. Armstrong and B. J. Schmidt, "Comparison of asymmetrically clipped optical OFDM and DC-biased optical OFDM in AWGN," *IEEE Communications Letters*, vol. 12, no. 5, 2008.

[44] M. Zhang and Z. Zhang, "An optimum DC-biasing for DCO-OFDM system," *IEEE Communications Letters*, vol. 18, no. 8, pp. 1351–1354, 2014.

[45] H. Chun, S. Rajbhandari, G. Faulkner, E. Xie, J. J. McKendry, E. Gu, M. D. Dawson, and D. O'Brien, "Optimum device and modulation scheme selection for optical wireless communications," *Journal of Lightwave Technology*, vol. 39, no. 8, pp. 2281–2287, 2021.

[46] K. Ying, Z. Yu, R. J. Baxley, H. Qian, G.-K. Chang, and G. T. Zhou, "Nonlinear distortion mitigation in visible light communications," *IEEE Wireless Communications*, vol. 22, no. 2, pp. 36–45, 2015.

[47] T. P. Lee, "The nonlinearity of double-heterostructure LED's for optical communications," *Proceedings of the IEEE*, vol. 65, no. 9, pp. 1408–1410, Sept 1977.

[48] B. Inan, S. C. J. Lee, S. Randel, I. Neokosmidis, A. M. J. Koonen, and J. W. Walewski, "Impact of LED nonlinearity on discrete multitone modulation," *IEEE/OSA Journal of Optical Communications and Networking*, vol. 1, no. 5, pp. 439–451, Oct 2009.

[49] D. Tsonev, S. Sinanovic, and H. Haas, "Complete modeling of nonlinear distortion in OFDM-based optical wireless communication," *Journal of Lightwave Technology*, vol. 31, no. 18, pp. 3064–3076, Sept 2013.

[50] H. Elgala, R. Mesleh, and H. Haas, "Non-linearity effects and predistortion in optical OFDM wireless transmission using LEDs," *International Journal of Ultra Wideband Communications and Systems*, vol. 1, no. 2, pp. 143–150, 2009. [Online]. Available: http://www.inderscienceonline.com/doi/abs/10.1504/IJUWBCS.2009.029003

[51] R. Mesleh, H. Elgala, and H. Haas, "Led nonlinearity mitigation techniques in optical wireless OFDM communication systems," *IEEE/OSA Journal of Optical Communications and Networking*, vol. 4, no. 11, pp. 865–875, Nov 2012.

[52] K. Ying, Z. Yu, R. J. Baxley, H. Qian, G. K. Chang, and G. T. Zhou, "Nonlinear distortion mitigation in visible light communications," *IEEE Wireless Communications*, vol. 22, no. 2, pp. 36–45, April 2015.

[53] J. K. Kim, K. Hyun, and S. K. Park, "Adaptive predistorter using NLMS algorithm for nonlinear compensation in visible-light communication system," *Electronics Letters*, vol. 50, no. 20, pp. 1457–1459, September 2014.

[54] R. Mitra and V. Bhatia, "Chebyshev polynomial-based adaptive predistorter for nonlinear LED compensation in VLC," *IEEE Photonics Technology Letters*, vol. 28, no. 10, pp. 1053–1056, May 2016.

[55] R. Mitra, "Precoded chebyshev-NLMS-based pre-distorter for nonlinear LED compensation in NOMA-VLC," *IEEE Transactions on Communications*, vol. 65, no. 11, pp. 4845–4856, Nov 2017.

[56] H. Qian, S. J. Yao, S. Z. Cai, and T. Zhou, "Adaptive postdistortion for nonlinear LEDs in visible light communications," *IEEE Photonics Journal*, vol. 6, no. 4, pp. 1–8, Aug 2014.

[57] P. Aggarwal, T. Kabra, R. Ahmad, V. A. Bohara, and A. Srivastava, "Adaptive learning architecture-based predistorter for nonlinear VLC system," *Photonic Network Communications*, vol. 38, no. 2, pp. 258–269, 2019.

[58] R. A. Shafik, M. S. Rahman, and A. R. Islam, "On the extended relationships among EVM, BER and SNR as performance metrics," in *2006 International Conference on Electrical and Computer Engineering*, Dec 2006, pp. 408–411.

[59] L. Ding, G. T. Zhou, D. R. Morgan, Z. Ma, J. S. Kenney, J. Kim, and C. R. Giardina, "A robust digital baseband predistorter constructed using memory polynomials," *IEEE Transactions on Communications*, vol. 52, no. 1, pp. 159–165, Jan 2004.

[60] Z.-p. Wang, S.-f. Chen, Y. Zhou, M. Chen, J. Tang, and L. Chen, "Combining discrete cosine transform with clipping for PAPR reduction in intensity-modulated OFDM systems," *Optoelectronics Letters*, vol. 10, no. 5, pp. 356–359, 2014.

[61] W. Xu, M. Wu, H. Zhang, X. You, and C. Zhao, "ACO-OFDM-specified recoverable upper clipping with efficient detection for optical wireless communications," *IEEE Photonics Journal*, vol. 6, no. 5, pp. 1–17, 2014.

[62] H. Zhang, L.-L. Yang, and L. Hanzo, "Piecewise companding transform assisted optical-OFDM systems for indoor visible light communications," *IEEE Access*, vol. 5, pp. 295–311, 2016.

[63] D. Abed and A. Medjouri, "Discrete sliding norm transform-based 50% PAPR reduction in asymmetrically clipped optical OFDM systems for optical wireless communications," *Electronics Letters*, vol. 51, no. 25, pp. 2128–2130, 2015.

[64] L. Nadal, M. S. Moreolo, J. M. Fabrega, and G. Junyent, "Comparison of peak power reduction techniques in optical OFDM systems based on FFT and FHT," in *2011 13th International Conference on Transparent Optical Networks*. IEEE, 2011, pp. 1–4.

[65] J. Bai, Y. Li, Y. Yi, W. Cheng, and H. Du, "PAPR reduction based on tone reservation scheme for DCO-OFDM indoor visible light communications," *Optics express*, vol. 25, no. 20, pp. 24 630–24 638, 2017.

[66] W. O. Popoola, Z. Ghassemlooy, and B. G. Stewart, "Pilot-assisted PAPR reduction technique for optical OFDM communication systems," *Journal of Lightwave Technology*, vol. 32, no. 7, pp. 1374–1382, 2014.

[67] S. B. Slimane, "Reducing the peak-to-average power ratio of OFDM signals through precoding," *IEEE Transactions on vehicular technology*, vol. 56, no. 2, pp. 686–695, 2007.

[68] R. You and J. M. Kahn, "Average power reduction techniques for multiple-subcarrier intensity-modulated optical signals," in *2000 IEEE International Conference on Communications. ICC 2000. Global Convergence Through Communications. Conference Record*, vol. 3. IEEE, 2000, pp. 1620–1627.

[69] J. Zhou and Y. Qiao, "Low-PAPR asymmetrically clipped optical OFDM for intensity-modulation/direct-detection systems," *IEEE Photonics Journal*, vol. 7, no. 3, pp. 1–8, 2015.

[70] A. A. Sharifi, "PAPR reduction of optical OFDM signals in visible light communications," *ICT Express*, vol. 5, no. 3, pp. 202–205, 2019.

[71] M. A. Aboul-Dahab, A. Esam, and A. A. Elhaseeb, "PAPR reduction based on DFT precoding for OFDM signals," *International Journal of Future Computer and Communication*, vol. 2, no. 4, p. 325, 2013.

[72] W. Shieh, Y. Tang, and B. S. Krongold, "DFT-spread OFDM for optical communications," in *Digest of the 9th International Conference on Optical Internet (COIN 2010)*. IEEE, 2010, pp. 1–3.

[73] M. Shi, C. Wang, H. Guo, Y. Wang, X. Li, and N. Chi, "A high-speed visible light communication system based on DFT-S OFDM," in *2016 IEEE International Conference on Communication Systems (ICCS)*, Dec 2016, pp. 1–5.

[74] Z.-Y. Wu, Y.-L. Gao, Z.-K. Wang, C. You, C. Yang, C. Luo, and J. Wang, "Optimized DFT-spread OFDM based visible light communications with multiple lighting sources," *Optics express*, vol. 25, no. 22, pp. 26 468–26 482, 2017.

[75] S. B. Slimane, "Peak-to-average power ratio reduction of OFDM signals using pulse shaping," in *Globecom'00-IEEE. Global Telecommunications Conference. Conference Record (Cat. No. 00CH37137)*, vol. 3. IEEE, 2000, pp. 1412–1416.

[76] G. Huang, A. Nix, and S. Armour, "Impact of radio resource allocation and pulse shaping on PAPR of SC-FDMA signals," in *International Symposium on Personal, Indoor and Mobile Radio Communications, PIMRC*. IEEE, 2007, pp. 1–5.

[77] M. Pervej, T. Roy, and M. Sarker, "PAPR reduction analysis of DFT-SCFDMA system using different pulse shaping filters," in *International Forum on Strategic Technology (IFOST)*, 2014.

[78] M. Vittal, K. Ramanaidu, and C. Subhas, "PAPR analysis of single carrier FDMA signals with gaussian pulse shaping," in *International Conference on Communications and Signal Processing (ICCSP)*. IEEE, 2013, pp. 776–780.

[79] O. Mauritz and B. M. Popovic, "Optimum family of spectrum-shaping functions for PAPR reduction of DFT-spread OFDM signals," in *Vehicular Technology Conference, VTC*. IEEE, 2006, pp. 1–5.

[80] H. G. Myung, J. Lim, and D. J. Goodman, "Single carrier FDMA for uplink wireless transmission," *IEEE Vehicular Technology Magazine*, vol. 1, no. 3, pp. 30–38, 2006.

[81] K. Kuchi, "Partial response dft-precoded-ofdm modulation," *Transactions on Emerging Telecommunications Technologies*, vol. 23, no. 7, pp. 632–645, 2012.

[82] C. Wu, H. Zhang, and W. Xu, "On visible light communication using LED array with DFT-spread OFDM," in *2014 IEEE International Conference on Communications (ICC)*. IEEE, 2014, pp. 3325–3330.

[83] A. W. Azim, Y. Le Guennec, and G. Maury, "Hermitian symmetry free optical-single-carrier frequency division multiple access for visible light communication," *Optics Communications*, vol. 415, pp. 177–185, 2018.

[84] R. Bai, Z. Wang, R. Jiang, and J. Cheng, "Interleaved DFT-spread layered/enhanced ACO-OFDM for intensity-modulated direct-detection systems," *Journal of Lightwave Technology*, vol. 36, no. 20, pp. 4713–4722, 2018.

[85] T. Turletti, "GMSK in a nutshell," *Telemedia Networks and Systems Group LCS, MIT-TR*, 1996.

[86] N. Fernando, Y. Hong, and E. Viterbo, "Flip-OFDM for unipolar communication systems," *IEEE Transactions on Communications*, vol. 60, no. 12, pp. 3726–3733, 2012.

[87] R. Ahmad and A. Srivastava, "PAPR reduction of OFDM signal through DFT precoding and GMSK pulse shaping in indoor vlc," *IEEE Access*, vol. 8, pp. 122 092–122 103, 2020.

[88] H. G. Myung, "Introduction to single carrier FDMA," in *European Signal Processing Conference*. IEEE, 2007, pp. 2144–2148.

[89] U. Sorger, I. De Broeck, and M. Schnell, "Interleaved FDMA-a new spread-spectrum multiple-access scheme," in *International Conference on Communications, ICC*, vol. 2. IEEE, 1998, pp. 1013–1017.

[90] H. G. Myung, J. Lim, and D. J. Goodman, "Peak-to-average power ratio of single carrier FDMA signals with pulse shaping," in *International Symposium on Personal, Indoor and Mobile Radio Communications, PIMRC*. IEEE, 2006, pp. 1–5.

[91] J. Wang, Y. Xu, X. Ling, R. Zhang, Z. Ding, and C. Zhao, "PAPR analysis for OFDM visible light communication," *Optics express*, vol. 24, no. 24, pp. 27 457–27 474, 2016.

[92] H. Ochiai, "On instantaneous power distributions of single-carrier fdma signals," *IEEE Wireless Communications Letters*, vol. 1, no. 2, pp. 73–76, 2012.

[93] H. Ochiai, "Peak-to-average power ratio distribution analysis of single-carrier FDMA signals," in *European Wireless 2012; 18th European Wireless Conference 2012*, April 2012, pp. 1–5.

[94] H. Ochiai, "Exact and approximate distributions of instantaneous power for pulse-shaped single-carrier signals," *IEEE Transactions on Wireless Communications*, vol. 10, no. 2, pp. 682–692, 2010.

[95] A. Azim, "Computational performances of OFDM using different FFT algorithms," *International Journal of Communications, Network and System Sciences*, vol. 6, no. 07, p. 346, 2013.

[96] R. Gerzaguet, D. Kténas, N. Cassiau, and J. Doré, "Comparative study of 5G waveform candidates for below 6GHz air interface," in *ETIS workshop on future radio technol., Air interfaces. Sophia Antipolis*, 2016.

[97] T.-A. Truong, M. Arzel, H. Lin, B. Jahan, and M. Jézéquel, "DFT precoded OFDM - an alternative candidate for next generation PONs," *Journal of Lightwave Technology*, vol. 32, no. 6, pp. 1228–1238, 2014.

[98] N. Michailow, M. Matthé, I. S. Gaspar, A. N. Caldevilla, L. L. Mendes, A. Festag, and G. Fettweis, "Generalized frequency division multiplexing for 5th generation cellular networks," *IEEE Transactions on Communications*, vol. 62, no. 9, pp. 3045–3061, 2014.

[99] J. Wu, X. Ma, X. Qi, Z. Babar, and W. Zheng, "Influence of pulse shaping filters on PAPR performance of underwater 5G communication system technique: GFDM," *Wireless Communications and Mobile Computing*, vol. 2017, 2017.

[100] N. Michailow and G. Fettweis, "Low peak-to-average power ratio for next generation cellular systems with generalized frequency division multiplexing," in *2013 International Symposium on Intelligent Signal Processing and Communication Systems*. IEEE, 2013, pp. 651–655.

[101] Z. Sharifian, M. J. Omidi, H. Saeedi-Sourck, and A. Farhang, "Linear precoding for PAPR reduction of GFDMA," *IEEE Wireless Communications Letters*, vol. 5, no. 5, pp. 520–523, 2016.

[102] S. Maheswari and A. Srivastava, "Comparative study of various modulation schemes used in indoor VLC," 2017.

[103] B. M. Alves, L. L. Mendes, D. A. Guimaraes, and I. S. Gaspar, "Performance of GFDM over frequency-selective channels-invited paper," in *Proceedings of International Workshop on Telecommunications*, 2013.

[104] G. Fettweis, M. Krondorf, and S. Bittner, "GFDM-generalized frequency division multiplexing," in *Vehicular Technology Conference*. IEEE, 2009, pp. 1–4.

[105] N. Michailow, S. Krone, M. Lentmaier, and G. Fettweis, "Bit error rate performance of generalized frequency division multiplexing," in *Vehicular Technology Conference (VTC Fall)*. IEEE, 2012, pp. 1–5.

[106] R. Ahmad and A. Srivastava, "Optical GFDM: an improved alternative candidate for indoor visible light communication," *Photonic Network Communications*, vol. 39, no. 2, pp. 152–163, 2020.

[107] L. Chen, B. Krongold, and J. Evans, "Performance analysis for optical OFDM transmission in short-range IM/DD systems," *Journal of Lightwave Technology*, vol. 30, no. 7, pp. 974–983, 2012.

[108] A. Farhang, N. Marchetti, and L. E. Doyle, "Low-complexity modem design for GFDM," *IEEE Trans. Signal Processing*, vol. 64, no. 6, pp. 1507–1518, 2016.

[109] M. Z. Afgani, H. Haas, H. Elgala, and D. Knipp, "Visible light communication using OFDM," in *Testbeds and Research Infrastructures for the Development of Networks and Communities, 2006. TRIDENTCOM 2006. 2nd International Conference on*. IEEE, 2006, pp. 6–pp.

[110] Y. Qiu, H.-H. Chen, and W.-X. Meng, "Channel modeling for visible light communications—a survey," *Wireless Communications and Mobile Computing*, vol. 16, no. 14, pp. 2016–2034, 2016.

[111] J.-H. Choi, B.-J. Lim, Y.-J. Kim, and Y.-C. Ko, "Effect of timing and frequency synchronization errors on GFDM systems," in *Information and Communication Technology Convergence (ICTC)*. IEEE, 2015, pp. 1322–1325.

[112] R. Ahmad, M. D. Soltani, M. Safari, and A. Srivastava, "Load Balancing of Hybrid LiFi WiFi Networks Using Reinforcement learning," in *2020 IEEE 31st Annual International Symposium on Personal, Indoor and Mobile Radio Communications*, 2020, pp. 1–6.

[113] D. Tsonev, S. Videv, and H. Haas, "Towards a 100 gb/s visible light wireless access network," *Opt. Express*, vol. 23, no. 2, pp. 1627–1637, Jan 2015.

[114] T. Komine and M. Nakagawa, "Fundamental analysis for visible-light communication system using LED lights," *IEEE Transactions on Consumer Electronics*, vol. 50, no. 1, pp. 100–107, 2004.

[115] M. D. Soltani, X. Wu, M. Safari, and H. Haas, "Bidirectional User Throughput Maximization Based on Feedback Reduction in LiFi Networks," *IEEE Trans. Commun.*, vol. 66, no. 7, pp. 3172–3186, Jul. 2018.

[116] H. Haas, L. Yin, Y. Wang, and C. Chen, "What is lifi?" *Journal of lightwave technology*, vol. 34, no. 6, pp. 1533–1544, 2016.

[117] X. Wu, M. Safari, and H. Haas, "Access point selection for hybrid Li-Fi and Wi-Fi networks," *IEEE Transactions on Communications*, vol. 65, no. 12, pp. 5375–5385, 2017.

[118] Y. Wang and H. Haas, "Dynamic load balancing with handover in hybrid Li-Fi and Wi-Fi networks," *Journal of Lightwave Technology*, vol. 33, no. 22, pp. 4671–4682, 2015.

[119] Y. Wang, D. A. Basnayaka, X. Wu, and H. Haas, "Optimization of load balancing in hybrid LiFi/RF networks," *IEEE Transactions on Communications*, vol. 65, no. 4, pp. 1708–1720, 2017.

[120] S. Shrivastava, B. Chen, C. Chen, H. Wang, and M. Dai, "Deep Q-network learning based downlink resource allocation for hybrid RF/VLC systems," *IEEE Access*, vol. 8, pp. 149 412–149 434, 2020.

[121] Y. Wang and H. Haas, "Dynamic load balancing with handover in hybrid Li-Fi and Wi-Fi networks," *Journal of Lightwave Technology*, vol. 33, no. 22, pp. 4671–4682, Nov 2015.

[122] V. K. Papanikolaou, P. P. Bamidis, P. D. Diamantoulakis, and G. K. Karagiannidis, "Li-Fi and Wi-Fi with common backhaul: Coordination and resource allocation," in *2018 IEEE Wireless Communications and Networking Conference (WCNC)*, April 2018, pp. 1–6.

[123] M. Kashef, M. Ismail, M. Abdallah, K. A. Qaraqe, and E. Serpedin, "Energy efficient resource allocation for mixed RF/VLC heterogeneous wireless networks," *IEEE Journal on Selected Areas in Communications*, vol. 34, no. 4, pp. 883–893, 2016.

[124] M. S. Demir, S. M. Sait, and M. Uysal, "Unified resource allocation and mobility management technique using particle swarm optimization for vlc networks," *IEEE Photonics Journal*, vol. 10, no. 6, pp. 1–9, 2018.

[125] Y. Wang, X. Wu, and H. Haas, "Fuzzy logic based dynamic handover scheme for indoor Li-Fi and RF hybrid network," in *2016 IEEE International Conference on Communications (ICC)*. IEEE, 2016, pp. 1–6.

[126] R. Zhang, Y. Cui, H. Claussen, H. Haas, and L. Hanzo, "Anticipatory association for indoor visible light communications: Light, follow me!" *IEEE Transactions on Wireless Communications*, vol. 17, no. 4, pp. 2499–2510, 2018.

[127] C. Wang, G. Wu, Z. Du *et al.*, "Reinforcement learning based network selection for hybrid VLC and RF systems," in *MATEC Web of Conferences*, vol. 173. EDP Sciences, 2018, p. 03014.

[128] J. Wang, C. Jiang, H. Zhang, X. Zhang, V. C. Leung, and L. Hanzo, "Learning-aided network association for hybrid indoor LiFi-WiFi systems," *IEEE Transactions on Vehicular Technology*, vol. 67, no. 4, pp. 3561–3574, 2017.

[129] C. Bettstetter, C. Wagner *et al.*, "The spatial node distribution of the random waypoint mobility model." *WMAN*, vol. 11, pp. 41–58, 2002.

[130] R. Jain, A. Durresi, and G. Babic, "Throughput fairness index: An explanation," in *ATM Forum contribution*, vol. 99, no. 45, 1999.

[131] R. Bellman, "A markovian decision process," *Indiana Univ. Math. J.*, vol. 6, pp. 679–684, 1957.

[132] J. Schulman, S. Levine, P. Abbeel, M. Jordan, and P. Moritz, "Trust region policy optimization," in *International conference on machine learning*, 2015, pp. 1889–1897.

[133] T. Zhao, H. Hachiya, G. Niu, and M. Sugiyama, "Analysis and improvement of policy gradient estimation," in *Advances in Neural Information Processing Systems*, 2011, pp. 262–270.

[134] R. S. Sutton and A. G. Barto, *Reinforcement learning: An introduction*. MIT press, 2018.

[135] T. Kurutach, I. Clavera, Y. Duan, A. Tamar, and P. Abbeel, "Model-ensemble trust-region policy optimization," *arXiv preprint arXiv:1802.10592*, 2018.

[136] Y. Tang and S. Agrawal, "Boosting trust region policy optimization by normalizing flows policy," *arXiv preprint arXiv:1809.10326*, 2018.

[137] O. Nachum, M. Norouzi, K. Xu, and D. Schuurmans, "Trust-pcl: An off-policy trust region method for continuous control," *arXiv preprint arXiv:1707.01891*, 2017.

[138] M. Ayyash, H. Elgala, A. Khreishah, V. Jungnickel, T. Little, S. Shao, M. Rahaim, D. Schulz, J. Hilt, and R. Freund, "Coexistence of WiFi and LiFi toward 5G: concepts, opportunities, and challenges," *IEEE Communications Magazine*, vol. 54, no. 2, pp. 64–71, Feb. 2016.

[139] J. Kong, Z.-Y. Wu, M. Ismail, E. Serpedin, and K. A. Qaraqe, "Q-learning based two-timescale power allocation for multi-homing hybrid RF/VLC networks," *IEEE Wireless Communications Letters*, vol. 9, no. 4, pp. 443–447, 2019.

[140] Y. S. M. Pratama and K. W. Choi, "Bandwidth aggregation protocol and throughput-optimal scheduler for hybrid RF and visible light communication systems," *IEEE Access*, vol. 6, pp. 32 173–32 187, 2018.

[141] M. D. Soltani, A. A. Purwita, Z. Zeng, H. Haas, and M. Safari, "Modeling the random orientation of mobile devices: Measurement, analysis and LiFi use case," *IEEE Transactions on Communications*, vol. 67, no. 3, pp. 2157–2172, 2019.

[142] M. D. Soltani, M. A. Arfaoui, I. Tavakkolnia, A. Ghrayeb, M. Safari, C. M. Assi, M. O. Hasna, and H. Haas, "Bidirectional optical spatial modulation for mobile users: Toward a practical design for LiFi systems," *IEEE Journal on Selected Areas in Communications*, vol. 37, no. 9, pp. 2069–2086, 2019.

[143] M. D. Soltani, A. A. Purwita, Z. Zeng, C. Chen, H. Haas, and M. Safari, "An orientation-based random waypoint model for user mobility in wireless networks," in *2020 IEEE International Conference on Communications Workshops (ICC Workshops)*, 2020, pp. 1–6.

[144] Z. Zeng, M. D. Soltani, Y. Wang, X. Wu, and H. Haas, "Realistic indoor hybrid WiFi and OFDMA-based LiFi networks," *IEEE Transactions on Communications*, vol. 68, no. 5, pp. 2978–2991, 2020.

[145] R. Ahmad, M. D. Soltani, M. Safari, and A. Srivastava, "Reinforcement learning-based near-optimal load balancing for heterogeneous lifi wifi network," *IEEE Systems Journal*, 2021.

[146] A. Hill, A. Raffin, M. Ernestus, A. Gleave, A. Kanervisto, R. Traore, P. Dhariwal, C. Hesse, O. Klimov, A. Nichol, M. Plappert, A. Radford, J. Schulman, S. Sidor, and Y. Wu, "Stable baselines," https://github.com/hill-a/stable-baselines, 2018.

[147] D. Blalock, J. J. G. Ortiz, J. Frankle, and J. Guttag, "What is the state of neural network pruning?" *arXiv preprint arXiv:2003.03033*, 2020.

[148] S. Shao, A. Khreishah, and M. Ayyash, "Evaluating the feasibility of random waypoint model for indoor wireless networks," *Internet Technology Letters*, vol. 4, no. 2, p. e214, 2021.

[149] Z.-Y. Wu, M. Ismail, J. Kong, E. Serpedin, and J. Wang, "Channel characterization and realization of mobile optical wireless communications," *IEEE Transactions on Communications*, vol. 68, no. 10, pp. 6426–6439, 2020.

[150] Z. Du, C. Wang, Y. Sun, and G. Wu, "Context-aware indoor VLC/RF heterogeneous network selection: Reinforcement learning with knowledge transfer," *IEEE Access*, vol. 6, pp. 33 275–33 284, 2018.

[151] S. Shao, G. Liu, A. Khreishah, M. Ayyash, H. Elgala, T. D. Little, and M. Rahaim, "Optimizing handover parameters by q-learning for heterogeneous radio-optical networks," *IEEE Photonics Journal, PP (99)*, pp. 1–1, 2019.